Surface science of Cs, CsO and CsI ionic layers on Pt(111)

by

Jakub Drnec
MSc., Charles University, Prague, 2003

A Dissertation Submitted in Partial Fulfillment of the
Requirements for the Degree of

Doctor of Philosophy

in the Department of Chemistry

Surface science of Cs, CsO and CsI ionic layers on Pt(111)

by

Jakub Drnec

MSc., Charles University, Prague, 2003

Supervisory Committee

Dr. D. A. Harrington, Supervisor (Department of Chemistry)

Dr. A. G. Brolo, Departmental Member (Department of Chemistry)

Dr. D. K. Hore, Departmental Member (Department of Chemistry)

Dr. B. C. Choi, Outside Member (Department of Physics)

Supervisory Committee

Dr. D. A. Harrington, Supervisor (Department of Chemistry)

Dr. A. G. Brolo, Departmental Member (Department of Chemistry)

Dr. D. K. Hore, Departmental Member (Department of Chemistry)

Dr. B. C. Choi, Outside Member (Department of Physics)

Abstract

Cesium adsorption on Pt(111) and its coadsorption with iodine and oxygen is studied in this dissertation. The work function during Cs dosing first decreases and at $\Delta\phi \approx 3$ eV ($\theta_{\mathrm{Cs}} = 0.15$) the surface undergoes surface transition between a disordered anomalous state (Pt(111)(*anom*)-Cs) and islands of a Pt(111)(2×2)-Cs causing a change in the slope of the work function curve. The work function curve reaches minimum at -5.5 eV where the surface is fully covered with the Pt(111)(2×2)-Cs structure ($\theta_{\mathrm{Cs}} = 0.25$). Further Cs dosing results in a work function increase and the surface undergoes a phase transition to Pt(111)$(\sqrt{3} \times \sqrt{3})$-Cs. The Cs saturated structure (Pt(111)(*ihcp*)-Cs) has an hexagonal symmetry with the unit cell vector aligned with the $\langle 1, 0 \rangle$ direction of the substrate. Cs in the anomalous state desorbs from the surface in a high-temperature TDS peak (> 1000 K). When the lock-in TDS detection technique is used, this peak appears to be phase shifted by $180\,^{\circ}$ when compared to the desorption peak of normally adsorbed Cs ($\theta_{\mathrm{Cs}} > 0.15$) . This phase shift is a consequence of a positive charge of desorbing Cs. The TDS and work function behavior were explained by a Monte Carlo desorption model incorporating different desorption behavior for all four observed adsorption phases.

When O_2 is dosed on a Pt(111)-Cs surface, the maximum coverage of oxygen

bonded to the surface is significantly increased in comparison to Pt(111). Anomalously adsorbed Cs activates the O_2 bond but does not interact strongly with coadsorbed O. However, when O_2 is dosed on Pt(111)(*ihcp*)-Cs, the oxygen first adsorbs to a sub-layer adsorption site and strongly interacts with Cs. The oxygen in this state is responsible for thermal stabilization of coadsorbed Cs. When iodine is coadsorbed on a Pt(111)-Cs surface, it also strongly interacts with and thermally stabilizes Cs. During the desorption of Cs,I layers, some Cs and I desorb together in the form of a Cs_xI_y cluster.

The surface structures observed by LEED during the coadsorption of Cs and I are in good agreement with atomic arrangements predicted for ionic layers. The validity of this conclusion and the general behavior of ionic layers was checked by an electrostatic energy calculation for various structures.

Table of Contents

List of Tables

List of Figures

Nomenclature

E	Electrostatic energy / J
E_d	Desorption energy / $\mathrm{kJ\,mol^{-1}}$
e	Elementary charge / C
F	Electric field / $\mathrm{V\,m^{-1}}$
H_vap	Heat of vaporization / $\mathrm{kJ\,mol^{-1}}$
k_0	Preexponential factor / $\mathrm{s^{-1}}$
n_g	Number of neighbor atoms
q	Charge / C
R	Gas constant / $\mathrm{J\,K^{-1}\,mol^{-1}}$
s	Temperature ramp rate / $\mathrm{K\,s^{-1}}$
T	Temperature / K
U_cov	Covalent part of total bonding energy / $\mathrm{kJ\,mol^{-1}}$
U_elec	Electrostatic part of total bonding energy / $\mathrm{kJ\,mol^{-1}}$
U_tot	Total bonding energy / $\mathrm{kJ\,mol^{-1}}$
V	Electric potential / V
W	Work / $\mathrm{kJ\,mol^{-1}}$
α'	Polarizability volume / $\mathrm{m^3}$
β	Dipole distance from the surface
$\delta_{i,j}$	Kronecker delta function
ε_0	Vacuum permittivity / $\mathrm{F\,m^{-1}}$
θ	Relative surface coverage

μ	Dipole moment / C m
ξ	Random number
Π	Desorption probability
ϕ	Work function / eV
$\Delta\phi$	Work function change / eV
AES	Auger Electron Spectroscopy
DFT	Density Functional Theory
LEED	Low Energy Electron Diffraction
ML	monolayer
TDS	Thermal Desorption Spectroscopy
WF	Work Function

Acknowledgements

I would like to thank mother Earth to keep me sane, my supervisor David Harrington to guide me through the amazing maze of science and UVic Chemistry Departmental staff for their much appreciated help.

To my family: Petra, Thomas and Anna

Chapter 1

Introduction

The main focus of surface science and electrochemistry research is to examine the chemical reactions on the interfaces between different states of matter. Interface topology and composition are the main factors defining the progression of such reactions. One of the goals of surface science is to find the relationship between reactivity of the surface and its properties such as electronic structure. Knowledge of this relationship allows us to improve the reactivity of the interface or to find novel materials for chemical synthesis. The focus of the current study was to analyze the surface of Pt metal, which is known to have unique properties with regards to heterogenous catalysis and is used in various industrial applications [**1**]. It is also known that modifying the Pt surface with alkali metals improves its catalytic activity for some surface reactions [1–3]. Therefore, in this study, Cs was adsorbed on the Pt(111) surface, and the reactivity of such a modified surface toward oxygen and iodine was studied.

The alkali metals are known to be good catalysts due to their influence on the electronic structure of the surface and coadsorbed molecules. For example, in CO hydrogenation promotion, coadsorbed K weakens the C-O bond while reducing the H_2 chemisorption capacity of the surface [2]. In ammonia synthesis, the role of the alkali metal is to help with the N_2 dissociation [4] and to weaken the NH_3 product

bonding to the surface [1]. Alkali metals are also known to increase the extent of oxidation of the Pt surface and decrease the O_2 dissociation activation energy [5]. This might be important for catalytic processes where O_2 dissociation plays a significant role. Knowing the adsorption sites and interaction characteristics of alkali metals and coadsorbed oxygen can help us to understand the alkali metal promotion mechanism. As a result, better and cheaper catalysts might be found. Another important application for alkali metals is their use in electron emitting cathodes. This is based on the fact that the work function (WF) of the surface can be significantly lowered by the adsorption of an alkali metal monolayer [6].

The adsorption properties of alkali metals on a transition metal surface can significantly differ between different substrate/adsorbate systems, however, some of the structural characteristics are common [7]:

1. The alkali metal layers are disordered at low coverage and room temperature.
2. As the alkali metal coverage increases, the adsorbate condenses into an ordered structure.
3. High coordination number adsorption sites are common for many alkali metals.
4. The nearest-neighbor distances in saturated alkali metal monolayers are smaller than the metallic diameter.

The simplest explanation of alkali metal bonding to a metallic surface was proposed by Langmuir and Gurney [8, 9] and was based on WF observations by Topping [10]. In this model, the alkali metal valence s electron is partially transferred to the substrate and the adsorbed atom can be viewed as charged to a certain extent. Later advances of quantum computing suggested that the bond is not likely purely ionic or purely covalent, but is somewhere between these extreme situations [11, 12].

The partially ionic nature of the bond is believed to be responsible for the characteristic WF response upon alkali metal adsorption [10, 13–15] and the broad desorption peak in TDS spectra [16, 17].

One of the goals of this study was to find the relationship between the type of bonding and the structure of binary layers. Ideally, knowledge of the bonding properties can help to predict the layer topology and vice versa. Wang at al. found mixed hexagonal structures with various stoichiometries when halides were coadsorbed with Tl on an Au(111) electrode in an aqueous environment [18–20]. The layers were either mixed monolayers or bilayers, depending on the size of the halide atoms. The observed mixed monolayer or "coplanar" layers were rationalized in terms of 2D ionic crystals with moderate substrate influence, where both halide and Tl atoms were partially charged. The authors proposed that 1:1, 1:2 and 1:3 stoichiometries are most favorable for 2D binary ionic layers due to maximizing the interactions between adjacent oppositely-charged ions. The coplanar structure was also found by Labayen and Harrington when Tl and I were electrodeposited on a Pt(111) surface [21]. The experimental findings of Cs and I coadsorption on Au(110) surface performed by Wang at al. showed similar behavior: Cs and I ions formed a coplanar structure with a quasi-square symmetry [22]. In the studies of AgI layers electrodeposited on Pt(111), Labayen and Harrington rationalized the structure of the adlayer in terms of covalent bonding within the layer [23, 24]. They suggested that the covalent characteristic of an Ag-I bond is responsible for an AgI bulk-like bilayer surface structure.

The studies mentioned above suggest that the structure of binary layers has either a bilayer or planar character depending on the bonding type. For surfaces where the bond between the adsorbates is covalent, the predicted structure is a bilayer. For layers where bonds between adsorbates are predominantly ionic, the predicted structure is a mixed monolayer. To further test the proposed hypothesis, we prepared binary layers from highly electropositive cesium and electronegative iodine or oxygen. Therefore, the resulting structures were expected to be ionic with a mixed monolayer

structure.

After chapter 2, which describes the experimental methods used, this dissertation is a collection of papers, each addressing a different aspect of the research questions highlighted above. In Chapter 3 of this thesis, the adsorption of Cs on Pt(111) is discussed. For the first time we were able to observe and characterize a low-coverage "anomalous" Cs adsorption state. Cs atoms adsorbed in this state desorb as positive Cs^+ ions and therefore the "anomalous" state is clearly different from the high coverage Cs adsorption states which are typical by neutral desorption. Anomalously-adsorbed Cs was found to have high thermal stability and high activity towards O_2 dissociation. The key technique used in our experiments was Thermal Desorption Spectroscopy (TDS) with a lock-in detection method. This new method developed within our research group [25] allows us to detect neutral and positively charged atoms simultaneously. In Chapter 6 we discuss Monte Carlo (MC) model which we successfully used to fit the experimentally observed results from Chapter 3 for Cs adsorption on Pt(111).

Chapter 4 focuses on the Cs and I coadsorption on Pt(111) and predicted structural trends in alkali-halide layers. We observed both planar and bilayer arrangements depending on the layer composition. A simple electrostatic model was developed to explain the observed structural trends.

Finally, in Chapter 5 the coadsorption of oxygen and Cs on Pt(111) is discussed. We were able to recognize different oxygen adsorption sites and explain their relationship to the coadsorbed Cs. The same LEED pattern for Cs,O and Cs,I layer was observed in both cases, which is consistent with the proposed structure-bonding relationship for ionic layers.

Chapter 2

Experimental

2.1 UHV System

The custom-built Ultra High Vacuum (UHV) system used for all experiments features the ability to transfer a crystal sample between an electrochemical cell and UHV environment. This allows for UHV evaluation of layers prepared under electrochemical conditions, as well as electrochemical studies of layers prepared under UHV.

The apparatus consists of two stainless steel chambers separated by a gate valve (Fig. 2.1). The main chamber is equipped with an ion gun used for sample cleaning, LEED optics (Omicron SPECTALEED), a work function Kelvin probe and a quadrupole mass spectrometer (Hiden HAL 321). The main chamber is evacuated using a high throughput 500 $\mathrm{L\,s^{-1}}$ Pfeiffer turbomolecular pump. The quadrupole mass spectrometer is differentially pumped with a 60 $\mathrm{L\,s^{-1}}$ Pfeiffer turbomolecular pump. The base pressure in the main chamber is typically 1.5×10^{-10} mbar. This pressure can be further reduced to 8×10^{-11} mbar by using a titanium sublimation pump. The high vacuum (HV) chamber (left-most chamber in Fig. 2.1) is equipped with an ionization gauge and is primarily pumped with the 60 $\mathrm{L\,s^{-1}}$ Pfeiffer turbomolecular pump. The first stage pumping required for transfer experiments (from

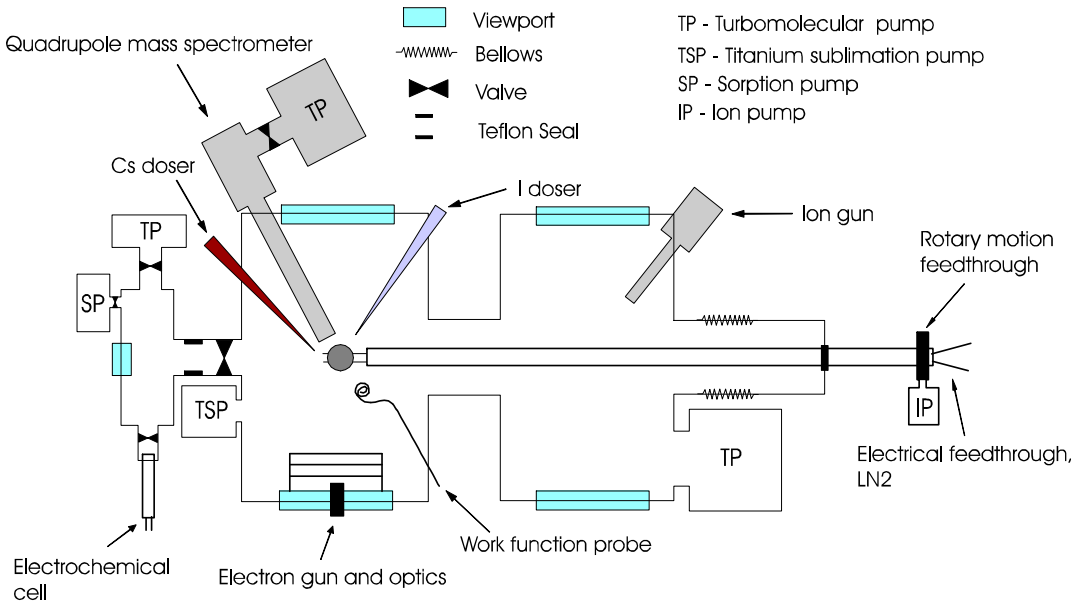

Figure 2.1: UHV system schematic (Department of chemistry, University of Victoria).

ambient pressure to high vacuum pressure) is achieved by two sorption pumps cooled with liquid nitrogen ($N_2(l)$). The base pressure of this chamber is 2×10^{-9} mbar.

The Pt crystal used for experiments was spot welded to two tantalum wires which were then spot welded to the copper feedthrough wires. The K-type thermocouple wires used for temperature measurements were spot welded to the back of the crystal. The feedthrough is located at the end of a stainless steel tube which can be moved between HV and the main chamber. The crystal can be electrically heated up to 1200 K by passing a current (≈ 20 A) through the copper feedthrough wires. Cooling to low temperatures (≈ 90 K) is achieved by filling the transfer tube with $N_2(l)$.

2.2 Crystal Preparation

Two Pt crystals were employed during the course of this study. The first crystal (a disc with a 1 cm diameter cut from the Pt boule grown by Metal Oxides and Crystals Ltd.) was replaced due to deterioration of the surface. Most of the experimental

results were measured using the second crystal disc obtained directly from Metal Oxides and Crystals Ltd.

Preparation of the (111) surface was the same for both crystals. Each crystal was first roughly polished with diamond paste and carefully aligned by back-Laue x-ray diffraction to the desired orientation $\pm 0.5\%$. The aligned crystal was further polished using diamond paste with decreasing grades. The final surface was finished by polishing with a 0.05 μm aluminum oxide slurry. The Pt(111) crystal was then welded to the electrical feedthrough and mounted to the UHV system.

Pt crystals are known to contain significant amounts of Si impurities which remain from the manufacturing procedure. These can, in some cases, negatively affect the experimental outcome [26]. In order to prevent surface contamination, the crystal was initially subjected to multiple oxidation cycles. The crystal surface was annealed to 1150 K in $1 \cdot 10^{-7}$ mbar of O_2 for 1 h which caused the Si impurities to diffuse to the surface and become oxidized. After cooling back to room temperature, the oxidized Si species cannot diffuse back into the bulk and remain on the surface. The formed SiO layer was removed from the surface by Ar^+ sputtering. The amount of Si impurities on the surface left after the oxidation cycles was analyzed by heating the Pt crystal in oxygen atmosphere, cooling it down and measuring the oxygen AES signal. The Si impurity reveals itself as an oxygen AES peak which arises from SiO. Oxidation cycling and Ar^+ sputtering was repeated until the oxygen AES signal was no longer observed. The quality of the surface after the crystal polishing and oxidation cycling was confirmed by LEED. The LEED pattern of a well prepared surface shows sharp spots corresponding to diffraction from the (111) surface (Fig. 2.2).

The crystal was also periodically evaluated for Si impurities during its lifetime. If necessary, it was cleaned by the oxidation cycling procedure.

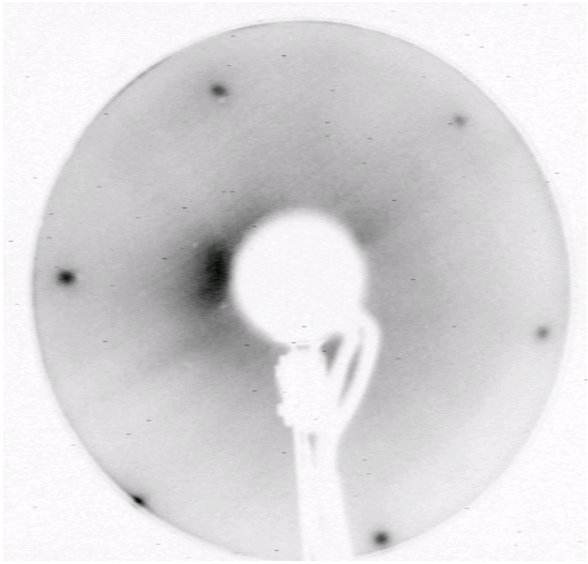

Figure 2.2: The LEED (92 eV, 0.02 μA) pattern from the Pt(111) surface after polishing and 14 oxidation cycles.

2.3 Cs and I Dosing

Dosing the surface with Cs atoms was accomplished with a custom doser (Fig 2.3) designed by the author of this dissertation and built in the chemistry department mechanical shop at University of Victoria. The main component of the doser is a resistively heated getter (SAES Getters, Cs/NF/2.2/12 FT10+10) containing dissolved Cs atoms. The dosing currents applied by an external power supply ranged from 5.5 to 6.5 A for most experiments. The Cs flux was collimated towards the surface using a stainless steel tube. A collimator shutter was used for precise control of the dosing time.

Iodine was dosed on the surface using an electrochemical cell with Ag_4RbI_5 solid state electrolyte [27]. In this cell, iodide ions from Ag_4RbI_5 electrolyte are oxidized to I_2 at the anode by using a small power supply, and subsequently collimated to the crystal. This approach avoids the thermal evaporation of iodine which is known to rapidly contaminate the UHV chamber.

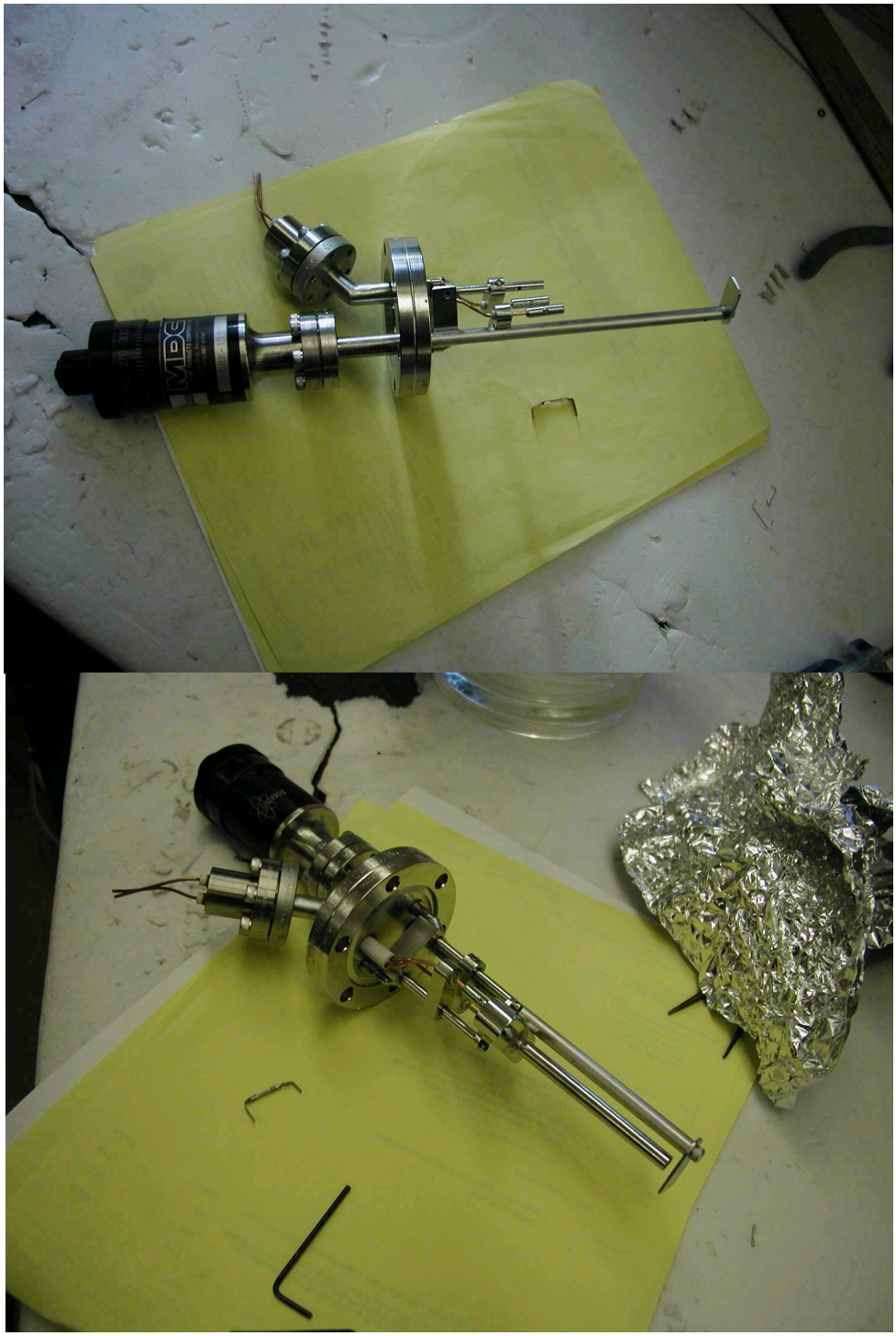

Figure 2.3: Photograph of the custom build Cs doser used in our experiments.

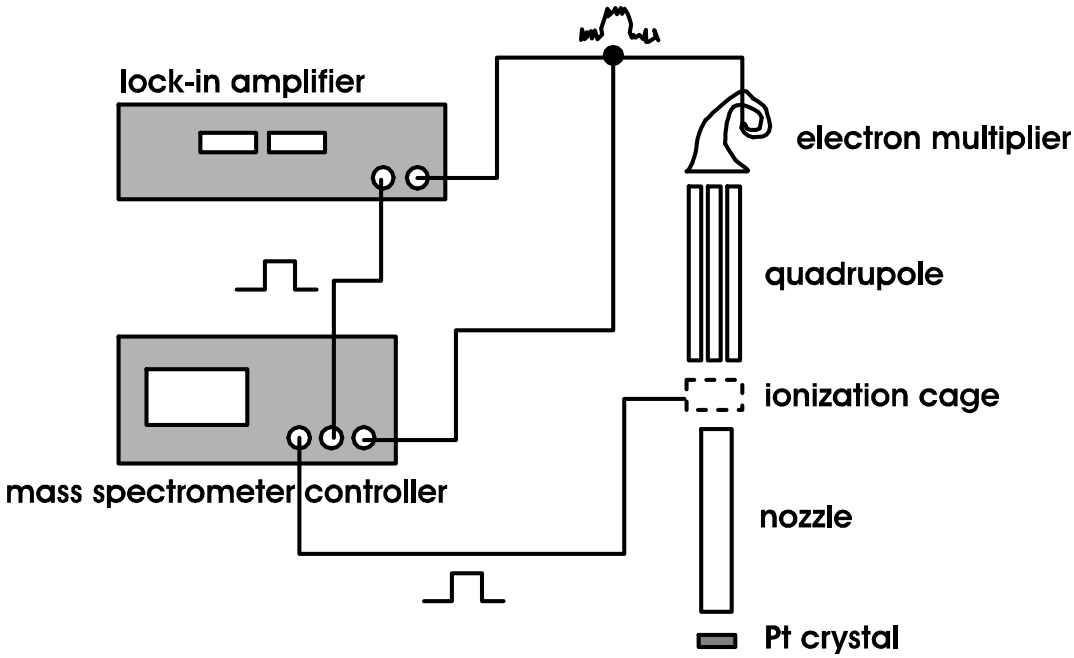

Figure 2.4: Schematic of the experimental setup for TDS. The voltage on the ionization cage was modulated, resulting in the alternating output signal. The modulation and output signals were fed into the lock-in amplifier, permitting intensity and phase shift determination.

2.4 UHV techniques

2.4.1 Thermal Desorption Spectroscopy (TDS)

Use of a lock-in detection scheme (which can be switched on or off) and line-of-sight geometry (Fig. 2.4) allow for increased signal-to-noise ratios, as well as detection of charged and neutral species in one experimental run [25].

The potential of the ionization cage was modulated by a square wave (47 Hz) with switching between -4 V and 3 V in the lock-in detection mode. At negative ionization cage potentials, previously neutral atoms are ionized by electron impact and attracted to the cage grid and do not enter the quadrupole. The signal from the electron multiplier is in the off state at negative cage potentials. Once the ionization cage is switched to positive potentials, the ionized atoms enter the quadrupole and the

signal on the multiplier is a square wave with the same frequency as the signal used to modulate the ionization cage and the signal amplitude is dependent on the number of atoms entering the mass spectrometer. The output signal from the multiplier is locked into the reference modulation square wave, allowing for recovery of amplitude and phase shift information. The phase shift in the case of neutral atoms is ideally $0\,^{\circ}$, but in practise some inherent phase shift is introduced through electronics and during the time ions spend in the ionization cage and quadrupole mass filter.

When *positively* charged ions enter the mass spectrometer nozzle, they immediately feel the electric field from the ionization cage. Therefore, when the cage is at positive potentials, the ions are deflected from their path to the detector and the signal is off. In contrast, when the cage is at negative potential, the positive ions entering the mass spectrometer nozzle are accelerated towards the detector and enter the quadrupole. The signal is on. In other words, *off* state for positive ions is the *on* state for neutral atoms. Therefore the charge of the atom can be immediately determined from the phase shift of the detected signal. The signal from positive ions is phase shifted by $180\,^{\circ}$ compared to the signal from neutral atoms. This can be seen in Fig. 2.5 of the Cs desorption from Pt(111)(*ihcp*)-Cs. The low temperature peak (red curve) from the neutral atoms is phase shifted exactly $180\,^{\circ}$ from the high temperature peak of Cs^{+}.

2.4.2 Work Function Probe

The work function is an important surface property related to changes of electronic structure of the surface. It is extensively used to monitor the adsorption and desorption of atoms and molecules. In our experiments, the work function change of the surface is measured using a Kelvin probe.

The Kelvin probe consists of: (i) a vibrating stainless steel reed with a molybdenum wire loop at the end, (ii) a lock-in amplifier, which is part of a negative feedback

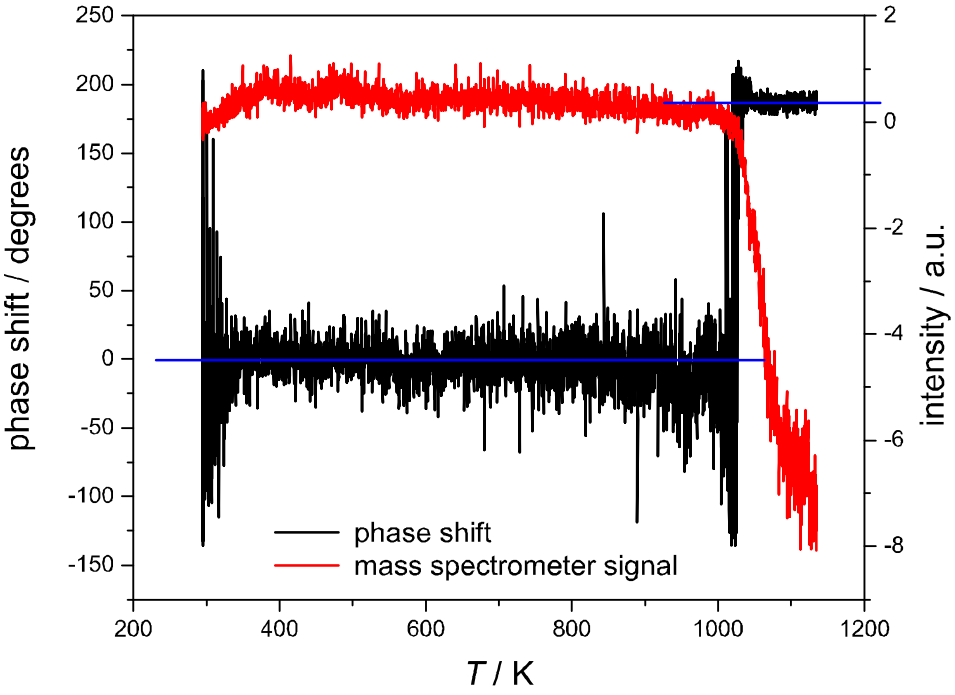

Figure 2.5: Example of an output signal phase shift resulting from detection of neutral and charged atoms. The red curve corresponds to the measured signal from the lock-in amplifier (channel A), black curve shows the phase of the signal. The phase signal is post-processed by shifting to the 0 ° for neutral atoms.

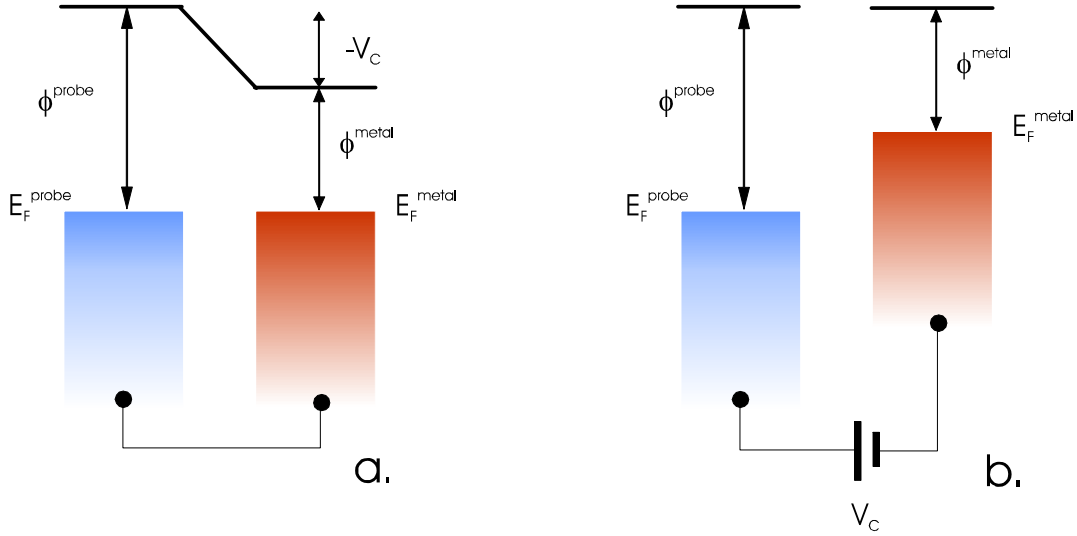

Figure 2.6: Representation of the principle of Kelvin probe WF measurements. The contact potential (a) is offset by an external voltage (b) to form a field free region.

loop between the reed and the Pt crystal. The reed is maintained in close proximity to the crystal, and connection by a metallic conductor would cause the Fermi levels of the reed and crystal to equalize, and there to be an induced contact potential, V_c,equal to the difference in work functions (Fig. 2.6 a). Vibration of the reed causes the capacitance (C) of the reed and surface to periodically change with time. As a result, the charge (q) on the reed and crystal is distorted in the same manner according to Eq. 2.1 :

$$q(t) = C(t) \cdot V_c \tag{2.1}$$

The periodic change of charge induces an oscillating current which is supplied to the lock-in amplifier. When $V = -V_c$ is applied between the reed and crystal, V_c is offset resulting in a electrostatic field free region (Fig. 2.6 b), and no current flows. The feedback loop ensures that no current is flowing through the circuit, by constantly adjusting the voltage between the crystal and the reed.

This method is useful for measuring changes in the work function, however, it cannot be used to measure the absolute value as the ϕ^{probe} is generally unknown. It is

assumed that the work function of the probe remains the same during changes of the surface work function (e.g. by dosing). This assumption is reasonable as the probe is made from untreated molybdenum which is oxidized and only slightly reactive. To measure the absolute value of the work function, a different method which relies on the photoelectric phenomena must be used.

2.4.3 LEED

Low Energy Electron Diffraction (LEED) is one of the most common techniques used in surface science, and is based on the interference of elastically scattered electrons.

The instrumentation consists of an electron gun, retarding grids and a microchannel plate. Low energy electrons generated on an emission cathode are accelerated to a set energy value and focused on the surface using electron optics. Diffracted electrons are filtered with the retarding grids, and only electrons that are elastically scattered can enter the microchannel plate. In the microchannel plate, electrons are multiplied and accelerated to a fluorescent screen. We used a CCD camera to obtain an image of the screen.

Our experiments were performed under the normal incidence angle. In this particular case, the diffraction angle, φ, can be expressed as

$$\sin\varphi = \frac{n}{d_{hk}} \cdot \sqrt{\frac{1.5\ \text{eV}}{U}} \tag{2.2}$$

In Eq. 2.2, n is the diffraction order; the distance between atomic rows of scatters in the $\langle h, k\rangle$ direction is given by d_{hk} in nm, and U is the electron energy in eV. The diffraction angle is inversely proportional to d_{hk}, and therefore the observed LEED pattern is reciprocal to the surface structure in real space.

The reciprocal lattice is defined by the vectors $\overrightarrow{a_j^*}$ obeying Equation 2.3:

$$\overrightarrow{a_i} \cdot \overrightarrow{a_j^*} = \delta_{ij} \ (i, j = 1, 2) \tag{2.3}$$

The surface unit cell basis vectors are given by $\overrightarrow{a_i}$. In other words, $\overrightarrow{a_1} \perp \overrightarrow{a_2^*}$, $\overrightarrow{a_2} \perp \overrightarrow{a_1^*}$ and $\overrightarrow{a_1^*}$, $\overrightarrow{a_2^*}$ follow Eqs. 2.4 and 2.5.

$$\left|\overrightarrow{a_1^*}\right| = \frac{1}{|\overrightarrow{a_1}| \cdot \sin\gamma} \tag{2.4}$$

$$\left|\overrightarrow{a_2^*}\right| = \frac{1}{|\overrightarrow{a_2}| \cdot \sin\gamma} \tag{2.5}$$

γ is the angle between $\overrightarrow{a_1}$ and $\overrightarrow{a_2}$.

Surface structures formed by adsorbed atoms are manifested by the change of the LEED image. Substrate lattice and superlattice structures with unit cell basis vectors $\overrightarrow{b_1}$ and $\overrightarrow{b_2}$ are related by

$$\overrightarrow{b_1} = m_{11}\overrightarrow{a_1} + m_{12}\overrightarrow{a_2} \tag{2.6}$$

$$\overrightarrow{b_2} = m_{21}\overrightarrow{a_1} + m_{22}\overrightarrow{a_2} \ . \tag{2.7}$$

The reciprocal lattice is related in a similar manner as

$$\overrightarrow{b_1^*} = m_{11}^*\overrightarrow{a_1^*} + m_{12}^*\overrightarrow{a_2^*} \tag{2.8}$$

$$\overrightarrow{b_2^*} = m_{21}^*\overrightarrow{a_1^*} + m_{22}^*\overrightarrow{a_2^*} \ . \tag{2.9}$$

If the reciprocal lattice for the superlattice is known, the real space unit cell parame-

ters $\overrightarrow{b_1}$ and $\overrightarrow{b_2}$ can be found from Eqns. 2.6 and 2.7 using

$$m_{11} = \frac{m_{22}^*}{\det M} \tag{2.10}$$

$$m_{12} = \frac{m_{21}^*}{\det M} \tag{2.11}$$

$$m_{21} = \frac{m_{12}^*}{\det M} \tag{2.12}$$

$$m_{22} = \frac{m_{11}^*}{\det M} \tag{2.13}$$

where $\det M = m_{11}^* m_{22}^* - m_{21}^* m_{12}^*$.

2.4.4 AES

Auger Electron Spectroscopy (AES) is based on the energy measurement of inelastically scattered electrons which leave the crystal surface upon excitation by a primary electron beam. We used the LEED diffraction instrument in retarding field analyzer (RFA) mode for analysis. In this configuration, the electrons inelastically scattered from the surface are filtered with retarding grids and collected on the front of the microchannel plate. Since the signal is integral of all electrons entering the RFA with energy $E > eV_{\text{grid}}$, the second derivative was measured to enhance the instrument resolution. The energy of scattered electrons was modulated using a small amplitude sine wave applied on the filtering grids, and the signal was differentiated with a lock-in amplifier.

The Auger process involves three electrons and the mechanism is depicted in Fig. 2.7 .The event proceeds as follows:

1. The inner state of the atom (K) is ionized by primary electrons from the electron gun.

2. The resulting hole is filled with electrons from the outer shell (L_1).

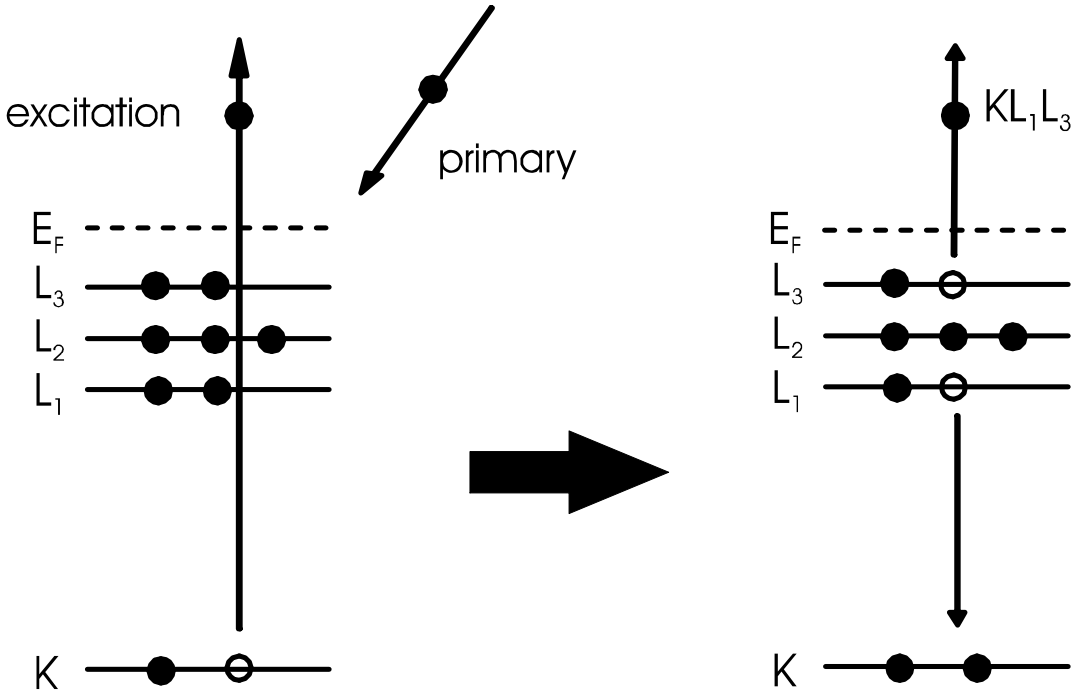

Figure 2.7: Representation of the Auger emission process.

3. The released energy is transmitted via a radiationless process to a second electron from the outer shell (L_3), which is then released from the atom with kinetic energy $E_{\mathrm{kin}} = E_{\mathrm{K}} - E_{\mathrm{L}_1} - E_{\mathrm{L}_3}$.

The orbital energies are specific to a given electron configuration, and therefore vary between different elements. As a result, the kinetic energies of electrons emitted in the Auger process depend on the chemical composition of the surface and this method is particularly useful in a quantitative analysis. It is also possible to detect more subtle changes in chemical bonding but our system resolution is too low for this kind of measurement.

Chapter 3

Anomalous Adsorption of Cs on Pt(111)[1]

3.1 Abstract

The adsorption and reactivity toward oxygen and iodine of Cs on Pt(111) surface for coverages $\theta_{Cs} \leq 0.15$ is reported. These surfaces show unusual "anomalous" behavior compared to higher coverage surfaces. Similar behavior of K on Pt(111) was previously suggested to involve incorporation of K into the Pt lattice. Despite the larger size of Cs, similar behavior is reported here. Anomalous adsorption is found for coverages lower than 0.15 ML, at which point there is a change in the slope of the work function. Thermal Desorption Spectroscopy (TDS) shows a high temperature Cs peak at 1135 K, which involves desorption of Cs^+ from the surface.

The anomalous Cs surfaces and their coadsorption with oxygen and iodine are characterized by Auger Electron Spectroscopy (AES), TDS and Low Electron Energy Diffraction (LEED). Iodine adsorption to saturation on Pt(111)(*anom*)-Cs give rise to a sharp $(\sqrt{7} \times \sqrt{7})R19.1^\circ$ LEED pattern and a distinctive work function increase.

[1]Published in Surface Science, 2009, 603, 2005-2014.

Adsorbed iodine interacts strongly with the Cs and weakens the Cs-Pt bond, leading to desorption of Cs_xI_yclusters at 560 K. Anomalous Cs increases the oxygen coverage over the coverage of 0.25 ML found on clean Pt. However, the Cs-Pt bond is not significantly affected by coadsorbed oxygen, and when oxygen is desorbed the anomalous cesium remains on the surface.

3.2 Introduction

Adsorption of alkali metals on transition metal surfaces has applications based on the modification of electron emission properties and on the promotion of catalysis [2, 6]. This adsorption is also important in fundamental studies because the adsorbates are archetypically electropositive [6, 28]. Although much is known about the adsorption geometry and electronic structure of these systems, an "anomalous" state of adsorption was first reported for K adsorption on Pt(111) [29–31]. The nature of this state is not well understood but has been suggested to be incorporation of K into the Pt lattice in some form of surface alloying. We report here for the first time that similar behavior occurs with Cs on Pt(111). This is surprising since Cs is much larger than K and presumably surface alloying would be more difficult.

According to previous research, the first sign of unusual behavior is a significantly enhanced sticking coefficient for K coverages below a critical coverage $\theta_K < 0.22$ ML, and the presence of a high-temperature desorption peak (maximum at 1100 K) for potassium in Thermal Desorption Spectroscopy (TDS) [29, 31]. Evidence was presented that the high-temperature TDS peak was due to the desorption of positively charged ions.

The anomalous adsorption of K on Pt(111) was further probed by Scanning Tunneling Microscopy (STM), Electron Energy Loss Spectroscopy (EELS) and Low Energy Ion Scattering (LEIS) [30, 31]. STM results showed step reconstruction and upward buckling of localized regions of the Pt substrate. EELS results were originally

explained by K incorporation in the lattice, but a later study revealed that enhanced OH coadsorption from the residual gas gave rise to the loss peak at 225 cm^{-1} originally assigned to the anomalous K [32]. LEIS results showed high background backscattering from Pt for incidence angles $\Psi \geq 20^\circ$ which precluded direct confirmation of subsurface K. Experimental results for $\Psi \leq 20^\circ$ were explained by K incorporation into the substrate and/or by an increased sticking coefficient at low coverages.

Cesium adsorption on Pt(111) is in general strikingly similar to potassium adsorption. For the first time, we observe for Cs the same desorption behavior as for K at low coverage and the high-temperature desorption peak. By suppressing this peak with a negative potential on the crystal we are able to verify that positive ions are desorbing from the surface. We show that co-adsorption of iodine is different in the presence of small amounts of the anomalously adsorbed Cs and alters the adsorption state of the Cs, but coadsorption of oxygen does not alter adsorption state of Cs significantly. Compared to oxygen on clean Pt(111), more oxygen adsorbs on low coverage Cs-Pt surfaces.

3.3 Experimental

The experiments were performed in a stainless steel UHV chamber with a base pressure of 1×10^{-10} mbar. The chamber is equipped with Omicron SPECTALEED single channelplate Low Energy Electron Diffraction (LEED) optics. The LEED optics were used as a retarding field analyzer (RFA) for Electron Auger Spectroscopy (AES) by collecting the electrons from the front of the channelplate, i.e., without using the channelplate gain. AES spectra were run with a normal incidence 20 μA 3 keV electron beam. A quadrupole mass spectrometer (Hiden HAL 321) was used for TDS. It detected the desorbed species via a differentially pumped nozzle with a 1 cm dia. inlet located 0.5 cm from the sample. TDS spectra were taken at a heating rate of 5 $K\,s^{-1}$ unless specified otherwise. A custom lockin-detection scheme was used

to improve the sensitivity [25]. The ion source was switched on and off at 51 Hz, and the modulated output from the secondary-electron multiplier was then measured using a lock-in amplifier. The in-phase and quadrature components were continually monitored, and the magnitude spectrum is presented here. The phase information proved useful also, as described below.

A Kelvin probe previously described in [33] was used to measure work function changes. When using a Kelvin probe for WF measurements, there is a possibility of incorrect measurement owing to Cs adsorption on the Kelvin probe vibrating reference electrode. In our case, this is unlikely as our reference electrode is made from untreated molybdenum which is only slightly reactive. Comparison between WF measurements of Cs adsorption on Pt(111) done by two independent techniques (Kelvin probe [34] and ARUPS [35]) show very good agreement, supporting our conclusion that Cs adsorption on the vibrating electrode is unlikely to lead to artifacts.

Two separate platinum crystals were used in this study, both cut from a boule grown by Metal Oxides and Crystals Ltd. The surfaces were polished with successive grades of diamond paste (Beuhler Ltd.) and oriented to within 0.5° of the (111) plane by back-Laue diffraction. The crystal was further polished by using 0.05 μm aluminium oxide slurry.

The Pt sample could be heated resistively up to 1200 K in UHV using an external power supply which provides up to 35 A to copper feedthroughs connected to the crystal with 0.25 mm dia. Ta support wires. A type K thermocouple was welded on the back side of the crystal. The power supply was controlled by a custom-built temperature controller that incorporates a thermocouple-to-temperature converter in the feedback loop to ensure that the heating ramp is linear. The sample manipulator was cooled by a stream of liquid N_2 to the copper feedthroughs to allow an extended temperature range.

The sample cleaning followed a standard procedure. The sample was initially

bombarded by Ar^+ ions (5 min, 25 μA at 3 keV, Ar pressure 3×10^{-5} mbar). After pumpdown to 9×10^{-10} mbar, the crystal was heated at 10 $K\,s^{-1}$ to 1150 K and then held at this temperature for 5 min. After subsequent cooling, AES and LEED showed a clean, well-ordered surface.

Pt crystals may contain a significant concentration of impurities like silicon that can greatly affect the overall reactivity of the surface [26]. Therefore in order to remove all contaminants, the crystal was periodically annealed at 1150 K in 5×10^{-7} mbar oxygen for 1 h. This allowed contaminants to segregate to the surface and form stable oxides. These oxides were then removed by Ar^+ bombardment as evidenced by the lack of an AES oxygen signal.

The crystal was also periodically checked for possible contaminants by annealing in oxygen atmosphere at 1150 K with a subsequent AES check for O signal after cooling. No platinum oxide forms at high temperatures so detection of an AES oxygen signal after the annealing procedure is a sign of contaminants on the surface. No O signal was detected after successful cleaning.

All Cs structures discussed in this paper were prepared using a SAES cesium dispenser (SAES Getters , Cs/NF/2.2/12 FT10+10) located 10 cm from the surface. The emitted Cs atoms were collimated by a stainless steel tube. The electric current flowing through dispenser was between 5.5 A and 6.5 A for most of the experiments. The cleanliness of the sample was confirmed by the work function measurement during formation of the Cs monolayer. The sample was considered clean if the maximum work function change during Cs dosing was above 4 eV. The maximum work function change showed some variability from experiment to experiment and was between -4 eV and $-$ 5.5 eV. The variation is believed to be mainly caused by anomalously-adsorbed Cs left from previous experiments.

Iodine was dosed using a custom-built doser based on a solid-state Ag_4RbI_5 electrochemical cell [27]. The I_2 molecules produced were collimated by a stainless steel

tube.

Oxygen was dosed by exposing the crystal to 8×10^{-8} mbar O_2 introduced to the chamber through the needle valve.

The quoted coverages were determined by AES. Peak-to-peak heights were normalized relative to the Pt peak at 237 eV, and values from spectra taken on several different spots of the surface structure were averaged. These were referenced to known coverages, assuming the peak heights were proportional to coverage. The reference structures with known coverage were Pt(111)(*ihcp*)-Cs (incommensurate hexagonal close packed, $\theta_{Cs} = 0.41$ ML) [35] and Pt(111)$(\sqrt{7} \times \sqrt{7})R19.1°$-I ($\theta_I = 0.43$ ML) [36–39]. Both reference structures are saturated structures and were obtained by dosing at ambient temperature (293 ± 2 K) until no work function change was observed. The calibration for Cs coverage was further checked by plotting the AES intensity measured from Pt(111)(*ihcp*)-Cs and Pt(111)(2×2)-Cs ($\theta_{Cs} = 1/4$ ML, minimum work function) structures. This was a straight line through the origin as expected.

Temperatures for Cs, I and O dosing varied from 288 K to 293 K. We observed no temperature-dependent variations in work function or other data over this range.

3.4 Results

3.4.1 Cs on Pt(111)

Work function and LEED

The presence of the anomalously-adsorbed Cs is most easily seen by the work function (WF) change on adsorption. Adsorption on a clean surface at 288 K first sharply decreases the work function (Fig. 3.1, black curve). Around $\theta_{Cs} = 0.15 \pm 0.3$, an abrupt change in slope occurs, denoted by "break" on the figure. Then $\Delta\phi$ goes through

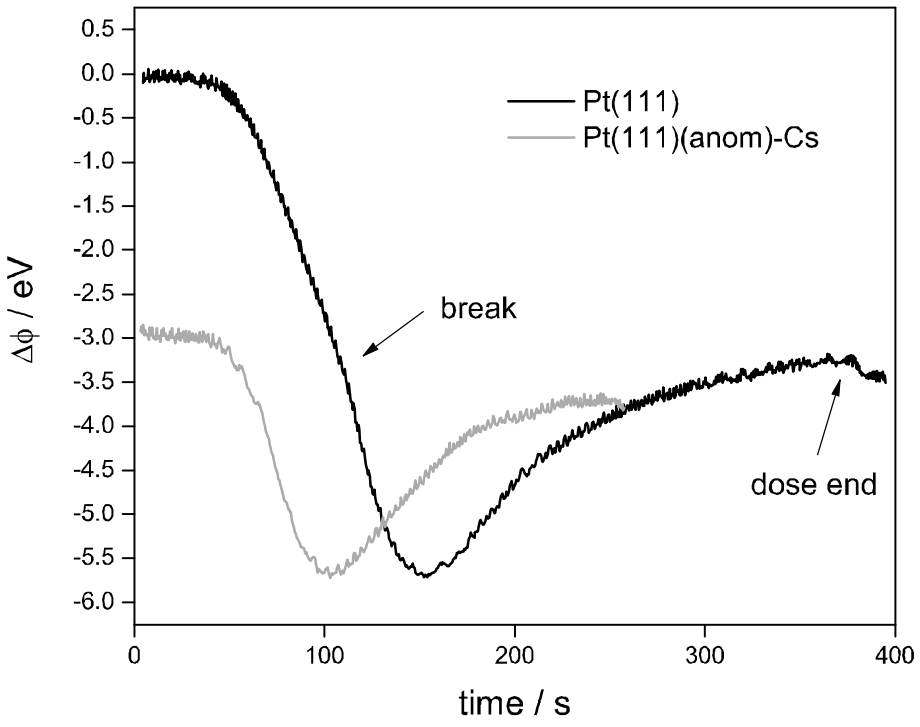

Figure 3.1: Work function change during Cs adsorption at 288 K on clean Pt(111) (black) and on Pt(111)(*anom*)-Cs annealed to 1000 K prior to dosing (grey). The grey curve has been vertically shifted to have the same minimum work function as the black curve.

a minimum at -5.5 eV corresponding to the Pt(111)(2×2)-Cs LEED structure (Fig. 3.2b). Further Cs dosing causes the WF to increase until reaching saturation around $\Delta\phi = 3.5$ eV. The LEED pattern after the WF minimum evolves through Pt(111)$(\sqrt{3} \times \sqrt{3})R30\,^{\circ}$-Cs, mixed Pt(111)$(\sqrt{3} \times \sqrt{3})R30\,^{\circ}$-Cs and Pt(111)$(ihcp)$-Cs to Pt(111)$(ihcp)$-Cs (Fig. 3.2c-e). The Pt(111)$(ihcp)$-Cs pattern has a hexagon of spots with the same orientation as the integral index spots but contracted by about 60%. This structure has been assigned as an incommensurate hexagonal close packed layer of Cs sitting on the surface [40]. After the doser is turned off, a slight drop of work function appears, marked by "dose end" on the graph. The observed WF behavior on Cs adsorption on Pt(111) corresponds well with data recorded by other groups [34, 35, 41]. However, none of the groups recognized either the characteristic break in the WF or the slight drop at the end of the dosing. These groups measured only several values for the whole dosing range, therefore losing fine details about the WF behavior.

The coverage of Cs at the break was determined from the work function curve assuming a constant sticking coefficient for the decreasing part [35]. Only a small change in Cs sticking coefficient as a function of coverage was reported by Davidsen et al. [42]. However, for K on Pt(111), the sticking coefficient was significantly higher for the lowest coverages [31]. Therefore our estimate of the break coverage might be an underestimate.

Annealing the surface at 1150 K for at least 5 min restores a clean surface and subsequent Cs adsorption behavior is reproducible. However, heating the saturated Pt(111)$(ihcp)$-Cs to 1000 K followed by immediate cooling to room temperature and subsequent Cs dosing shows a different WF response (Fig. 3.1, grey curve). The work function change to the minimum is now only ca. 2.5 eV, but the behavior after the minimum is the same as for adsorption on clean Pt(111). This finding points to the fact that after annealing to 1000 K there is still some residual Cs adsorbed on the surface. Following [31], we will refer to this residual Cs as anomalously adsorbed Cs

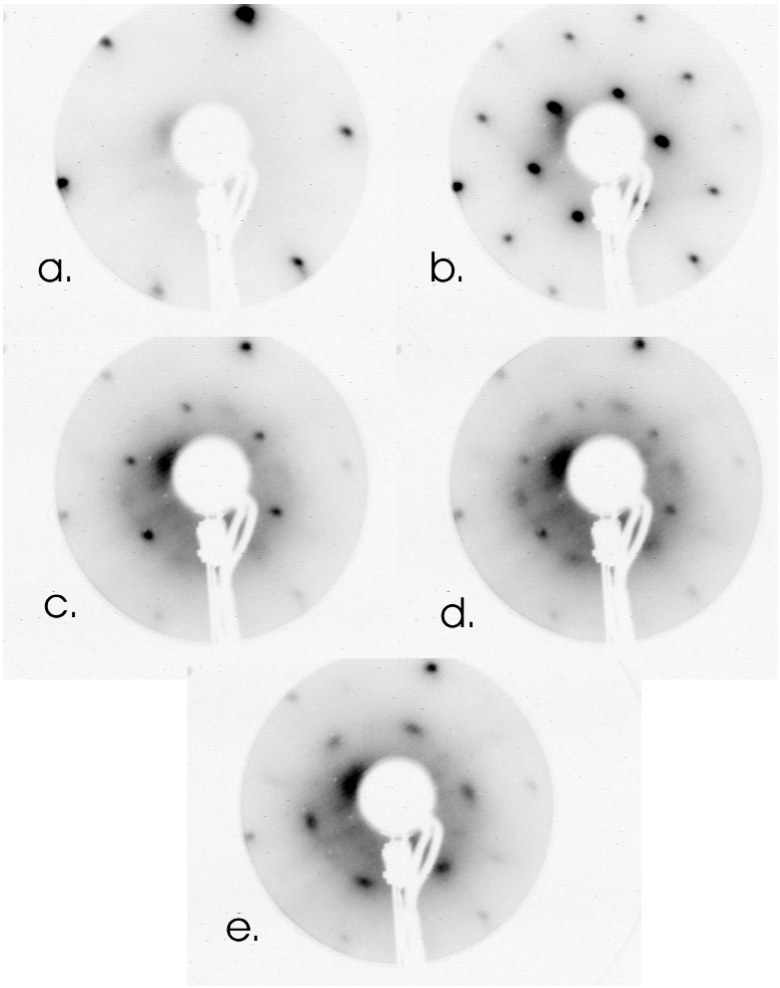

Figure 3.2: LEED patterns during Cs adsorption on Pt(111) at 293 ± 5 K. Patterns shown at 90 eV and $0.01\,\mu$A beam current. a.) clean Pt(111), b.) Pt(111)(2×2)-Cs, c.) Pt(111)$(\sqrt{3} \times \sqrt{3})R30\,^{\circ}$-Cs, d.) mixed Pt(111)$(\sqrt{3} \times \sqrt{3})R30\,^{\circ}$-Cs and Pt(111)(*ihcp*)-Cs, e.) Pt(111)(*ihcp*)-Cs.

and we denote it by Pt(111)(*anom*)-Cs. Calibration by AES after cooling down the crystal, assigns the coverage of Pt(111)(*anom*)-Cs to be $\theta_{\mathrm{Cs}} = 0.12 \pm 0.3$. Evidently, the initial stage of adsorption on the clean surface, corresponding to a work function change of about 3 eV, is directly into the anomalously adsorbed state. The measured coverages agree well within experimental error. A slight difference comes mainly from the different methods used for calibration. Also some of the Cs atoms in the Pt(111)(*anom*)-Cs adsorption state may be desorbed during annealing to 1000 K which may lead to a lower measured coverage by AES.

Effect of crystal ordering on anomalous Cs adsorption

In the course of this study we used two different Pt crystals. The first crystal showed a slow but significant deterioration in the quality of the LEED patterns, and was ultimately replaced. In this study, we present results from the second crystal with better quality sharp LEED patterns. The only exception is Fig. 3.5, where we show TDS from the first crystal for comparison. For the less well-ordered crystal, the onset of the high temperature peak appears at 880 K, about 100 K earlier than for the well-ordered crystal. Therefore, ordering of the surface plays a significant role in the thermal stability of the anomalously-adsorbed Cs, and the lower desorption temperature for the more defect ridden surface suggests that the anomalously-adsorbed Cs may be associated with defect sites. This is despite the fact that these two crystals showed no other significant differences in the behavior of adsorbed Cs or Cs coadsorbed with either I or O_2.

Thermal desorption spectroscopy (TDS)

The TDS spectrum obtained by heating the saturated Pt(111)(*ihcp*)-Cs structure is shown in Figs. 3.3 and 3.4.

The first of these shows a single broad peak at $300 - 1000$ K characteristic of des-

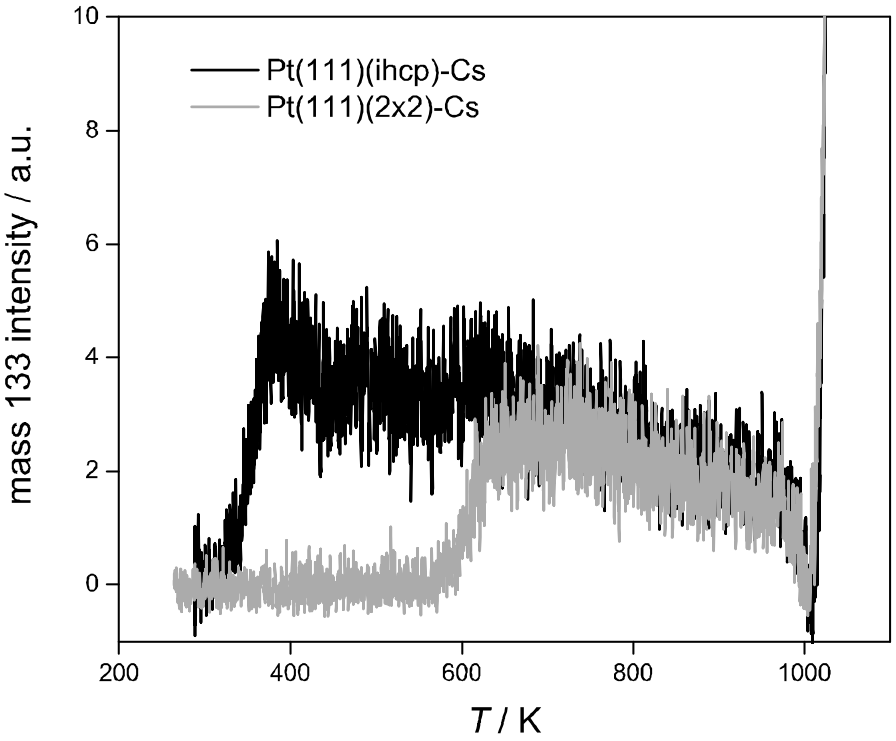

Figure 3.3: Mass 133 (Cs) TDS signal from Pt(111)(2 × 2)-Cs (grey curve) and Pt(111)(*ihcp*)-Cs (black curve). Both heating rates are 5 $\mathrm{K\,s^{-1}}$.

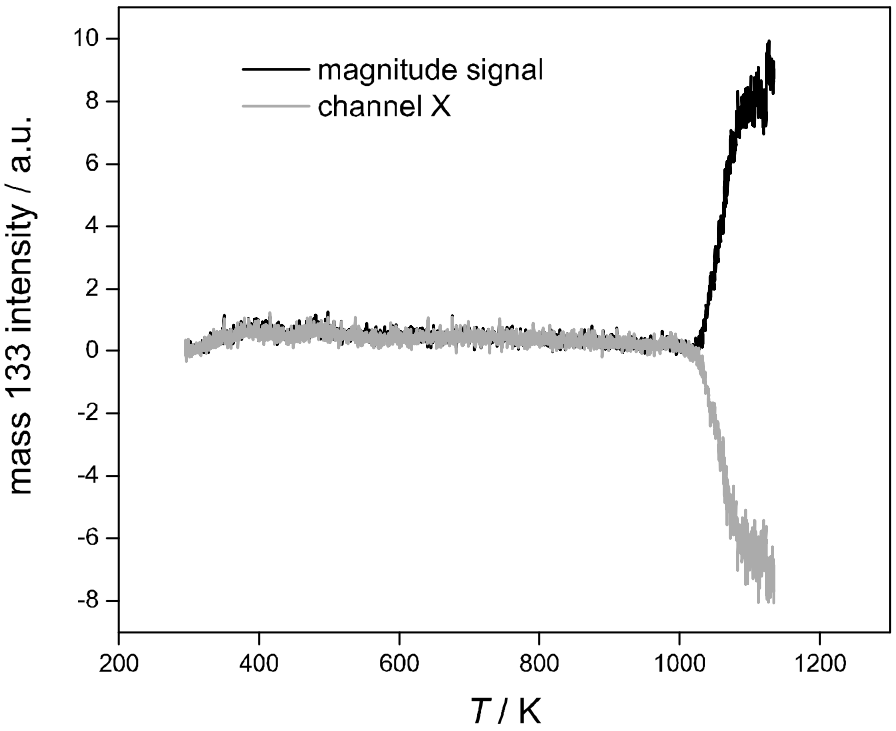

Figure 3.4: Mass 133 (Cs) TDS lock-in signal during Cs desorption (5 $\mathrm{K\,s^{-1}}$). Grey curve is the signal from channel X (in-phase component) of the lock-in amplifier. Black curve shows the magnitude signal.

orption of alkali metals from transition metal surfaces with significant charge transfer or polarization. Below 1000 K, the spectra closely resemble those of Cs on Pt(111) measured at 4.25 $\mathrm{K\,s^{-1}}$ [42] and of K on Pt(111) measured at 30 $\mathrm{K\,s^{-1}}$ [5]. The broad shape of the peak with a nearly linear decay on the top is consistent with repulsive lateral interactions between adsorbed atoms as verified by model studies [17].

The sudden increase of signal above 1000 K is the beginning of very large peak, seemingly the desorption of many monolayers, seen more clearly in the black spectrum in Fig. 3.4. Our heating system is unstable at high enough temperature to see the decrease in signal that presumably occurs. A similar high temperature TDS peak was observed in the case of K adsorption on Pt(111) and for K on Pd(110) [29,43], but to the best of our knowledge, has not been previously observed for other alkali metals on Pt(111).

The modulation scheme used clearly divides the peaks into two categories. In normal operation, the reference signal is adjusted to maximize the in-phase component. For the large peak above 1000 K, the in-phase signal has changed sign, i.e a 180° phase shift relative to the signal below 1000 K (Fig. 3.4). A more detailed discussion of this is given below, but the behavior supports that suggestion of Lehmann [29] that the Cs is desorbing in a different charge state, specifically as a positive ion.

Definitive support for the assignment of the high-temperature peak to desorption of Cs^+ is shown by changing the potential on the sample to -20 V during the TDS measurement, just after the beginning of the high temperature desorption. This causes this desorption to be suppressed, with the signal returning close to the baseline (Fig. 3.5).

This behavior confirms that the Cs species leaving the surface in the low temperature peak is neutral but in the high temperature peak is positively charged.

The high temperature Cs^+ TDS peak was not observed in the work of Davidsen et al. [42]. They measured only the low temperature neutral TDS peak extended

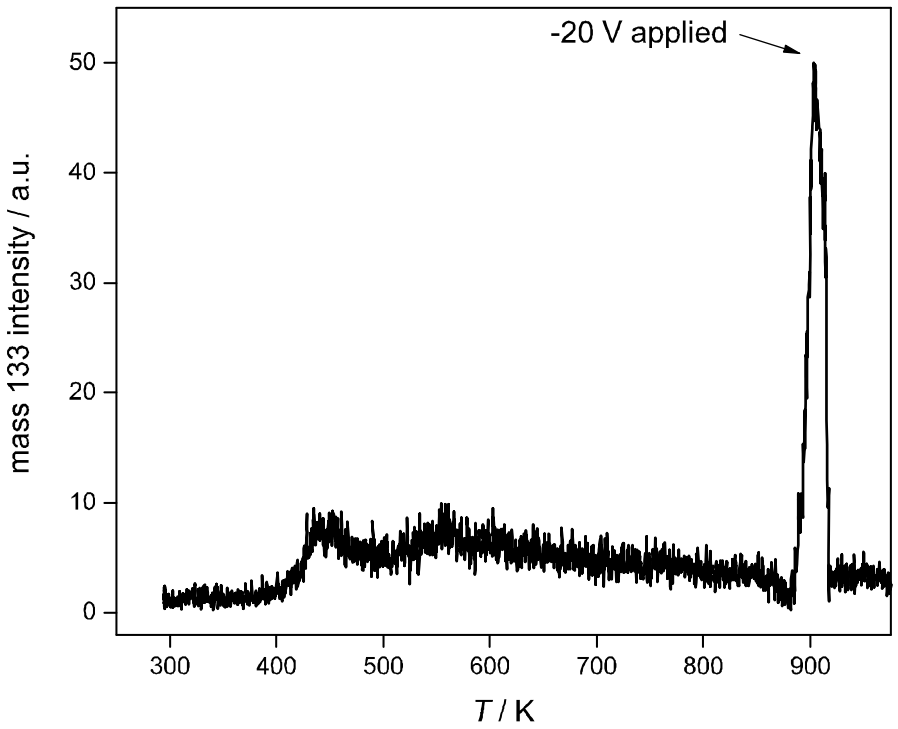

Figure 3.5: Mass 133 (Cs) TDS experiment showing the effect of applied potential on the high temperature ionic desorption peak. The temperature was ramped at 5 $\mathrm{K\,s^{-1}}$. As the ionic peak starts to evolve, a potential of $-20\,\mathrm{V}$ was applied to the crystal. The signal dropped to its baseline value. Note: A different crystal was used in this experiment, for which the high temperature peak starts at a lower temperature.

to 1200 K, presumably because their mass spectrometer rejected desorbing positive ions. In our work, the tail of the low temperature broad peak is masked by the high temperature Cs^+ peak. However, the neutral desorption is seen in Fig. 3.5, as the non-zero signal that remains after the negative voltage is applied.

The desorption energy for the high temperature peak was estimated in two different ways: fitting an exponential to the leading edge (as appropriate for a zero-order desorption) and by Redhead analysis [44]. Leading edge analysis gives $E_\mathrm{d} = 456 \pm 21$ kJ mol^{-1}, and Redhead analysis, assuming first-order desorption and a pre-exponential factor of 10^{13} s^{-1}, yielded $E_\mathrm{d} = 301$ kJ mol^{-1} at the peak maximum of 1135 K. Although these are approximate and assumption dependent, they are very high values, much higher than would be expected for neutral normal desorption.

Following Lehmann, we also sought a positive crystal current correlated to the positive ion flux assumed to be leaving the surface. The current through the sample during the TDS experiment was measured by grounding the sample through a 100 kΩ resistor. We find that the crystal current increases when the temperature reaches 1000 K. Measuring the current during the heating of Pt crystal without adsorbed Cs results in the same response and therefore this current cannot be associated with the desorption process. The current flows in the opposite direction than expected although it is of the order of 2 μA, similar to Lehman's case [29]. Such current can be caused by either thermionic emission from the sample or more likely by poor electrical isolation in the floating power supply used to heat the crystal. A small stray current is not unexpected as the heating current at this temperature is close to 20 A.

3.4.2 I adsorption on Pt(111)(*anom*)-Cs

Having detected an anomalous state of Cs on the Pt(111) surface, we sought to characterize it further by investigating its reactivity toward two adsorbates, iodine and oxygen. Pt(111)(*anom*)-Cs surface prepared by adsorbing Cs to saturation at

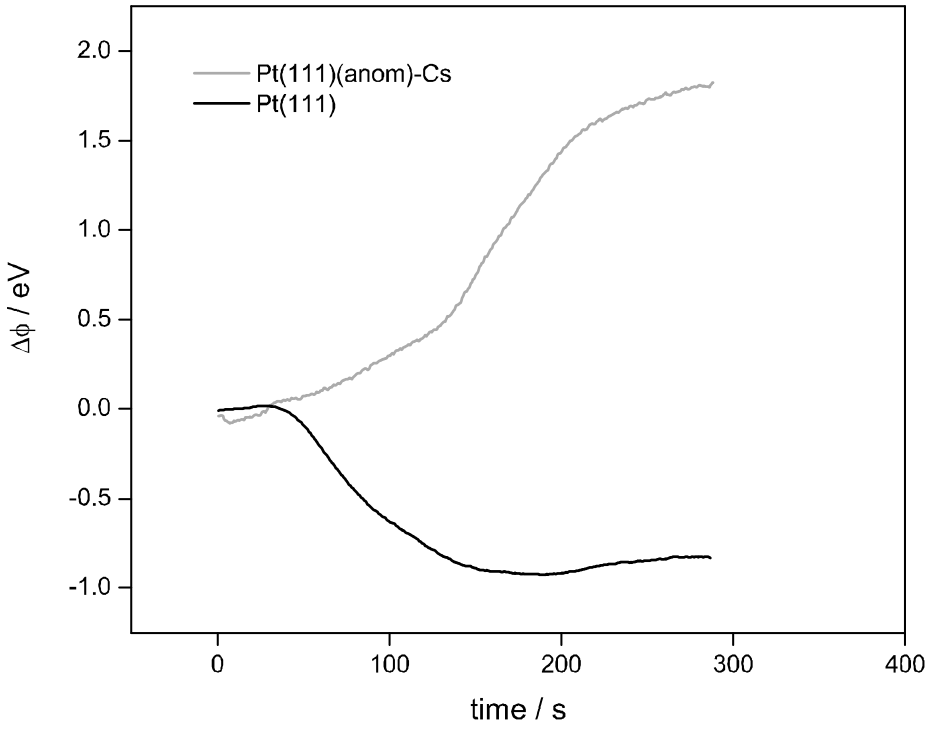

Figure 3.6: Work function response upon adsorption of iodine on clean Pt(111) (black) and Pt(111)(*anom*)-Cs (red) at 293 ± 5 K.

293 K, flash heating in vacuum to 1000 K, and then immediate cooling to 293 K gave reproducible results. We consider first the interaction of Pt(111)(*anom*)-Cs with iodine.

Work function measurement

The work function response upon iodine adsorption on Pt(111)(*anom*)-Cs at 293 K differs dramatically from the response in the Pt(111) case (Fig. 3.6). For clean Pt(111), the WF response to iodine adsorption is characterized by an initial drop followed by a slight increase and then a plateau at saturation. The saturated surface is

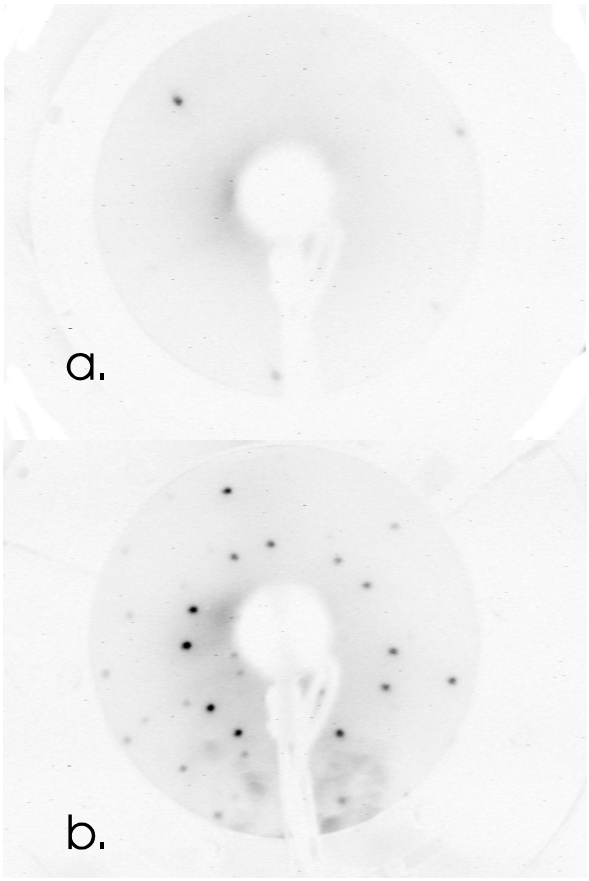

Figure 3.7: LEED patterns (100 eV, 0.01 μA beam current) (a) Pt(111)(*anom*)-Cs structure (b) and Pt(111)($\sqrt{7} \times \sqrt{7}$)R19.1°-CsI, prepared by dosing iodine on Pt(111)(*anom*)-Cs until no change in work function was observed.

known to be Pt(111)($\sqrt{7}\times\sqrt{7}$)R19.1°-I with a coverage of $\theta_{\mathrm{I}} = 0.43$ [36–39]. The work function change to the minimum is around 1 eV. However for the Pt(111)(*anom*)-Cs surface, the work function steadily *increases* by about 2 eV.

LEED, Auger and TDS measurement

Anomalously-adsorbed cesium produces a LEED pattern with poorly defined diffraction spots (Fig. 3.7a), indicating a poorly-ordered surface. Despite this, adsorption of iodine to saturation at 293 K on this surface yields a very sharp ($\sqrt{7} \times \sqrt{7}$)R19.1° LEED diffraction pattern (Fig. 3.7b), the same structure as is found for adsorption

on the clean Pt surface. AES measurements gave coverages of $\theta_{\mathrm{I}} = 0.37 \pm 0.05$ and $\theta_{\mathrm{Cs}} = 0.10 \pm 0.04$. The iodine coverage is in agreement with the ideal coverage of $\theta_{\mathrm{I}} = 3/7 = 0.43$ found for this structure on clean Pt(111). This structure consists of a close-packed layer of iodine atoms. The additional Cs atoms might replace iodine atoms in this layer, since the sum of the Cs and I coverages is also within error of 3/7. From the coverage data alone, we cannot distinguish this possibility from the alternative that the Cs is above or below this layer.

Thermal desorption spectra for I adsorbed on Pt(111)(*anom*)-Cs are shown in Fig. 3.8. The most interesting feature is the common peak at 560 K for all the measured masses (Cs, I and CsI). The presence of CsI in this desorption suggests the codesorption of Cs and I as CsI molecules or perhaps as larger clusters. This is the only desorption state for Cs, and is quite different from the desorption peak of Cs from the clean surface. The high temperature peak corresponding to anomalously adsorbed cesium is no longer observed. Evidently, a strong attraction between Cs and I weakens the Cs-Pt interaction and promotes a dramatic decrease in the desorption temperature for the Cs. The narrow desorption peak shape with sharp trailing edge is indicative of zero- or fractional-order desorption and is consistent with strong attractive interactions between adsorbed atoms or desorption from island edges [16]. From leading edge analysis, the desorption energy is $E_{\mathrm{d}} = 111 \pm 6$ kJ mol^{-1}.

The iodine TDS shows the CsI desorption peak, but is otherwise very similar to desorption from Pt(111)$(\sqrt{7} \times \sqrt{7})R19.1°$-I (Fig. 3.8 inset) suggesting that only a small fraction of I atoms are interacting with the Cs atoms.

The effect of adsorbed Cs on I adsorption was further probed by adsorbing iodine on Pt(111)(*anom*)-Cs at 953 K. At this temperature, the anomalously-adsorbed Cs is present on the surface but not desorbing, and iodine does not adsorb on the clean surface. As iodine is introduced, a Cs desorption signal is seen. Evidently the iodine has a transient existence on the surface, combines with the anomalously adsorbed Cs and desorbs as a $\mathrm{Cs}_x\mathrm{I}_y$ cluster.(Fig. 3.9).

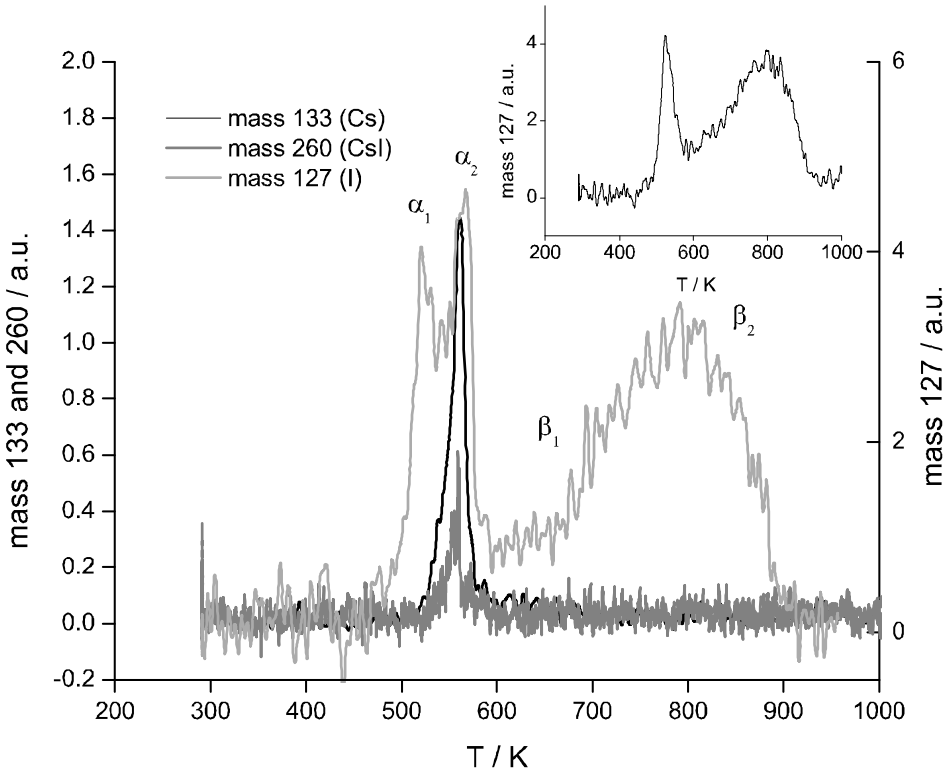

Figure 3.8: Thermal desorption spectra of mass 133 (Cs, black), 127 (I, light gray) and 260 (CsI, dark gray) from Pt(111)($\sqrt{7} \times \sqrt{7}$)R19.1°-CsI. Inset shows TDS spectrum of mass 127 (I) from Pt(111)($\sqrt{7} \times \sqrt{7}$)R19.1°-I. The Pt(111)($\sqrt{7} \times \sqrt{7}$)R19.1°-CsI structure was prepared by dosing iodine on Pt(111)(*anom*)-Cs until no change in work function was observed.

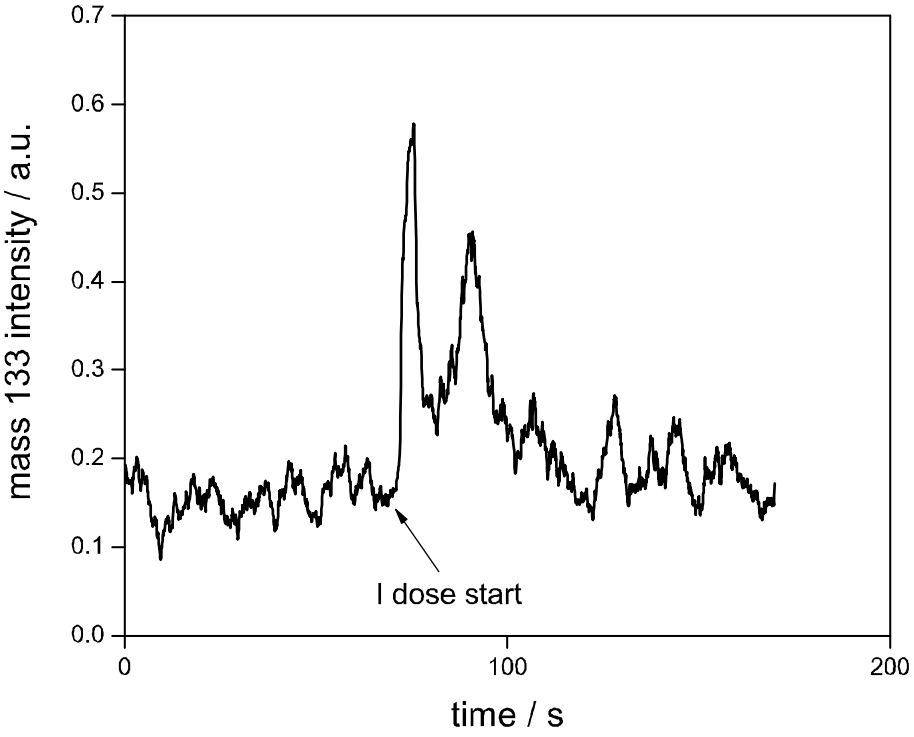

Figure 3.9: Mass 133 (Cs) signal response upon I adsorption on Pt(111)(*anom*)-Cs at 953 K. The fluctuation of the signal is caused by unstable I doser emission.

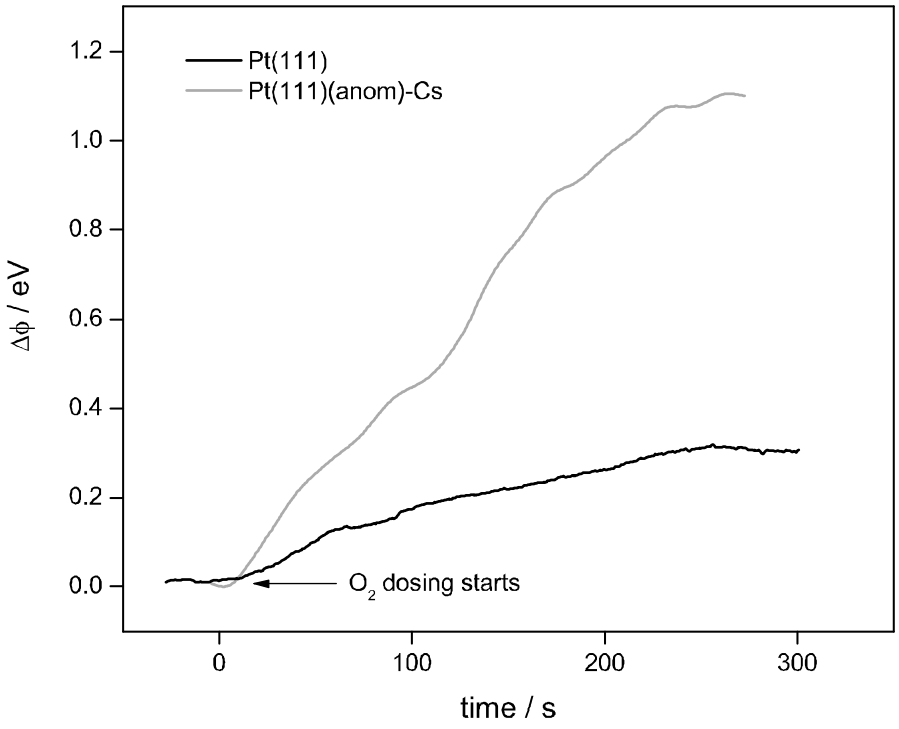

Figure 3.10: Work function response of O_2 adsorption on Pt(111)(*anom*)-Cs (grey) and Pt(111) (black) at 293 ± 5 K.

3.4.3 O adsorption on Pt(111)(*anom*)-Cs

Coadsorption with oxygen gives different behavior than for the I case. The work function still increases by around 1 eV during O_2 adsorption at 290 K (Fig. 3.10 grey curve) because, as usual, the introduction of an electronegative adsorbate increases the work function. However, during desorption the oxygen signal shows one broad feature (Fig. 3.11 grey curve) consisting of two peaks β_1 and β_2 with maxima at 592 K and 665 K respectively. The Cs signal (Fig. 3.12 grey curve) during O_2 desorption stays at its background value, i.e., Cs does not desorb together with O_2, which is in sharp contrast to the Pt(111)(*anom*)-CsI case.

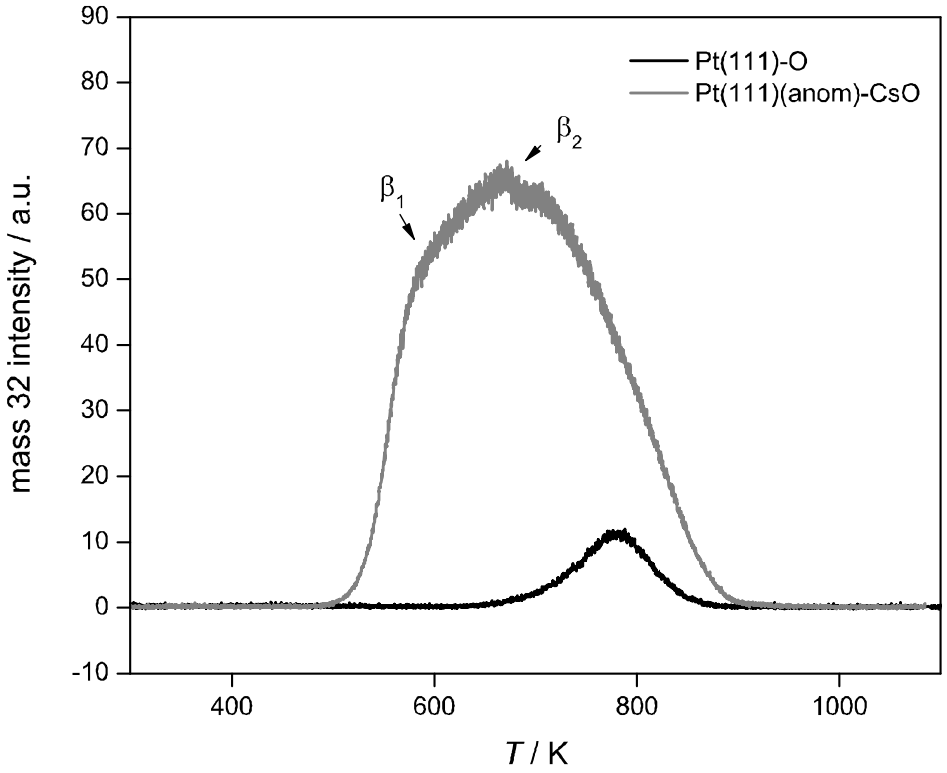

Figure 3.11: Mass 32 (O_2) TDS from Pt(111)(*anom*)-CsO (grey) and from Pt(111)-O surface (black). Heating rate $5\,\mathrm{K\,s^{-1}}$.

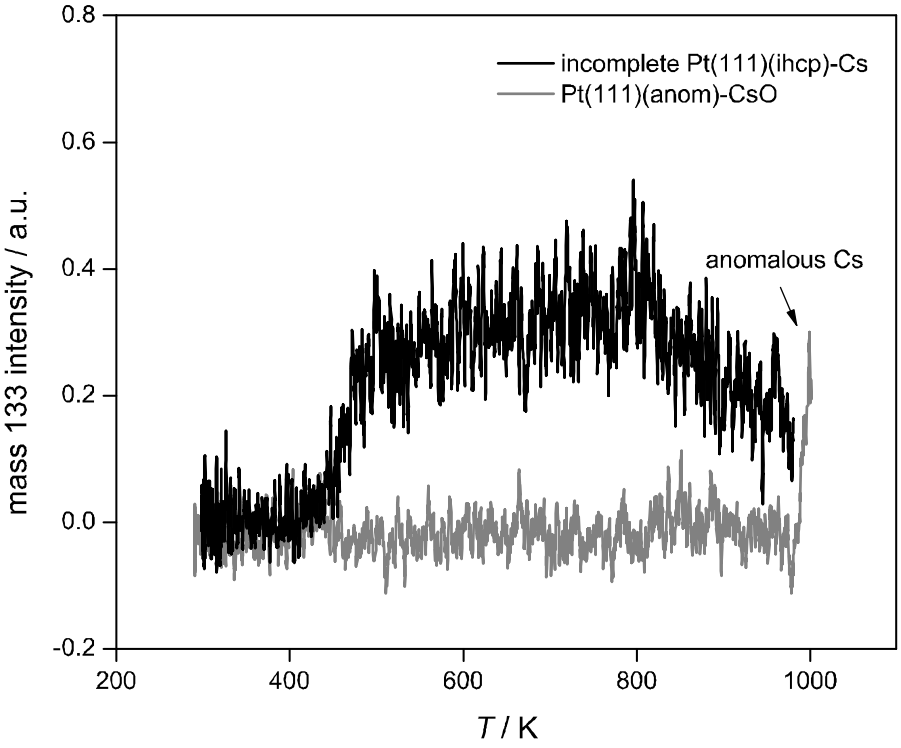

Figure 3.12: Cs TDS from Pt(111)(*anom*)-CsO (gray). TDS from incomplete Pt(111)(*ihcp*)-Cs (black) is shown for comparison. Heating rate 5 $\mathrm{K\,s^{-1}}$.

For comparison, we adsorbed oxygen on clean Pt(111) immediately after removing the CsO layer by annealing to 1150 K (Figs. 3.10 and 3.11). Comparison of the WF response for the different surfaces shows that the presence of anomalously-adsorbed Cs increases the slope of the work function response. Such an increase in WF slope can be caused by an enhanced sticking coefficient for oxygen or by a larger dipole moment in the adsorbed structure. The TDS spectra show that the peak maximum for O_2 desorption shifts to lower temperatures and increases in area if prepared from the Pt(111)(*anom*)-Cs surface. We conclude that although the Cs is not removed by oxygen, it dramatically enhances the amount of oxygen that can be adsorbed. We found that if the maximum temperature did not exceed 1000 K, cooling and readsorbing oxygen gave reproducible TDS spectra.

There is also a possibility of Si contamination of the surface which might affect surface properties towards O adsorption [26]. It has been recommended that Si impurities are oxidized prior to an experiment by exposing the crystal to oxygen and heating to high temperatures. In our experimental procedures, the surface has been oxidized and heated to at least 1000 K prior to each experiment involving adsorption and desorption of oxygen, therefore any effect of hidden Si impurities is unlikely.

3.5 Discussion

Our experiments clearly show anomalous adsorption of Cs on the Pt(111) surface for the first time. It occurs prior to the change in slope of work function when the Cs coverage reaches $\theta_{Cs} = 0.12$. Thermal desorption spectroscopy shows a high temperature peak that is suppressed by a negative voltage on the crystal. Further, a new surface with only anomalously adsorbed Cs could be prepared by heating the sample to 1000 K. The reactivity of this surface toward iodine and oxygen was studied. Both iodine and oxygen adsorption were accompanied by an increase of work function as expected for adsorption of electronegative species. The iodine causes the

anomalous Cs to desorb at 560 K in the form of Cs_xI_y clusters. Adsorption of O_2 on Pt(111)(*anom*)-Cs leads to a significant increase in the final oxygen coverage when compared to adsorption on clean Pt(111). The anomalously adsorbed Cs stays on the surface when oxygen is desorbed.

3.5.1 Nature of the high-temperature desorption peak

Lehmann [29] showed using crystal current, and comparison of filament on/off signals that the high-temperature desorption peak from K on Pt(111) was due to desorption of a charged species. In our case, the true crystal current was masked by an artifact, but applying a negative potential (−20 V) to the sample decreased the TDS signal to the baseline, indicating that the desorbing species is positively charged. Ions leaving the surface having climbed the desorption activation barrier will have kinetic energies comparable to the thermal energy, which at 1100 K is about 0.09 eV, much too small to escape the 20 eV electrostatic barrier.

We now show that the 180° phase shift in the modulated signal for this peak relative to normal operation is also evidence for a positive desorbing species. In the normal case of desorbing neutrals the modulation scheme works by switching the potential on the ion source: an "on" state of +3 V pushes the just-ionized positive ions into the quadrupole mass filter, and an "off" state of −2 V prevents the ions from entering the filter. On the other hand, a desorbing positively-charged species seeing the +3 V ion source will not enter the source, and no signal will be produced: the "on" state is really an off state for positively charged species. Conversely, the −2 V accelerates the positive ion into the source. The transit time of the ions through the mass filter and conversion to a current by the secondary electron multiplier is fast on the time scale of the modulation (47 Hz) and so the signal appears 180° phase shifted relative to the normal case of neutral desorption. The large size of this peak relative to the normal peak is a reflection of the fact that the positive ions proceed

by line-of-sight into the mass filter, whereas in a normal peak only a fraction of the neutrals are ionized.

The anomalous Cs desorbing in the high temperature TDS peak has an exceptionally high energy of desorption. A positively charge ion leaving the surface has to overcome the attraction to its image charge which for Cs^+ can be estimated as 210 $\mathrm{kJ\,mol^{-1}}$ (initial separation from image charge estimated as twice the Pauling ionic radius of 1.67 Å). This energy is on top of any covalent contribution in the bond. Although this latter contribution is unknown, for the purposes of an estimate we take it the same as for Pt(111)(2×2)-Cs, 166 $\mathrm{kJ\,mol^{-1}}$, which then makes the total estimated desorption energy to be around 380 $\mathrm{kJ\,mol^{-1}}$. This prediction is comparable to the measured desorption energy of 456 ± 21 $\mathrm{kJ\,mol^{-1}}$ (leading edge analysis) for anomalously adsorbed Cs.

3.5.2 Coverage

We determine the Cs coverage for Pt(111)(*anom*)-Cs structure by three different methods. Assuming a constant sticking coefficient, a Cs coverage of 0.15 ± 0.03 is found from the time to the work function break. Furthermore, the Cs coverage for Pt(111)(*anom*)-Cs prepared by annealing Pt(111)(*ihcp*)-Cs to 1000 K is 0.12 ± 0.03 from AES measurement. A third estimate of θ_{Cs} comes from analyzing the low temperature Cs TDS peaks as follows.

Details of the low temperature TDS peaks from Pt(111)(2×2)-Cs (red, $\theta_{\mathrm{Cs}} = 0.25$) and Pt(111)(*ihcp*)-Cs (black, $\theta_{\mathrm{Cs}} = 0.41$) are shown in Fig. 3.3. The starting point of both TDS spectra is at the known coverage determined from the LEED structures. The assumption is that the number of atoms desorbing in the low temperature peak depends on the initial coverage of surface, but the number of atoms desorbing in the high temperature peak is the same for both starting structures. The sum of the Cs coverages desorbing at low and high temperature peaks gives the total amount of

adsorbed atoms for each structure, Eqs. (3.1), (3.2).

$$0.41 = \theta_{\text{low},0.41} + \theta_{\text{Cs,anom}} \quad (3.1)$$

$$0.25 = \theta_{\text{low},0.25} + \theta_{\text{Cs,anom}} \quad (3.2)$$

Now, the desorbing coverage at low temperatures, θ_{low}, is proportional to the integrated TDS peak area I.

$$0.41 = \alpha I_{\text{low},0.41} + \theta_{\text{Cs,anom}} \quad (3.3)$$

$$0.25 = \alpha I_{\text{low},0.25} + \theta_{\text{Cs,anom}} \quad (3.4)$$

$I_{\text{low},0.41}$ and $I_{\text{low},0.25}$ correspond to the peaks for coverage 0.25 and 0.41 respectively and α is scaling a factor characteristic of our UHV system geometry.

Solving the two equations for the two unknowns α and $\theta_{\text{Cs,anom}}$ gives the coverage 0.15 ± 0.04 for Cs desorbing above 1000 K. This calculated $\theta_{\text{Cs,anom}}$ is the same within experimental error as the coverage estimated from AES measurement and from the work function break. Overall there is good agreement between these three values.

$\theta_{\text{Cs, anom}}$ found from the break of work function is expected to be an slight underestimate as the assumption of constant sticking coefficient has been suggested to be not valid [29].

AES coverages were also determined for Pt(111)$(\sqrt{7}\times\sqrt{7})R19.1°$-CsI ($\theta_{\text{I}} = 0.37 \pm 0.05$, $\theta_{\text{Cs}} = 0.10 \pm 0.04$). These coverages, together with integrals of TDS peaks from Pt(111)$(\sqrt{7}\times\sqrt{7})R19.1°$-CsI, can be used to estimate the possible stoichiometry of the desorbing Cs_xI_y clusters. According to Labayen et al. [45], the total iodine coverage desorbed between $400 - 600$ K is 0.10 for Pt(111)$(\sqrt{7} \times \sqrt{7})R19.1°$-I prepared from I_2 on the clean surface. However, further analysis shows that a significantly lower number of I atoms are directly involved in the Cs_xI_y desorption. The peak observed at 560 K in our work overlaps with the small α_2 peak from Labayen's work [45] (in

the following we will use the same peak notation as in ref. [45]). In our case, the enhancement of α_2 peak intensity must come in at the expense of the other peaks. From the comparison with Pt(111)($\sqrt{7} \times \sqrt{7}$)R19.1°-I TDS, the peak height ratio α_1/β_2 does not seem to be significantly affected. All of the I atoms desorbing at 560 K come from the feature β_1 located at the onset of the β_2 peak. By subtracting the α_2 peak from the spectrum, the coverage of adsorbed iodine which is not in direct interaction with anomalously adsorbed Cs can be found. Integration of the subtracted TDS spectrum gives $\theta_{\mathrm{I}} = 0.35 \pm 0.02$, which is only slightly less than the total coverage $\theta_{\mathrm{I}} = 0.37 \pm 0.05$ of Pt(111)($\sqrt{7} \times \sqrt{7}$)R19.1°-CsI as measured by AES. Therefore the coverage of iodine which is desorbing with Cs can be estimated to be about 0.02 ± 0.07. The measured coverage of anomalously adsorbed Cs in Pt(111)($\sqrt{7} \times \sqrt{7}$)R19.1°-CsI structure is $\theta_{\mathrm{Cs}} = 0.10 \pm 0.04$ and it can be concluded that Cs and I atoms are desorbing in $\mathrm{Cs}_x\mathrm{I}_y$ clusters with $x/y \geq 1$. The error in this estimate is rather high so even a $\mathrm{Cs}_1\mathrm{I}_1$ cluster is possible. Given the low coverage of Cs relative to I, desorption of CsI clusters seems more likely than those richer in Cs.

The measured AES coverage of Pt(111)($\sqrt{7} \times \sqrt{7}$)R19.1°-CsI shows that the I coverage is lower compared to Pt(111)($\sqrt{7} \times \sqrt{7}$)R19.1°-I. We propose that this missing iodine is substituted by previously anomalously adsorbed Cs and together with the rest of iodine forms ($\sqrt{7} \times \sqrt{7}$)R19.1° structure. This is supported by the fact that adding θ_{I} and θ_{Cs} gives the total coverage of 0.47 ± 0.06 which is comparable within experimental error to the ideal coverage of 0.43 for the Pt(111)($\sqrt{7} \times \sqrt{7}$)R19.1°-I structure. The maintenance of the same ($\sqrt{7} \times \sqrt{7}$)R19.1° structure for both surfaces with and without Cs argues for random substitution rather than islands of Cs.

3.5.3 Work function

The work function behavior for Cs adsorption reported here closely resembles the behavior for K adsorption on Pt(111) [29]. We observe a characteristic break in

WF at low coverages even at an adsorption temperature of 100 K. Other groups measuring the work function for Cs adsorption did not report the break. The Kelvin probe used here has higher resolution than the other WF measurement methods used, where such fine features could be lost in the coarse-grained data [34, 40, 41]. Furthermore, the literature work function change at the minimum was measured as 4.8 eV, whereas we have measured values in the range $4.0 - 5.5$ eV. We believe the higher values represent cleaner surfaces, and suggest that failure to remove all Cs atoms between experiments by insufficient heating may cause some of this variability. Residual anomalous Cs would lower the work function change and mask the expected change in slope.

To understand the origin of the WF break, we refer to the STM study of Yamada et al. [34]. This study of Cs adsorption on Pt(111) found two different adsorption states for $\theta_{\mathrm{Cs}} < 0.10$ seen as "depression" regions with apparently reduced height. The small depressions were considered as adsorption of single Cs atoms, whereas larger depressions were assigned to adsorption of several Cs atoms. The apparent change in height was explained by ionic adsorption and charge transfer to the substrate. Interestingly, they found the Local Tunneling Barrier Height (LBH) to be significantly decreased for larger depressions, but no apparent change in LBH for small depressions. The LBH is proportional to local work function, and a mix of the two populations of depressions would lead to a work function decrease that would only fortuitously be linear with coverage. It is worth noting that subsurface Cs atoms, a possibility considered for K [29], would likely lead to an *increase* in work function, or very little change at all due to screening of the charge of the subsurface species by the surface layer of metal atoms. An inverted dipole moment for subsurface species has been demonstrated before, e.g., for subsurface O in Zr(0001) [46].

For $\theta_{\mathrm{Cs}} \approx 0.10$, close to where we observe the break in WF, Yamada at al. saw the formation of unstable (2×2) islands with further decreased LBH. At a similar or slightly higher coverage ($\theta_{\mathrm{Cs}} = 0.14$), LEED studies by Tűshaus et al. [47] and Riwan

et al. [40] saw emergence of Pt(111)($\sqrt{7} \times \sqrt{7}$)R19.1°-Cs LEED patterns. While this pattern is consistent with an ideal $\theta = 1/7$ structure at close to the observed coverage, it is more likely due to islands of a more densely packed structure. These studies are consistent with disordered anomalously adsorbed Cs up to the work function break, at which point ordered phases appear. Our LEED measurements also show only diffuse patterns (Fig. 3.7 a.) for Cs coverages below about 0.12 ML.

Lehmann [29] suggests that the break may be lifting of a reconstruction, but a 2-D gas to 2-D solid type of phase transition would also explain the results; we require only that the dilute anomalously-adsorbed Cs has a lower dipole moment than the ordered phase that first appears at the break.

We consider now the origin of the WF change for coadsorption of I and O with anomalous Cs. It is clear from our experiments that even a small amount of adsorbed Cs can drastically change the surface properties towards I adsorption. In the case of I adsorption on the Pt(111)(*anom*)-Cs surface we see a WF increase. Therefore there must be significant electronic charge transfer towards the iodine, forming dipoles of opposite polarity than the Cs induced dipole [14,15]. This is the expected direction for an electronegative adsorbate like I. Note that on a clean Pt surface, iodine adsorption leads to an initial decrease in work function due to its polarizability (similar to the decrease for non-polar Xe on Pt) that overwhelms the weak electronegativity until the coverage is higher. We conclude that the presence of anomalous Cs on the surface increases the ionicity of Pt-I bond. Similar reversal of a dipole moment was observed for the coadsorption of cyclohexane and Cs on Pt(111), but in that case it was thought to be due to high polarizability of cyclohexane [48].

Adsorption of oxygen on either Pt(111)(*anom*)-Cs or clean Pt leads to an increase in work function, as expected for an electronegative adsorbate. The overall slope of the WF response is enhanced for the anomalous surface, but from our experiments we cannot decide on the origin of this behavior. It could be due to the enhancement of charge transfer caused by anomalous Cs as in the I adsorption case, or due to an

increased maximum O coverage or both.

3.5.4 Nature of the anomalously-adsorbed state

For K on Pt(111), Lehmann [29] showed that there was a phase transition of some type at a critical coverage of $\theta_K \approx 0.22$, as evidenced by the qualitative change in the slope of the work function or the shape of Xe photoemission peaks at that coverage. That coverage also corresponded to the coverage of a high-temperature thermal desorption peak, which was identified as desorption of positively charged K^+ from the surface. Lehmann argued for incorporation of the K into the Pt surface in some way, perhaps interstitial incorporation, since the activation energy appeared low, with facile incorporation even at 100 K. Wenter et al. [31] used LEIS to verify the phase transition, but were unable to distinguish subsurface incorporation from normal adsorption with an enhanced sticking coefficient. Hannon et al. used vibrational EELS to argue for subsurface K [30], but the same group later showed that the species present was KOH formed by reaction of K with water in the residual gas [32]. The upward buckling observed by STM attributed to the presence of subsurface K [30] may have other explanations. Theoretical calculations were not definitive: DFT cluster calculations carried out by Hannon et al. [30] suggested possible subsurface adsorption, but tensor LEED analysis (using intensity-voltage curves) and DFT slab calculations by More et al. [49] found no signs of K incorporation into the lattice for Pt(111)(2×2)-K. Existing evidence for incorporation of K into the Pt surface is indirect, and we defer the final conclusion on the nature of the state in that case. We argue, however, that in our case Cs incorporation is much more unlikely due to the large size of the Cs atom compared to K and also because we observe the anomalous WF break at low temperatures where thermal energy is not sufficient for surface reconstruction during incorporation. Size dependent behavior *was* observed for substitutional adsorption of alkali metals on Al(111) [50], where the smaller size atoms Na, K and Rb adsorbed substitutionally, but the larger Cs atoms adsorbed on

top of Al(111).

We conclude that the anomalously adsorbed state is probably a normally adsorbed species, whose charge state is distinct from that found at higher coverages. The presence of ordering at the break coverage suggests that there is a phase transition, perhaps from a state with purely repulsive lateral interactions to a state with attractive next-nearest neighbor interactions. It does not seem to be necessary to postulate lattice incorporation, alloying or subsurface sites, though these possibilities cannot be excluded based on the data given here.

3.5.5 Coadsorption of cesium with iodine or oxygen

As already discussed, coadsorption of anomalously adsorbed Cs does not affect the structure and coverage of adsorbed iodine in a significant way. The Cs appears to substitute for I on the Pt(111)$(\sqrt{7} \times \sqrt{7})R19.1°$-I overlayer, but desorbs at a much lower temperature (560 K) than in the absence of iodine. The hold experiment at 953 K clearly shows that I is responsible for Cs desorption at the lower temperatures. All of the cesium leaves the surfaces at the same time as iodine as confirmed by the disappearance of the anom-Cs TDS peak. Evidently, a strong Cs-I interaction weakens the attraction of the Cs to the surface.

In contrast, the coadsorption of oxygen with the anomalously adsorbed Cs does not change the desorption temperature for Cs, but does significantly enhance the amount of oxygen that can adsorb on the surface. However, the amount of oxygen that can adsorb on the clean Pt(111) shows some variability, both in our results and in the literature, so we discuss this in some more detail.

We observe some variation in work function response from experiment to experiment depending on the history of sample and on the cleaning procedure. Generally we find that even after 700 min of O_2 dosing on Pt(111) the layer does not seem to be saturated. We also measure a higher than previously reported overall work

function change of about $0.20 - 0.50$ eV. In the work of Derry et al. [51], the work function was found to be rising slowly even after 1500 s of O_2 dosing at 2.6×10^{-6} Pa (28 L) and 300 K, though the work function change was only about 0.15 eV, much less than we observed. Other literature values for work function change are also not consistent [52, 53].

Concomitantly, the amount of oxygen that can be adsorbed on nominally clean surfaces also shows variability. The black curve in Fig. 3.11 shows TDS of O_2 from Pt(111)-O obtained directly after desorption of anomalously adsorbed Cs. It is characterized by a symmetric peak at 780 K and agrees well with results measured by other groups on Pt(111)-O for coverages $\theta_O < 0.25$ [54–56]. However, we observed significant variation in the TDS peak height and a slight shift of the peak maximum, depending on the history of the sample. Therefore, calibration of oxygen coverages by AES was unreliable due to the uncertainty in the reference structure's coverage, which should be the saturated Pt(111)(2×2)-O structure with nominal coverage $\theta_O = 0.25$ [56, 57]. As the coverage decreases, the O_2 TDS peak decreased in intensity and the maximum shifted to higher temperatures, as also observed by Szabo et al [56]. Therefore we conclude that there is some variability in coverage, which may be associated with defects or impurities.

The O_2 TDS spectra measured here from the Pt(111)(*anom*)-CsO surface are similar to those found by other groups for oxygen adsorption on modified Pt(111) surfaces for coverages $\theta_O > 0.25$. These higher coverages can be obtained in various ways, aside from the variability alluded to above. Higher oxygen coverages up to $\theta_O = 2.9$ can be obtained by using aggressive oxidants, dissociative chemisorption of NO_2, or atomic oxygen beams [54, 57]. The O_2 TDS spectrum from a Pt(111)-O surface with coverage $\theta_O = 0.57$ prepared by an atomic oxygen beam [57] is almost identical to the O_2 TDS from Pt(111)(*anom*)-CsO measured here .

There are two main features β_1, β_2 visible on the spectra for Pt(111)(*anom*)-Cs. The notation here follows the notation in [57]. According to Devarajan et al., for

coverages $0.25 < \theta_O < 0.50$ oxygen arranges into $p(2\times1)$ domains giving rise to the β_2 peak [58]. Coverages $0.50 \leq \theta_O < 0.75$ are explained by Pt-oxide chain development and correspond to the β_1 peak. The onset of formation of a Pt-oxide chain structure was observed for coverages around $\theta_O = 0.40$. In our case, β_1 peak is not very well defined and its height is dependent on the amount of anomalously adsorbed Cs (data not shown). The maxima for the β_1 and β_2 desorptions are at 592 K and 665 K respectively, similar to the TDS spectra measured by Weaver et al. [57]. They measured the β_1 peak around 600 K and the β_2 peak maximum changing from 650 K − 680 K as the O coverage decreased. We found desorption energies of $E_d = 149 \pm 1$ kJ mol^{-1} (leading edge analysis), $E_d = 154$ kJ mol^{-1}(Redhead analysis) for the β_1 peak and $E_d = 173$ kJ mol^{-1} (Redhead analysis) for the β_2 peak. Weaver et al. found desorption activation energies by leading edge analysis from desorption traces for $\theta_O > 0.25$ changing from 188 to 109 kJ mol^{-1} as the O coverage increased, which are comparable to those found for our β_1 desorption peak.

Direct comparison can be also made between our Pt(111)(*anom*)-CsO TDS measurement and the TDS reported by Garfunkel and al. for Pt(111)-KO [5]. They measured both K and O_2 TDS for different initial K coverages in the KO layer. Their O_2 TDS shows one asymmetric peak with the maximum at about 650 K for low potassium coverages (therefore anomalously-adsorbed potassium). The shape is only slightly different from our observations. The main difference is that the peak tail extends to 1000 K. However, the most likely explanation for this tail is the use of significantly higher heating rates (30 K s^{-1}) in [5]. The similarity between O coadsorption with anomalously adsorbed K and Cs is not a surprise as both systems reveal similar adsorption behavior and electronic structure.

The overall similar TDS shape of the Pt(111)(*anom*)-CsO and Pt(111)-O prepared by atomic O beam points to a similar nature of the Pt-O bond on these two surfaces. We speculate that dramatic increases in oxygen coverage for Pt(111)(*anom*)-Cs can be linked to a long range modification of surface electronic structure caused by anom-

alously adsorbed Cs. Further supporting evidence for long range changes in electronic structure were also found by measuring local tunneling barrier height (LBH) upon Cs adsorption on Pt(111) [34].

3.6 Conclusions

The initial stages of adsorption of Cs on Pt(111) surface follow the behavior of K on Pt(111) at low coverages, the so-called anomalous adsorption state. This is characterized by a distinct work function response upon adsorption and by a high temperature TDS peak consisting of desorbing positively charged Cs^+ ions. It also dramatically changes the adsorption behavior of both iodine and oxygen. We suggest that the change in slope of work function that defines the end of the anomalously-adsorbed state is a phase transition to an ordered phase with a different charge state. This explanation and the fact that the large size of Cs compared to K makes lattice incorporation much less likely, argue against previous explanations involving lattice incorporation, surface alloying or subsurface sites. The latter explanation would also appear to be inconsistent with the sign of the work function change.

We find that the coverage of oxygen on Pt(111)(*anom*)-Cs surface is dramatically higher than on the clean surface. This effect may have consequences in heterogenous catalysis involving breakage of the O_2 bond. Anomalously adsorbed Cs may lower the activation barrier for O_2 dissociation, and yet the Cs-O interaction appears to be weak enough that subsequent reaction of adsorbed O with other species would not be inhibited. Furthermore the Cs is not easily removed from the surface. Therefore Pt(111)(*anom*)-Cs seems to be a good model catalyst for further investigation.

3.7 Acknowledgements

This work was financially supported by the Natural Sciences and Engineering Research Council (NSERC) of Canada.

Chapter 4

Coadsorption of Cs and I on Pt(111): Structure and ionicity[1]

4.1 Abstract

Coadsorption of Cs and I on Pt(111) has been studied with Low Energy Electron Diffraction, Auger Electron Spectroscopy and Thermal Desorption Spectroscopy. By adsorbing I on a Cs layer with saturation coverage (with an incommensurate hexagonal close packed structure), two distinct structures were prepared. First, Pt(111)(4×4)-Cs,I was observed after dosing until the the work function had increased by 1eV. By further I dosing, the structure changed to mixed islands of Pt(111)$(\sqrt{3} \times \sqrt{3})R30\,^{\circ}$-Cs,I and Pt(111)$(\sqrt{7} \times \sqrt{7})R19.1\,^{\circ}$-Cs,I. The Pt(111)$(4 \times 4)$-Cs,I was assigned to a Cs_2I 2D ionic crystal. In this structure, the total coverage is $\theta = 0.56$ monolayers (ML). One third is iodine ($\theta_{\mathrm{I}} = 0.19$ ML) and 2/3 is cesium ($\theta_{\mathrm{Cs}} = 0.37$ ML). The assignment of the observed structure was consistent with the predictions of a simple electrostatic model.

[1] Slightly revised version of a manuscript submitted to Surface Science, Jan 2010.

4.2 Introduction

The aim of this study is to prepare and to characterize adlayers of cesium and iodine that may be considered as 2D crystals of Cs,I on Pt(111), and explain the observed structures in terms of the bonding ionicity. In contrast to 3D ionic crystals, physical and structural properties of 2D ionic crystals have been less well studied. This is partly due to the lack of experimental techniques for preparation of these layers under Ultra High Vacuum (UHV) conditions. The importance of such research lies in understanding the relation between bonding and structure. In the case of well-ordered coadsorption structures, the structure is greatly affected by the nature of the bonds between the two types of atoms. Sometimes the structure is a mixed monolayer, in which the adsorbed atoms lie in the same plane; sometimes it is a bilayer, in which atoms of the two types are in separate layers. Some attempts to explain the structural behavior in terms of ionicity of the bonds were made by Wang et al. [18] and Labayen et al. [24]. It was proposed that partially ionic bonds between adsorbed atoms lead to a mixed overlayer [18]. Conversely, predominantly covalent bonds lead to bilayer structures [24].

Previously, underpotential deposition (UPD) has been used to study the coadsorption of halide anions during the electrodeposition of a metal monolayer to an electrode surface [18]. To some extent, these anion-metal surface structures could be considered either ionic or covalent. So far, the influence of composition and bonding on the formation of the layer is not very well understood. Unfortunately, the type of chemical bonding in these UPD structures is typically unknown. Cs structures cannot be made by UPD, but electrochemical coadsorption of Cs^+ with I^- on Au(111) in an electrochemical environment was studied by Bravo et al. using cyclic voltammetry, Auger Electron Spectroscopy (AES), X-Ray Photoelectron Spectroscopy (XPS) and Low Energy Electron Diffraction (LEED) [59]. They found that for potentials < -0.45 V, the overlayer forms a Au(111)(4×4)-CsI structure with $\theta_{Cs} = \theta_I = 0.25$ ML. At more

positive potentials, the structure changed to Au(111)$(\sqrt{3}\times\sqrt{3})R30\,^{\circ}$-Cs,I and then to Au(111)(5×3)-Cs,I with increasing θ_{I} and decreasing θ_{Cs}. The same general behavior was also observed for Cs and I coadsorption on Au(110) electrode studied by Scanning Tunneling Microscopy (STM) and Surface X-Ray Scattering (SXS) techniques respectively [22, 60]. At low potentials the mixed Au(110)(2×4)-Cs,I structure was observed in both cases. As the potential increased, the structure moved toward a pure iodine layer with no adsorbed Cs atoms. The model favoured for Au(110)(2×4)-Cs,I by Wang et al. consists of planar, mixed layers with 1:1 stoichiometry and atomic spacing almost identical to that in the bulk CsI crystal. The arrangement of atoms resembled those on a CsI(110) surface.

Stickney et al. immersed the Pt(111) surface in a KI solution and found that only structures with I adsorption were formed; no K adsorption was observed [61].

Here, we study coadsorption of Cs and I on Pt(111) in the gas phase. At saturation coverage at room temperature, Cs forms a hexagonal, close packed layer with rows of Cs atoms aligned with the [1,0] direction of the Pt(111) surface [40], previously referred to as Pt(111)(*ihcp*)-Cs (incommensurate hexagonal close packed) [62]. Iodine adsorption on this layer results in the formation of two new ordered surface structures having different LEED patterns. We found that this particular coadsorption system demonstrates both planar and bilayer behavior, even though it is expected to be significantly ionic. The second part of this work is devoted to the electrostatic interaction calculations of purely ionic layers which aid in understanding the general structural trends, as well as the unexpected bilayer formation. The observed behavior of the Pt(111)-CsI layer is interpreted in terms of the calculated electrostatic energies for different structures.

4.3 Experimental

The experiments were performed in a stainless steel UHV chamber with a base pressure of 1×10^{-10} mbar equipped with a Kelvin probe to measure work function (described in [33]), a quadrupole mass spectrometer (Hiden HAL 321) with a custom lock-in detection scheme for TDS [25] and an Omicron SPECTALEED single channelplate LEED optics used for LEED and also as a retarding field analyzer (RFA) for Auger Electron Spectroscopy (AES). The AES spectra were taken with a normal incidence 20 μA, 3 keV electron beam, and the TDS spectra were taken at a 5 $\mathrm{K\,s^{-1}}$ heating rate. A more detailed description of the system is provided in Ref. 62.

The platinum crystal used in this study was cut with a diamond-wafering saw from a single crystal grown by Metal Oxides and Crystals Ltd. After cutting, the surface was polished with successive grades of diamond paste (Beuhler Ltd.) and oriented to within 0.5° of the (111) plane by back Laue diffraction. The crystal was further polished using a 0.05 μm aluminium oxide slurry. The crystal cleaning procedure was the same as described in Ref. 62.

Experimental results on Pt can be affected by a significant concentration of impurities like silicon on the surface [26]. To avoid contamination, the crystal was periodically annealed at 1150 K in 5×10^{-7} mbar oxygen for 1 h. The contaminants segregated on the surface and formed stable oxides which were subsequently removed by Ar^+ bombardment. The effectiveness of the cleaning procedure was periodically checked by monitoring the AES oxygen signal after annealing in an oxygen atmosphere [62].

The starting Pt(111)(*ihcp*)-Cs structure was prepared using a SAES cesium dispenser (SAES Getters , Cs/NF/2.2/12 FT10+10) located 10 cm from the surface with dosing currents between $5.5 - 6.5$ A. The emitted Cs atoms were collimated by a stainless steel tube. The overall work function (WF) drop during Cs dosing varied from 4 eV to 5.5 eV. The variation is believed to be mainly caused by anomalously-

adsorbed Cs left from previous experiments. The surface must be annealed to 1150 K for at least 5 min in order to remove all anomalously adsorbed Cs from previous experiments [62]. Otherwise some Cs is still present on the surface after cleaning and this results in a decreased overall WF drop. If the maximum WF drop was below 4 eV, the layer was rejected for further investigation as being contaminated.

The Cs,I surface structures were prepared by dosing iodine from a solid state electrochemical cell formed from a Ag_4RbI_5 pellet [27]. The Pt(111)(*ihcp*)-Cs was first prepared by dosing Cs at ambient temperatures (295 ± 2 K) until no work function change was observed. Then the iodine (200 μA current through the pellet) was adsorbed at 295 ± 2 K and the WF was measured during dosing. When the WF reached the required change, the I doser was turned off and the doser collimator was blocked by a shutter. The sample was briefly heated to 350 K at 1 $\mathrm{K\,s^{-1}}$ to enhance surface diffusion and obtain sharper LEED patterns. The sample was then cooled down to 150 K and the LEED measurement was taken. The LEED pictures are presented as negative images to enhance apparent contrast.

The compositions for various Cs,I layers were obtained from AES spectra as described in [62]. All quoted errors are for a 95% confidence interval.

4.4 Results

4.4.1 Cs adsorption on Pt(111)

Fig. 4.1 shows the change in the surface work function of Pt(111) during the adsorption of the Cs monolayer at 295 K. First, the work function rapidly decreases with increasing Cs coverage. Around 3 eV there is a change of the WF slope and later the WF reaches a minimum which corresponds to a work function drop of about 5.3 eV. The magnitude of the overall work function drop, i.e., from the initial value to the minimum, is sensitive to the concentration of impurities at the surface and on the his-

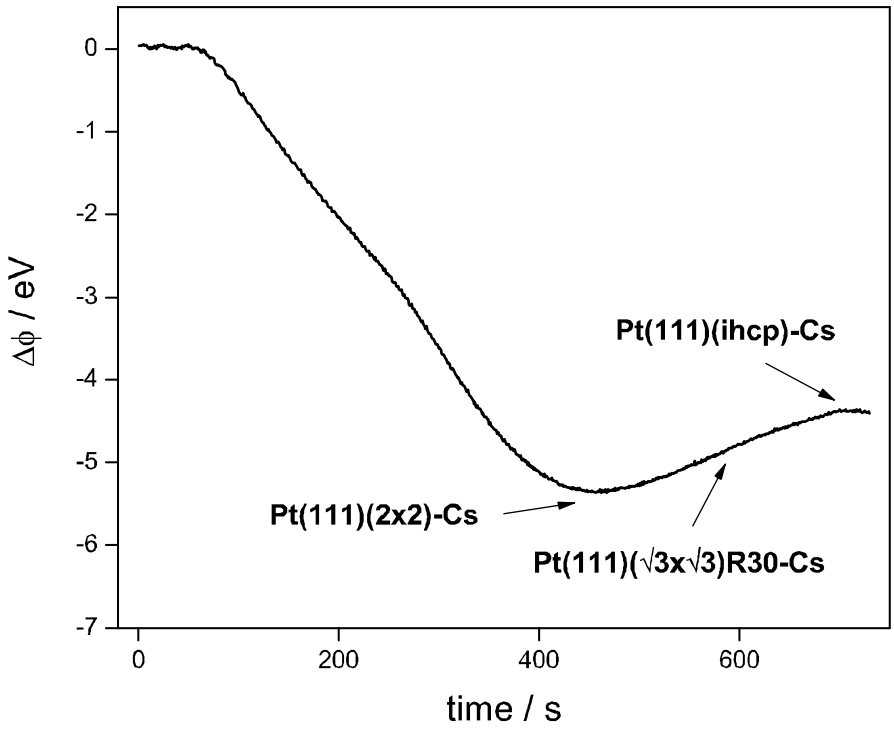

Figure 4.1: Work function change during Cs adsorption on Pt(111) at 295 K. The minimum corresponds to Pt(111)(2×2)-Cs. Upon further increasing the Cs coverage, the surface undergoes a phase transition to Pt(111)$(\sqrt{3}\times\sqrt{3})R30\,^{\circ}$-Cs and the work function increases. The saturation surface structure is Pt(111)$(ihcp)$-Cs with $\theta_{\mathrm{Cs}} = 0.41$.

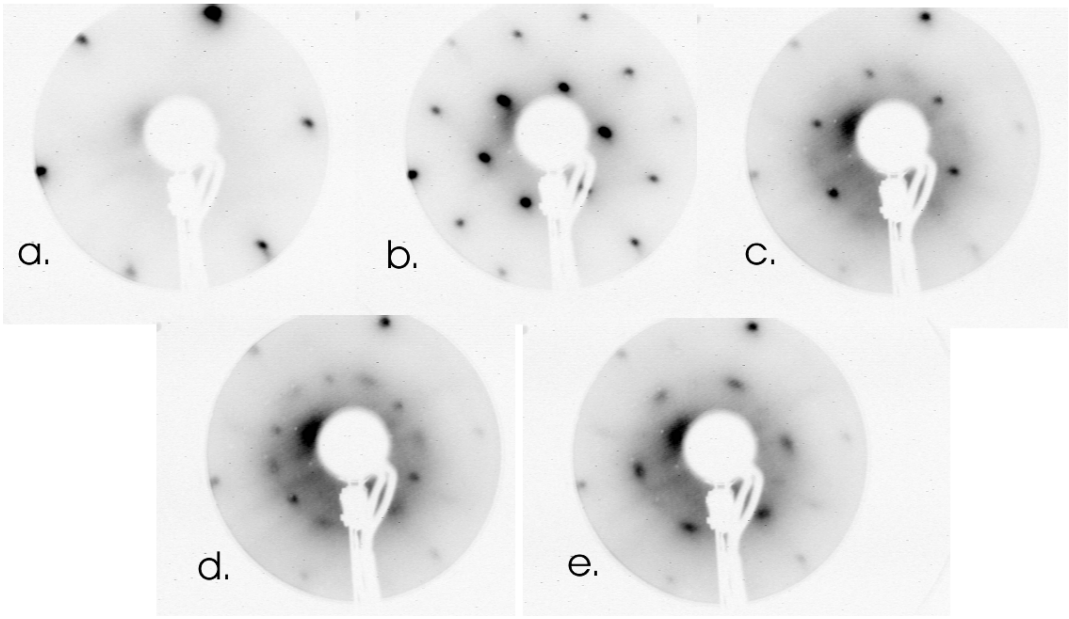

Figure 4.2: LEED patterns for Cs surface structures on Pt(111). The electron beam energy is 90 eV. a) Pt(111), b) Pt(111)(2×2)-Cs, c) Pt(111)$(\sqrt{3} \times \sqrt{3})R30\,^{\circ}$-Cs, d) mixed Pt(111)$(\sqrt{3} \times \sqrt{3})R30\,^{\circ}$-Cs and Pt(111)$(ihcp)$-Cs, e) Pt(111)$(ihcp)$-Cs.

tory of the sample. The change in the slope of the WF has been previously assigned to the phase transition between anomalously-adsorbed (Cs^{+}) and normally-adsorbed Cs adsorption states. [62].

The WF minimum corresponds to the formation of Pt(111)(2×2)-Cs ($\theta_{Cs} = 0.25$), Fig. 4.2b. Upon further Cs dosing the work function increases and the surface undergoes a phase transition to Pt(111)$(\sqrt{3} \times \sqrt{3})R30\,^{\circ}$-Cs ($\theta_{Cs} = 0.33$), Fig. 4.2c. Eventually, the Cs coverage reaches saturation ($\theta_{Cs} = 0.41$) where the structure is Pt(111)$(ihcp)$-Cs (Fig. 4.2e). Phase transitions are accompanied by the observation of mixed LEED patterns (Fig. 4.2d), suggesting the coexistence of homogenous islands of various phases at one particular coverage. The observed WF behavior and surface phase transitions correspond well with the data measured by other groups [34, 35, 41, 47].

4.4.2 I adsorption on Pt$(111)(ihcp)$-Cs

Adsorption of I on Pt(111)($ihcp$)-Cs causes the WF to increase (Fig. 4.3). This increase is accompanied by structural changes of the overlayer. For $\Delta\phi < 0.5$ eV, the LEED is diffuse. A new (4×4) LEED pattern (Fig. 4.4) is seen for $\Delta\phi$ in the range $0.5-$ 1.5 eV. The (4×4) pattern builds in from $\Delta\phi = 0.5$ eV, mixed with a diffuse pattern. The maximum coverage of the (4×4) structure occurs at about $\Delta\phi = 1$ eV. Further I dosing causes gradual reappearance of a diffuse pattern (presumably a different structure), and the (4×4)-Cs,I structure becomes less prominent. There is some inhomogeneity of the surface, with the (4×4) more or less prominent as the beam is moved across the surface. In the following, reference to the Pt(111)(4×4)-Cs,I surface corresponds to the structure formed by dosing I on Pt(111)($ihcp$)-Cs until $\Delta\phi \approx 1$ eV.

After further I dosing, the diffraction pattern changes to a mixture of Pt(111)$(\sqrt{3} \times \sqrt{3})R30\,^\circ$-Cs,I, Pt(111)$(3 \times 3)$-Cs,I and Pt(111)$(\sqrt{7} \times \sqrt{7})R19\,^\circ$-Cs,I patterns (Fig. 4.5c, d). The work function range where these phases coexist is $\Delta\phi = 2 - 2.5$ eV. Finally, the layer is saturated by I at $\Delta\phi = 2.5$ eV and the structure is now Pt(111)$(\sqrt{7} \times \sqrt{7})R19.1\,^\circ$-Cs,I (Fig. 4.5b) over the whole surface.

The surface composition for various CsI layers determined by AES were $\theta_{\mathrm{Cs}} = 0.35 \pm 0.11$, $\theta_{\mathrm{I}} = 0.28 \pm 0.07$ for Pt(111)(4×4)-Cs,I and $\theta_{\mathrm{Cs}} = 0.33 \pm 0.07$, $\theta_{\mathrm{I}} = 0.35 \pm 0.06$ for Pt(111)$(\sqrt{7} \times \sqrt{7})R19.1\,^\circ$-Cs,I. The AES spectrum for Pt(111)(4×4)-Cs,I is shown in Fig. 4.6.

We also used an alternative method for iodine coverage determination of Pt(111)(4×4)-Cs,I layer based on the iodine dosing time (Fig. 4.3). Assuming a constant sticking coefficient during dosing and the coverage of Pt(111)$(\sqrt{7} \times \sqrt{7})R19.1\,^\circ$-Cs,I as determined by AES, θ_{I} in Pt(111)(4×4)-Cs,I was found to be between $0.16 - 0.19$ for $\Delta\phi$ in the range of $1-$ 1.5 eV. This value was lower than the coverage of Pt(111)(4×4)-CsI determined by AES directly

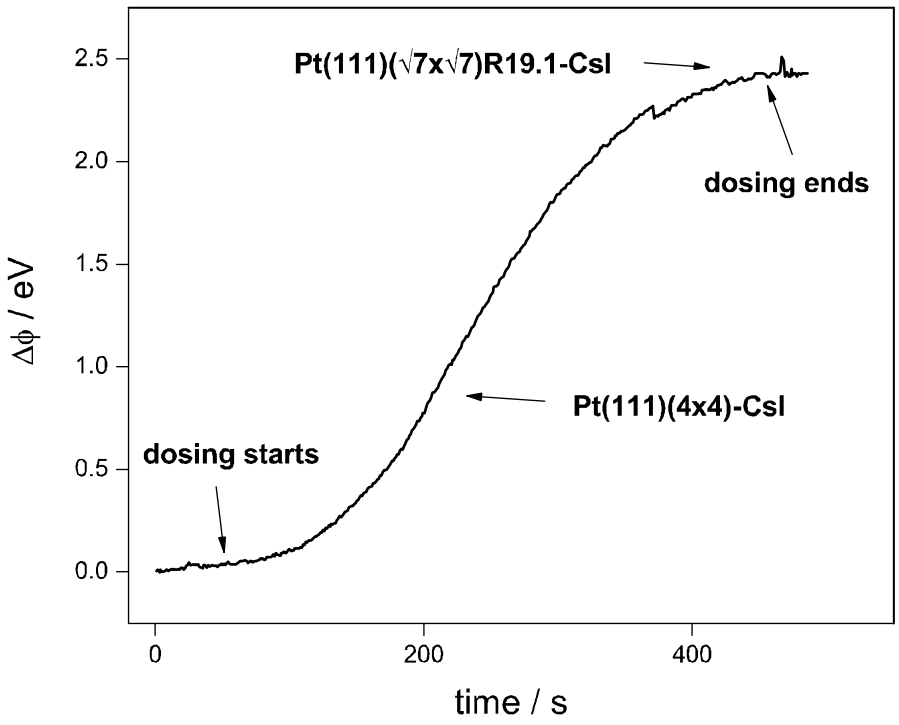

Figure 4.3: Work function change for I adsorption on Pt(111)(*ihcp*)-Cs at 295 K. As the work function change increases near 1 eV, a Pt(111)(4×4)-Cs,I structure is formed on the surface. Increasing the I coverage causes a further increase in work function and the structure changes through mixed Pt(111)($\sqrt{3}\times\sqrt{3}$)$R30\,^\circ$-Cs,I, Pt(111)(3×3)-Cs,I and Pt(111)($\sqrt{7}\times\sqrt{7}$)$R19.1\,^\circ$-Cs,I to saturated Pt(111)($\sqrt{7}\times\sqrt{7}$)$R19.1\,^\circ$-Cs,I.

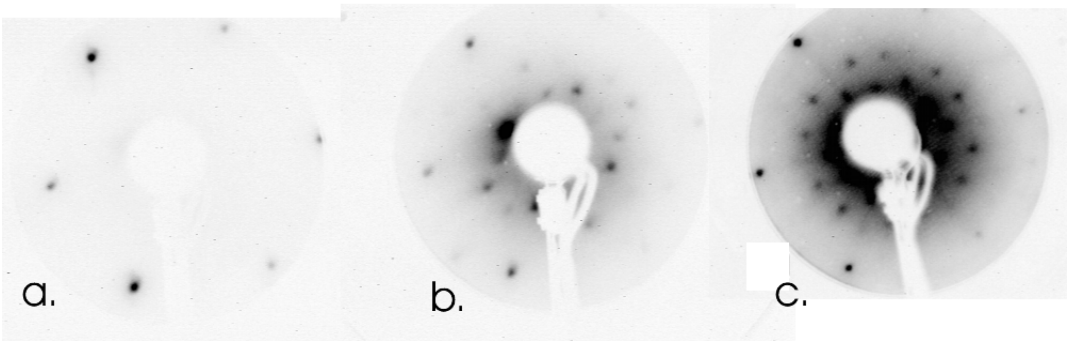

Figure 4.4: LEED patterns for the Pt(111)(4×4)-Cs,I structure formed by dosing I on Pt(111)(*ihcp*)-Cs. a) Pt(111), 99 eV, b) Pt(111)(4×4)-Cs,I, 99 eV, c) Pt(111)(4×4)-Cs,I, 92 eV.

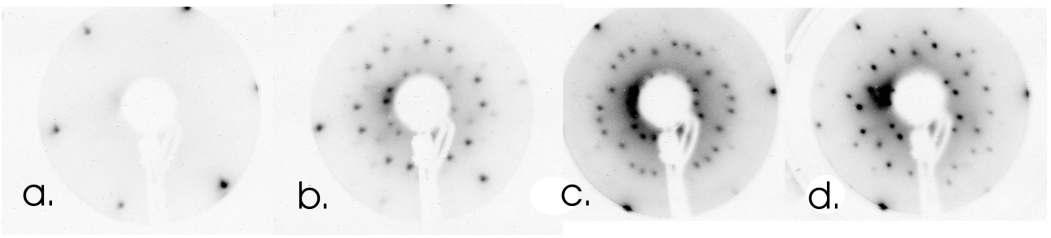

Figure 4.5: LEED patterns for Pt(111)-Cs,I layer close to saturation formed by dosing I on the Pt(111)(*ihcp*)-Cs. a) Pt(111), 90 eV, b) Pt(111)($\sqrt{7} \times \sqrt{7}$)R19.1 °-Cs,I at saturation, 90 eV, c) and d) transition structures observed for WF changes of $2 - 2.5$ eV. These structures were identified as mixed Pt(111)($\sqrt{3} \times \sqrt{3}$)R30 °-Cs,I + Pt(111)(3 × 3)-Cs,I + Pt(111)($\sqrt{7} \times \sqrt{7}$)R19.1 °, 77 eV and 81 eV respectively.

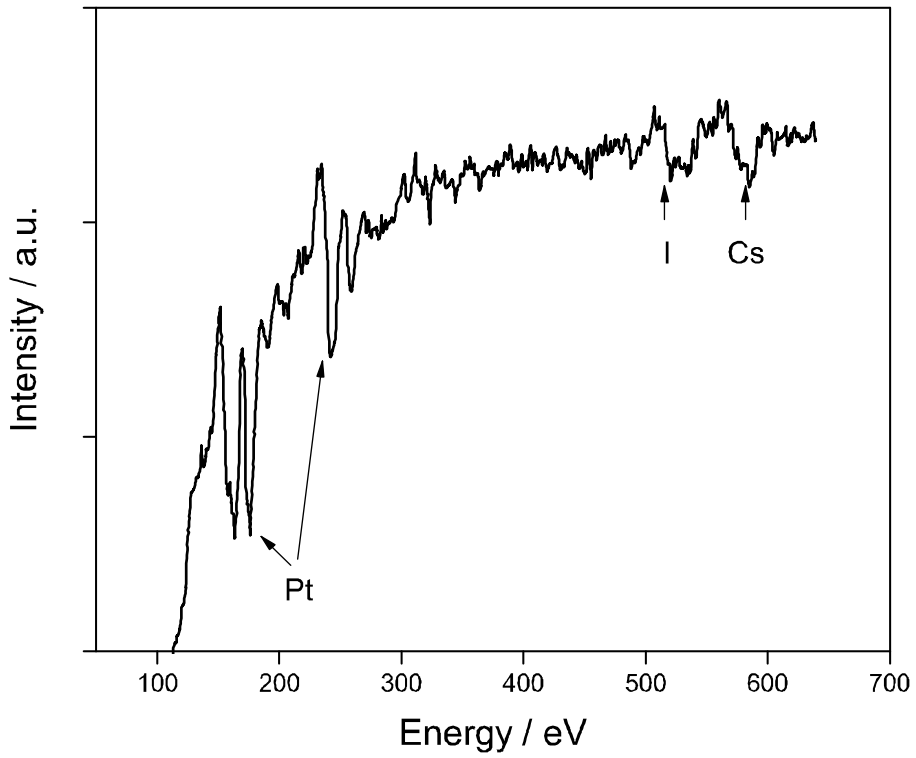

Figure 4.6: Auger spectrum of Pt(111)(4×4)-Cs,I. Auger peaks for Cs and I marked on the spectrum are well separated which allows AES coverage analysis.

The AES calibration has large errors for Pt(111)(4×4)-Cs,I because the surface composition when $\Delta\phi \approx 1$ eV can differ from experiment to experiment. Attempts were made to measure the AES spectra on an area of the crystal where the (4×4) LEED pattern was most pronounced, but the beams at the two energies may hit the crystal at different locations, and likely not the location where the work function change was measured. During the long time for the AES measurement, there was some interconversion of Pt(111)(4×4)-Cs,I to Pt(111)$(\sqrt{7}\times\sqrt{7})R19.1\,^{\circ}$-Cs,I, probably due to increased adsorption of iodine from the residual gas. This results in a systematic error towards higher I and lower Cs coverages. It may also be that the 1 eV surface is not where the ideal (4×4) structure occurs. The AES coverages for Pt(111)$(\sqrt{7} \times \sqrt{7})R19.1$-Cs,I are significantly more reliable because the layer is saturated with I.

Fig. 4.7 shows the TDS for various masses from the saturation Pt(111)$(\sqrt{7} \times \sqrt{7})R19.1°$-Cs,I structure. The iodine TDS spectra is very similar to the iodine TDS from Pt(111)$(\sqrt{7} \times \sqrt{7})R19.1°$-I surface (Fig. 4.8 inset) [45]. The only difference is the additional sharp peak at 600 K, which is also seen for masses 133 (Cs) and 260 (CsI). It can be concluded that Cs and I desorb from the surface simultaneously in the form of Cs_xI_y clusters. The high-temperature end of the Cs desorption is the beginning of the large anomalous Cs peak, in which a small amount of Cs desorbs as Cs^+. All three spectra share features with the spectra from Pt(111)-Cs,I prepared by dosing I on the lower-coverage Pt(111)(*anom*)-Cs surface (surface covered with anomalously adsorbed Cs) [62].

TDS spectra from the Pt(111)(4×4)-Cs,I layer are shown in Fig. 4.8. Again, the spectra are characterized by a sharp peak with a maximum at 595 K for all three measured masses. The mass 127 (I) TDS spectrum differs significantly from the spectrum measured from Pt(111)$(\sqrt{7} \times \sqrt{7})R19.1°$-I (Fig. 4.8 inset), reflecting the lower iodine coverage. The high temperature broad peak near 800 K is missing and almost all I desorbs in the sharp peak though there is a long tail extending to higher temperatures. The mass 133 (Cs) desorption shows the same peak as

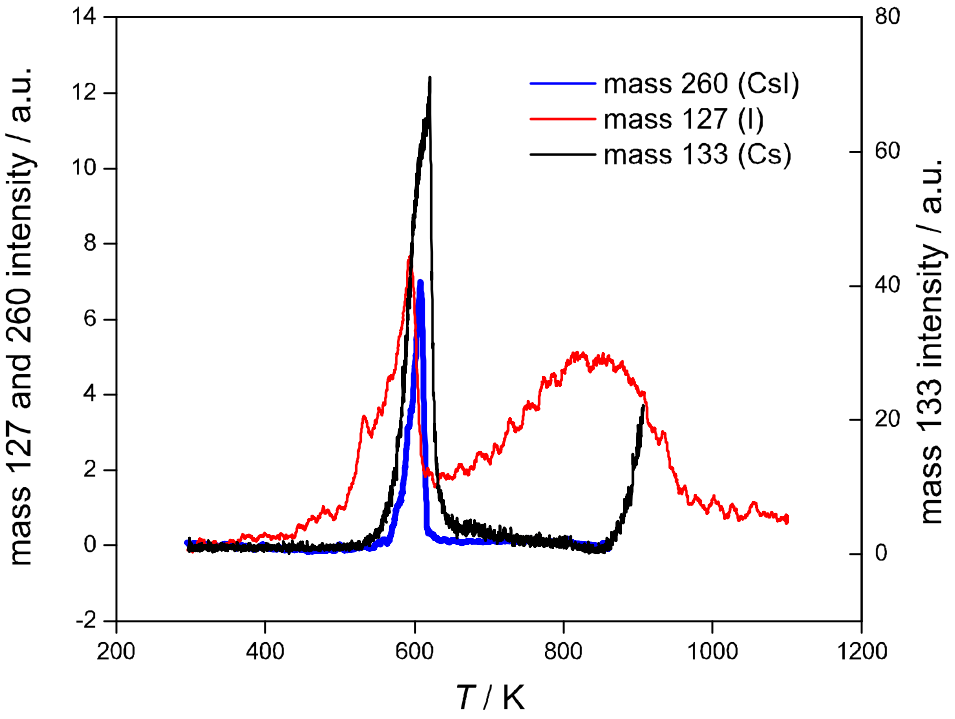

Figure 4.7: Thermal desorption spectra of mass 133 (Cs, black), 127 (I, red) and 260 (CsI, blue) from Pt(111)($\sqrt{7} \times \sqrt{7}$)R19.1°-Cs,I. The Pt(111)($\sqrt{7} \times \sqrt{7}$)R19.1°-Cs,I structure was prepared by dosing iodine on Pt(111)(*ihcp*)-Cs until no change in the work function was observed.

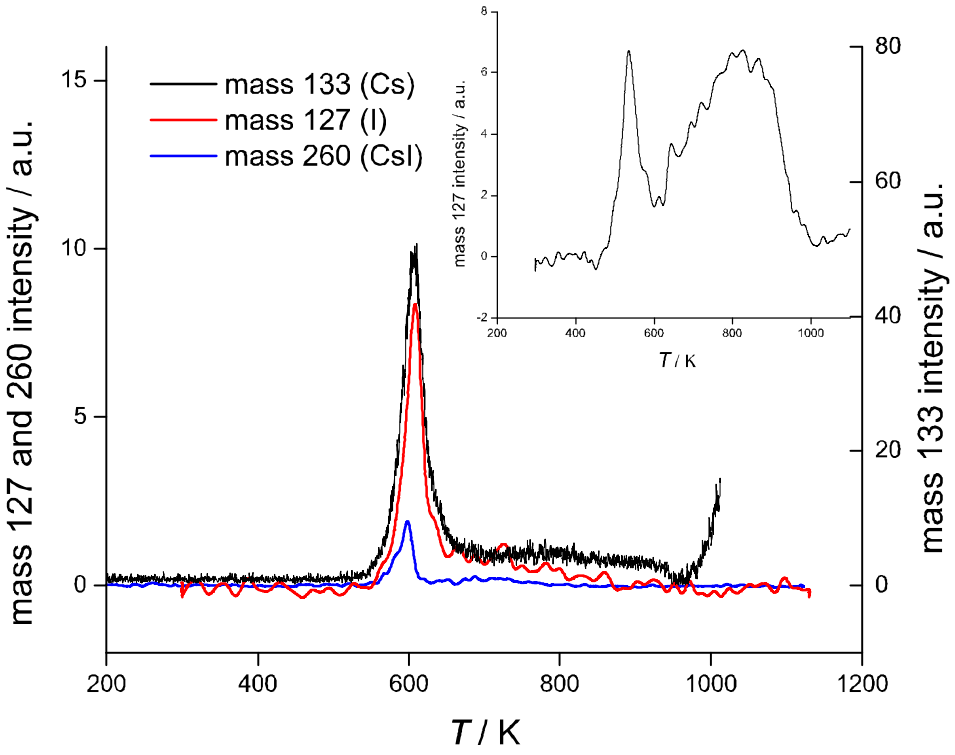

Figure 4.8: Thermal desorption spectra of mass 133 (Cs, black), 127 (I, red) and 260 (CsI, blue) from Pt(111)(4×4)-CsI. Inset shows TDS spectrum of mass 127 (I) from Pt(111)$(\sqrt{7} \times \sqrt{7})R19.1°$-I. The Pt(111)$(4 \times 4)$-CsI structure was prepared by dosing iodine on Pt(111)(*ihcp*)-Cs until the WF change was 1 eV.

from Pt(111)($\sqrt{7} \times \sqrt{7}$)R19.1°-Cs,I. There is a significant amount of Cs desorbing at temperatures higher than 600 K, as is found for desorption from surfaces covered only with Cs.

4.4.3 Oxygen adsorption on Cs+I surfaces

Oxygen adsorption/desorption was used to probe the reactivity of the Pt(111)(4 × 4)-Cs,I and Pt(111)($\sqrt{7} \times \sqrt{7}$)R19.1°-Cs,I. layers (Fig. 4.9). The various surfaces were exposed to 8×10^{-8} mbar of O_2 until no change in the work function was observed. Mass 32 (O_2) TDS from bare Pt(111) shows one peak centered around 800 K. Desorption from oxygen-dosed Pt(111)(4 × 4)-Cs,I also shows one TDS peak but with much less intensity and with the peak maximum shifted to 820 K. TDS from oxygen-dosed Pt(111)($\sqrt{7} \times \sqrt{7}$)R19.1 °-Cs,I resulted in a flat spectrum with no visible peaks. This observation correlates very well with the WF measurements: O_2 adsorption on Pt(111)(4 × 4)-Cs,I induces a WF increase of 0.15 eV, whereas adsorption on Pt(111)($\sqrt{7} \times \sqrt{7}$)R19.1 °-Cs,I gives no significant WF change.

The adsorption of oxygen on these Cs,I surfaces gives information about the compactness of the Cs,I layer. The absence of oxygen adsorption on Pt(111)($\sqrt{7} \times \sqrt{7}$)R19.1°-Cs,I suggests that that Pt(111)($\sqrt{7} \times \sqrt{7}$)R19.1°-Cs,I layer is compact. In contrast, for the Pt(111)(4 × 4)-Cs,I surface, the O_2 TDS peak at 822 K is at a similar temperature to that on the bare Pt(111) surface (795 K, Fig. 4.9 black curve), suggesting that oxygen adsorbs on Pt sites between Cs,I islands. A stronger interaction with the Cs,I surface would lead to more complex spectra, as is seen in the case of oxygen desorption from Pt(111)-K [5]. Our reference O_2 TDS from the fully covered Pt-O surface corresponds well with data from other groups for coverages $\theta_O < 0.25$ [54–56].

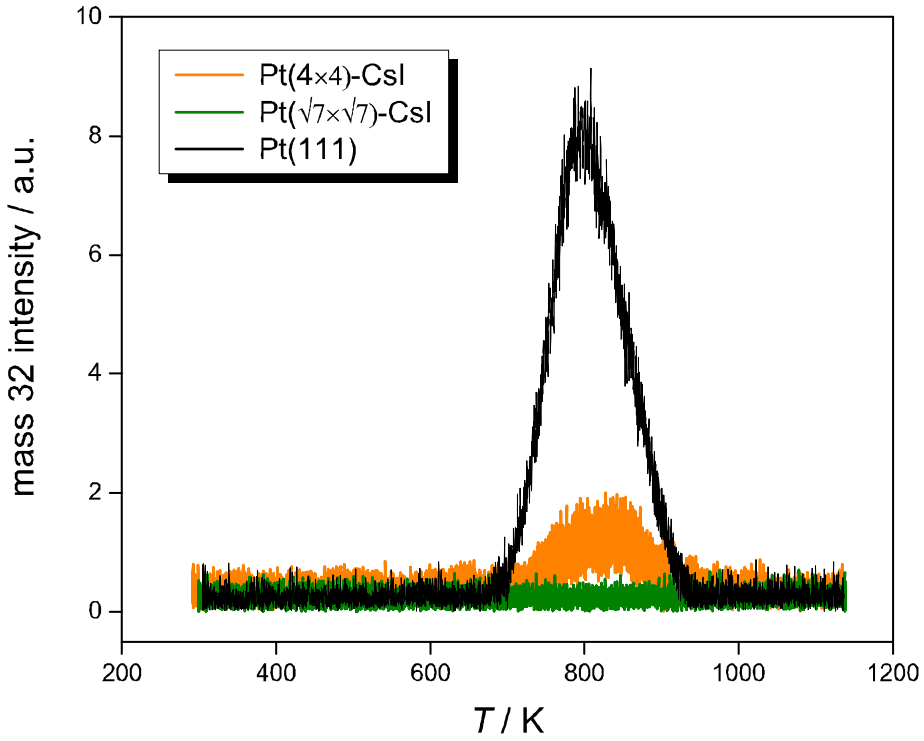

Figure 4.9: Mass 32 (O_2) TDS spectrum from clean Pt(111) (black curve), Pt(111)(4×4)-Cs,I (yellow curve) and Pt(111)($\sqrt{7} \times \sqrt{7}$)$R19.1\,^\circ$-Cs,I (green curve) surfaces exposed to 8×10^{-8} mbar of O_2 to saturation. The overall work function change during the O_2 adsorption on Pt(111)(4×4)-Cs,I and Pt(111)($\sqrt{7}\times\sqrt{7}$)$R19.1\,^\circ$-Cs,I is 0.15 eV and 0 eV respectively.

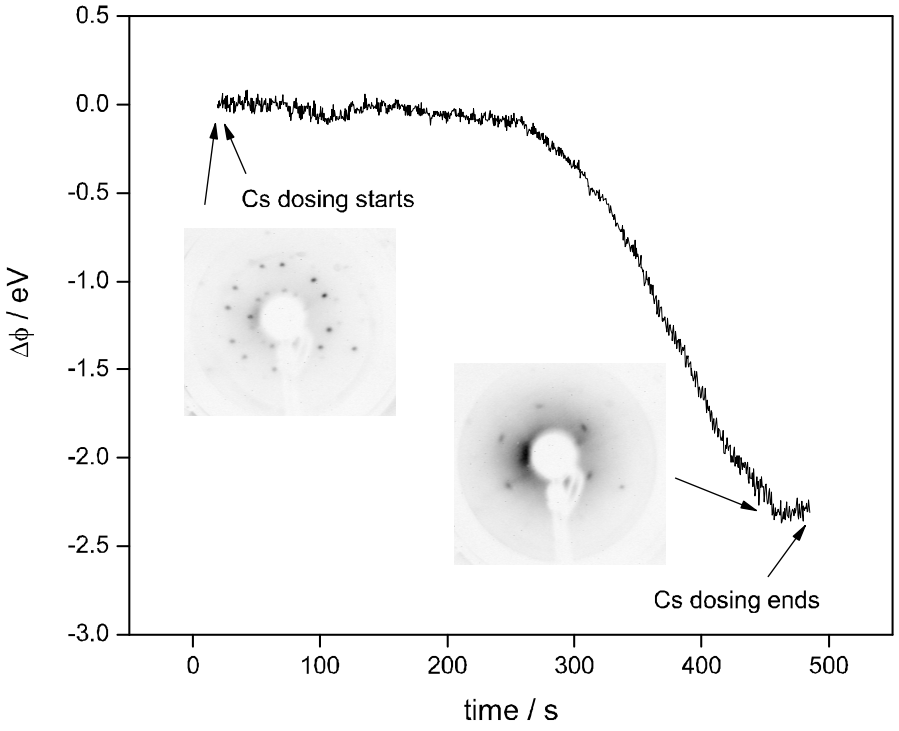

Figure 4.10: Work function change for Cs adsorption on Pt(111)$(\sqrt{7}\times\sqrt{7})R19.1°$-I at 302 K. The work function stays at its initial value for 250 s and then decreases. The overall drop of about -2.5 eV is reached at I saturation after 450 s. The initial $(\sqrt{7}\times\sqrt{7})R19.1°$ and final (*ihcp*) LEED patterns are also shown.

4.4.4 Cs adsorption on Pt$(111)(\sqrt{7}\times\sqrt{7})R19.1°$-I

When Cs is adsorbed on a Pt(111)$(\sqrt{7}\times\sqrt{7})R19.1°$-I surface, the WF response shows some unexpected behavior (Fig. 4.10). First, the WF stays at its initial value for a Pt(111)$(\sqrt{7}\times\sqrt{7})R19.1°$-I layer for about 5 min. Then abruptly the WF starts to decrease, which is consistent with the onset of electropositive Cs adsorption. Further Cs dosing causes the WF to level off at about 2.5 eV below its initial value. The initial structure has the $(\sqrt{7}\times\sqrt{7})R19.1°$ LEED pattern expected for an I saturated Pt(111)

surface [36–39]. As Cs is adsorbed, the structure changes through Pt(111)(4 × 4)-Cs,I (LEED not shown) to a Cs,I structure with the (*ihcp*) LEED pattern. The coverages in the final Pt(111)(*ihcp*)-Cs,I structure were measured with AES to be $\theta_{\mathrm{Cs}} = 0.38 \pm 0.16$ and $\theta_{\mathrm{I}} = 0.23 \pm 0.09$.

4.5 Discussion

4.5.1 Cs adsorption on Pt(111)

Cs adsorption on Pt(111) follows the general trends known from other alkali metal on transition metal adsorption systems such as significant decrease of WF, observation of multiple surface structures and broad desorption peak. [7]. Various surface characterization methods have previously been used to investigate the adsorption/desorption behavior of Cs on Pt(111) [34,35,40–42,47,63]. Cesium is known to form well ordered Pt(111)(2×2)-Cs, Pt(111)($\sqrt{3}\times\sqrt{3}$)$R30\,^{\circ}$-Cs and Pt(111)(*ihcp*)-Cs structures [40,47]. The high degree of ordering is believed to result from repulsive interactions between the partially-ionic alkali atoms [16, 17].

The measured work function curve of Cs adsorption (Fig. 4.1) is in good agreement with already published results [34, 35, 41]. The most interesting feature is the abrupt change in slope ("break") around 3 eV at a cesium coverage of 0.15±0.3 ML [62]. Such breaks are usually associated with a change in dipole moment [6]. We showed that this break is most likely due to a phase transition from an "anomalous" charged adsorption state to a neutral adsorption state [62]. In both states, Cs atoms are adsorbed on top of the surface. The alternative literature explanation for K on Pt(111) that the work of WF break involves alkali incorporation into the surface [29–32, 49] is unlikely for Cs because of the size mismatch between Cs and Pt atoms [62].

The work function increase following the minimum is qualitatively explained by Cousty at al. as depolarization of the Cs-Pt bond with increasing coverage and

subsequent formation of metallic bonds between Cs adatoms [35]. Metallic bonding is consistent with the structure of Pt(111)(*ihcp*)-Cs, which is incommensurate with the substrate, implying non-directional Cs-Pt bonding. Further clarification of this model was introduced by Rhead [14, 15]. The minimum of the work function was related to the nucleation of a dense phase with a work function close to the bulk Cs value. Thus as the Cs coverage increases after reaching the WF minimum, LEED spots from the dense phase should appear. This is indeed observed as the emergence of Pt(111)($\sqrt{3} \times \sqrt{3}$)$R30\,^{\circ}$-Cs and Pt(111)(*ihcp*)-Cs patterns (Fig. 4.2).

4.5.2 Coadsorption of Cs and I on Pt(111)

Effect of dosing order

The growth of the Cs,I layer greatly depends on the order of Cs and I dosing. If the order of dosing is Cs first and then I, the Cs,I layer starts to form almost the instant that dosing begins, as seen from the WF response (Fig. 4.3). The situation is very different if I is adsorbed first followed by Cs. The WF stays at its initial value for approximately 5 min after Cs dosing starts, and then decreases rapidly. We suggest that in the latter case, the Cs,I layer grows as islands and island nucleation is a slow process relative to the average residence time of Cs or alternatively, Cs adsorbs as a precursor on the Pt(111)-I layer. We cannot conclude if the instant WF response in I adsorption on Pt(111)(*ihcp*)-Cs is due to the fast nucleation rate or direct random incorporation of I into the Cs matrix or some other mechanism. Clearly, this interesting issue needs further clarification.

Further evidence of island formation of Cs,I on Pt(111) comes from the observation of the mixed Pt(111)($\sqrt{3}\times\sqrt{3}$)$R30\,^{\circ}$-Cs,I, Pt(111)$(3\times3)R30\,^{\circ}$-Cs,I and Pt(111)($\sqrt{7}\times\sqrt{7}$)$R19.1\,^{\circ}$-Cs,I LEED patterns (Figs. 4.5c and d); the layer is in form of islands consisting of different Cs,I structures which are on the surface simultaneously. For this dosing order, the Cs,I overlayer preferentially forms the structures determined

by the I interaction with the substrate and these structures are the same as for I adsorption on Pt(111) [36, 38].

TDS analysis

The difference in the TDS from the two ordered structures made by dosing I onto Pt(111)(*ihcp*)-Cs structures can be used to deduce some information about structure and bonding. AES calibration shows $\theta_{\mathrm{Cs}} \approx \theta_{\mathrm{I}}$ (within experimental error) for Pt(111)$(\sqrt{7} \times \sqrt{7})R19.1°$-Cs,I and $\theta_{\mathrm{Cs}} > \theta_{\mathrm{I}}$ for Pt(111)(4×4)-Cs,I. Iodine TDS spectra from Pt(111)$(\sqrt{7} \times \sqrt{7})R19.1°$-Cs,I resemble the spectra from Pt(111)$(\sqrt{7} \times \sqrt{7})R19.1°$-I with the exception of the extra sharp Cs_xI_y peak which is apparent in the mixed Cs,I layer. We conclude that the majority of I in Pt(111)$(\sqrt{7} \times \sqrt{7})R19.1°$-Cs,I layer *is not* desorbing with Cs and the amount of I directly bonded to Cs is determined by the Cs coverage. Evidently, the $(\sqrt{7} \times \sqrt{7})R19.1°$ arrangement is driven mainly by the excess of strong I-Pt interactions, which are stronger than the Cs-I or Cs-Pt interactions. When the Cs_xI_y cluster has desorbed, there is still I remaining on the surface, which desorbs as a broad high temperature peak similar to the peak observed in TDS from Pt(111)$(\sqrt{7} \times \sqrt{7})R19.1°$-I.

In contrast, the Pt(111)(4×4)-Cs,I layer has an excess of Cs and all available I atoms desorb in the Cs_xI_y cluster. No high temperature I TDS peak is observed. The excess Cs, which does not desorb from the surface in the Cs_xI_y peak, forms a high temperature Cs desorption tail that is similar in shape to that for Cs desorbing from clean Pt.

We consider now the nature of the Cs_xI_y clusters desorbing from the surface. The TDS spectra in Figs. 4.8 and 4.7 show common overlapping peaks at 600 K indicating simultaneous desorption of Cs and I. Overlap with the mass 260 (CsI) peak suggests desorption in the form of a Cs_xI_y cluster of unknown stoichiometry. The detection scheme used in the mass spectrometer allows us to distinguish desorption of neutral

and charged species from the surface [62]; all three measured TDS spectra show that the desorbing species are neutral. The same TDS Cs_xI_y peak is also observed for Pt(111)-Cs,I prepared by dosing I on the Pt(111)(*anom*)-Cs surface ($\theta_{\mathrm{I}} = 0.37 \pm 0.05$ and $\theta_{\mathrm{Cs}} = 0.10 \pm 0.04$) [62].

Ionic M_nX_{n-1} clusters have been previously found to exist and to be stable under UHV conditions [64]. Our tentative assignment is based on the TDS spectra analysis and AES determined coverages as follows. For the Pt(111)$(\sqrt{7} \times \sqrt{7})R19.1°$-Cs,I structure ($\theta_{\mathrm{Cs}} = 0.33 \pm 0.07$, $\theta_{\mathrm{I}} = 0.35 \pm 0.06$), all the Cs desorbs in the cluster peak but a significant amount of I still remains on the surface. Therefore the cluster must be rich in Cs. Subtracting the cluster peak from the spectra and integrating the remaining I signal (at both lower and higher temperatures than the cluster peak) gives $\theta_{\mathrm{I}} \approx 0.25 \pm 0.02$. Subtracting this from the initial iodine coverage of 0.35 ± 0.06, shows that the amount desorbing in the cluster is about 0.1 ± 0.06 ML, which means that the ratio of Cs to I compatible with simple stoichiometries of either Cs_2I or Cs_3I.

However, the same argument fails when comparing TDS spectra from Pt(111)$(4 \times$ 4)-Cs,I. In this layer, the majority of I desorbs in the cluster peak and the high temperature I TDS peak is missing. The AES coverage for iodine is $\theta_{\mathrm{I}} = 0.28 \pm 0.07$, therefore two or three times as much Cs should desorb from the surface in the cluster form. This is unrealistic, as the AES coverage for Cs is measured to be $\theta_{\mathrm{Cs}} = 0.35 \pm$ 0.11. It is possible that the desorbing cluster from Pt(111)(4×4)-Cs,I has a different stoichiometry compared to the cluster from Pt(111)$(\sqrt{7} \times \sqrt{7})R19.1°$-Cs,I, but it is more likely that the large systematic error in our AES coverage determination for Pt(111)(4×4)-Cs,I precludes a quantitative conclusion. Nonetheless, a Cs:I ratio as high as Cs_3I seems unlikely, and so we tentatively assign the cluster peak as Cs_2I.

The TDS cluster peak has the same shape and very similar maximum temperature for both studied surface structures. The exponential leading and very steep trailing edge is characteristic of desorption from island edges or layers with strong attractive interactions [16]. The similar desorption characteristics suggest that the

Cs-I cluster desorption pathway is not significantly different for the Pt(111)(4×4)-Cs,I, Pt(111)$(\sqrt{7} \times \sqrt{7})R19.1°$-Cs,I . The Pt(111)-Cs,I prepared by dosing I on the Pt(111)$(anom)$-Cs surface also shows the same behavior.

Cs atoms desorbing in this peak are thermally stabilized (desorbing at a higher temperature) for Pt(111)(4×4)-Cs,I and Pt(111)$(\sqrt{7} \times \sqrt{7})R19.1°$-Cs,I layers. The bonding of Cs is changed in each case when compared to Pt(111)-Cs. For both Pt(111)(4×4)-Cs,I and Pt(111)$(\sqrt{7} \times \sqrt{7})R19.1°$-Cs,I, the desorption temperature of high coverage Cs *increases* relative to Pt(111)-Cs. We conclude that the presence of iodine on the surface *increases* the Cs-substrate interaction, probably through an attractive Cs-I interaction, because the metallic Cs layer in the $(ihcp)$ structure has only limited interaction with the substrate (weak bond) [35].

In contrast, the desorption temperature of I in Pt(111)(4×4)-Cs,I *decreases* when compared to the TDS from Pt(111)$(\sqrt{7} \times \sqrt{7})R19.1°$-I (Fig. 4.8, also [45]), i.e., the Pt-I bond is weakened [65, 66].

Atomic arrangements

The LEED analysis used in our experiments gives information about only the unit cell size and orientation but not about the atom positions within the unit cell. It is clear from the TDS analysis above that there is a significant change in type of bonding relative to the systems with Cs or I alone. It is tempting to suggest that since ionic clusters desorb from all the coadsorption systems, the bonding on the surface has ionic character. However, the high mobility of adsorbates at the desorption temperature means that the species desorbing need not reflect those on the surface before the surface was heated. Nonetheless, ionic bonding in bulk and cluster alkali halides might be expected to carry over to 2-D surface structures. In this section we propose surface structures based on symmetry and observed coverages and confirm their consistency with the hypothesized ionic bonding. Only structures with hexagonal symmetry

are considered. This is consistent with the general trend in surface science, where monolayer thick binary structures tend to often be of high symmetry.

Two principles guide the proposed atom locations in ionic structures. Firstly, Wang et al. [18] proposed that for hexagonal symmetry of the overlayer, favorable unit cell configurations have stoichiometries of 1:1, 1:2 and 1:3. These layers are favoured because every ion is surrounded by a maximum number of counterions for a given coverage, therefore minimizing the electrostatic energy of the layer. Intralayer electrostatic interactions dominate over adsorbate-substrate interactions, and so the atoms are not expected to be in high symmetry sites. Secondly, if the adsorbed atoms are ions in a 2D crystal, the interatomic distances should be close to the sum of ionic radii [18]. The average sum of accepted effective ionic radii for Cs and I is $d_{\mathrm{ion}} = 3.87$ Å ($r_{\mathrm{Cs^+}} = 1.67$ Å and $r_{\mathrm{I^-}} = 2.20$ Å [67]). This value is in good agreement with the nearest neighbor spacing of 3.95 Å for CsI crystals [68]. For the Pt(111)(4×4)-Cs,I structure, we can satisfy these two principles with mixed-layer structures. For the higher coverage structures, the interatomic spacings are necessarily smaller, and closer to those expected for covalent bonds ($r_{\mathrm{cov,Cs}} = 1.67$ Å plus $r_{\mathrm{cov,I}} = 1.40$ Å equals 3.07 Å) [69]. However, even in these cases bilayer structures with a degree of ionic bonding will be considered, and are found to be reasonable on energetic and structural grounds.

Pt(111)(4×4)**-Cs,I** The first ordered Cs,I structure observed upon I adsorption on Pt(111)(*ihcp*)-Cs has a (4×4) LEED pattern (Fig. 4.4b, c). Atomic arrangements, as shown in Fig. 4.11 were considered as possible unit cell structures, and calculated coverages of Cs and I for each structure are shown in Table 4.1 The structure in Fig. 4.11a is unlikely to be the experimental one, owing to the disagreement with the experimental coverages, but is included for comparison.

The Cs_2I structure (Cs:I ratio 2:1) as shown in Fig. 4.11b, has a total high coverage of $\theta = 9/16 = 0.56$. One third of this coverage would be iodine ($\theta_{\mathrm{I}} = 3/16 = 0.19$)

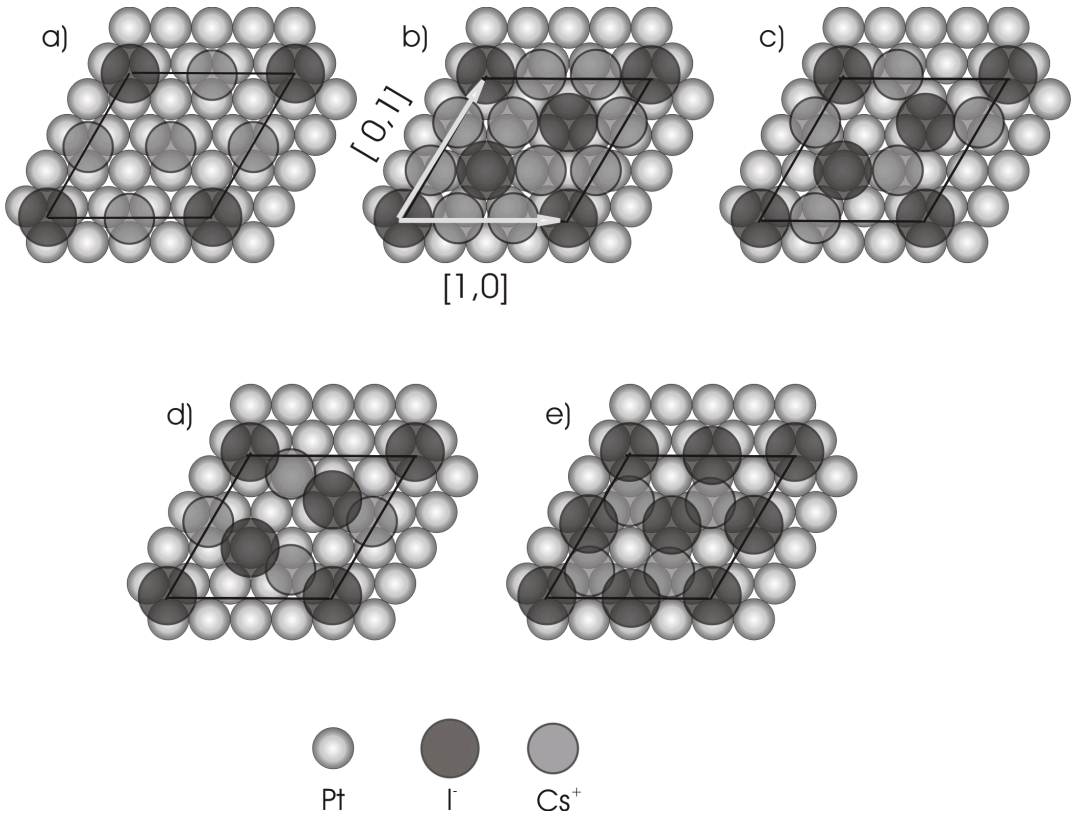

Figure 4.11: Five proposed Pt(111)(4 × 4)-CsI structures are depicted. a) shows Cs_3I structure with total coverage $\theta = 0.25$. b) shows a higher packed Cs_2I unit cell ($\theta = 0.56$). c) and d) show different configurations of the CsI layer with 6 atoms in unit cell ($\theta = 0.37$) and e) shows CsI layer with 8 atoms in unit cell ($\theta = 0.50$).

Structure	Unit cell Cs:I ratio	θ_{Cs}	θ_I	Symmetry
Cs_3I (Fig. **4.11**a)	3:1	0.19	0.06	hexagonal
Cs_2I (Fig. **4.11**b)	6:3	0.38	0.19	hexagonal
CsI (Fig. **4.11**c)	3:3	0.19	0.19	hexagonal
CsI (Fig. **4.11**e)	4:4	0.25	0.25	hexagonal
CsI	5:5	0.31	0.31	oblique
CsI	6:6	0.38	0.38	hexagonal
Experimental (AES)		0.35 ± 0.11	0.28 ± 0.07	

Table 4.1: The Cs and I coverages and symmetries of the proposed Pt(111)(4×4)-Cs,I structures.

and two-thirds cesium ($\theta_{\mathrm{Cs}} = 3/8 = 0.38$). The average Cs-I separation in the <1,0> directions assuming the planar configuration is $d_{\mathrm{av}} = 3.71$ Å, which is close to the sum of the ionic radii (3.87 Å), but much larger than the sum of covalent radii (3.07 Å).

The CsI structure (Cs:I ratio 1:1) is shown in Fig. 4.11c. Cs and I each have the same coverage of $\theta = 3/16 = 0.19$. This structure was assigned by Bravo et al. [59] to the Au(111)-CsI layer with a (4×4) LEED pattern formed during adsorption from aqueous CsI solution (pH 6.8) at potentials below -0.55 V vs Ag|AgCl. The structure assignment was based on AES coverages which were $\theta_{\mathrm{I}} = \theta_{\mathrm{Cs}} \approx 0.19$ (Fig. 5 in [59]). It should be emphasized that layers deposited in an aqueous environment may develop different structures than those formed in UHV conditions, due to the presence of the polar solvent. The average nearest neighbor Cs-I separation for this layer is the same as for Cs_2I, $d_{\mathrm{av}} = 3.71$ Å (compare Figs. 4.11b and c).

The structure depicted in Fig 4.11d is a variation of the unit cell discussed above, where the atoms of one type are shifted to the bridge bonding sites between atoms of the opposite type. In this arrangement, atoms of opposite types alternate along the $< 2, \overline{1} >$ direction. Even though there is no hexagonal symmetry, this structure is still shown, because the electrostatic energy of the unit cell is lower than the electrostatic energy of the structure in Fig. 4.11c [18].

The CsI structure in Fig. 4.11e also has a 1:1 Cs:I ratio, however, the overall coverage of $\theta = 0.50$ ($\theta_{\mathrm{Cs}} = 0.25$, $\theta_{\mathrm{I}} = 0.25$). The Cs-I separation is $d_{\mathrm{av}} = 3.21$ Å which is significantly smaller than the sum of ionic radii (3.87 Å).

AES calibration of our Pt(111)(4×4)-Cs,I layer prepared under UHV conditions results in $\theta_{\mathrm{Cs}} = 0.35 \pm 0.11$ and $\theta_{\mathrm{I}} = 0.28 \pm 0.07$. Given the large systematic error (discussed in section 4.4.2), we also expect coverages to differ significantly towards lower values of iodine and higher values of Cs. This is supported by the I coverage estimation from the WF measurements where θ_{I} is found to be between $0.16-0.19$. As a result, the experimental coverages are closest to the 2:1 stoichiometry (Fig. 4.11b).

However, possible structures with 1:1 stoichiometry need to be carefully considered due to the large experimental error.

The structure in Fig. 4.11c is unlikely, due to the Cs coverage of 0.19 which is significantly lower than $\theta_{\mathrm{Cs}} = 0.35 \pm 0.11$ and $\theta_{\mathrm{Cs}} = 0.33 \pm 0.07$ observed for Pt(111)(4×4)-Cs,I and I saturated Pt(111)$(\sqrt{7} \times \sqrt{7})R19.1$-Cs,I, respectively. The other 1:1 stoichiometric structure with total coverage of 0.50 (Fig. 4.11e) is also rejected due to the inconsistency with the observed LEED pattern (Fig. 4.4). The half-integral index LEED spots for this structure should be most intense because in the approximation that the scattering factors for Cs and I are the same, the structure diffracts as though it were a (2×2) structure. The highest coverage surface structures with 1:1 stoichiometries are not considered. The unit cell with 5 Cs atoms and 5 I atoms has no hexagonal symmetry and the layer with 6 Cs atoms and 6 I atoms in the unit cell would have the I coverage ($\theta_{\mathrm{I}} = 3/8 = 0.38$) significantly higher than the observed $\theta_{\mathrm{I}} = 0.28 \pm 0.07$.

We tentatively assign our observed Pt(111)(4×4)-Cs,I to Cs_2I. In this specific structure depicted in Fig. 4.11b, one iodine atom sits at the hcp three-fold site, one at the fcc three-fold site and one at the atop site. These sites are all known to be favorable for iodine adsorption on Pt(111) [38,39]. The assignment of Cs to adsorption sites without high symmetry is consistent with other known Cs structures and a non-directional interaction with the Pt substrate. The Pt(111)(4×4)-Cs_2I structure is consistent with planar ionic arrangement as predicted by Wang et al. [18].

Pt(111)$(\sqrt{7}\times\sqrt{7})R19.1$**-Cs,I and Pt**(111)$(ihcp)$**-Cs,I** For the denser Pt(111)$(\sqrt{7}\times\sqrt{7})R19.1$-Cs,I and Pt(111)$(ihcp)$-Cs,I layers, we find that in order to accommodate higher coverages of adsorbed adatoms, the layer has to have bilayer character, where atoms of one type lie above atoms of the opposite type. Other possible arrangements include subsurface adsorption and will be briefly discussed.

For the Pt(111)$(\sqrt{7} \times \sqrt{7})R19.1$-Cs,I structure, we observe a high Cs coverage

of $\theta_{\mathrm{Cs}} = 0.33 \pm 0.07$. This coverage is within the experimental error of Cs coverage for Pt(111)(4 × 4)-Cs,I and therefore, most of the Cs atoms do not desorb during I adsorption on Pt(111)(4 × 4)-Cs,I but only change their position in the surface structure. In this structure, atoms cannot be "squeezed" into a single layer and Cs atoms are most likely partially lifted above the I layer (but not desorbed) and/or substitutively adsorbed into the I layer. We expect I atoms to be located closer to the surface than Cs atoms. The structure has the $(\sqrt{7} \times \sqrt{7})R19.1$ LEED pattern, as for Pt(111)$(\sqrt{7} \times \sqrt{7})R19.1°$-I, suggesting that the structure is mainly determined by short range Pt-I interactions.

The same $(\sqrt{7} \times \sqrt{7})R19.1$ final LEED pattern with $\theta_{\mathrm{I}} = 0.37$ and $\theta_{\mathrm{Cs}} = 0.10$ was also observed for I adsorption on the Pt(111)(*ihcp*)-Cs surface. Because of the low Cs coverage in this case, substitutional adsorption seems to be more probable [62].

We suggest that the Pt(111)$(\sqrt{7} \times \sqrt{7})R19.1°$-Cs,I structure is related to the Pt(111)(4×4)-CsI structure (Fig. 4.12).The $(\sqrt{7} \times \sqrt{7})R19.1°$ unit cell is compressed and rotated by $R19.1°$ compared to the (4 × 4) unit cell and consists of three iodine atoms and three Cs atoms. The average bond length, d_{av}, projected onto the surface plane is 2.13 Å, which is significantly less than the sum of the Cs^+ and I^- ionic radii, $d_{\mathrm{ion}} = 3.87$ Å. The most likely arrangement, assuming the I atoms lie in one plane close to the surface, is that Cs atoms are in a second layer in order to fit into the unit cell.

Dosing Cs on Pt(111)$(\sqrt{7} \times \sqrt{7})R19.1°$-I causes a similar structural evolution as in the reverse case. First a (4 × 4) LEED pattern is observed which evolves into the (*ihcp*) LEED at Cs saturation (Fig. 4.10). This final (*ihcp*) structure is likely driven by the Cs-Pt interaction because Cs atoms are in excess, and a significant number of Cs atoms do not directly interact with I. Here the bottom layer may consist of Cs atoms and the top layer of I atoms.

Other arrangements could include one of the atomic species to be adsorbed sub-

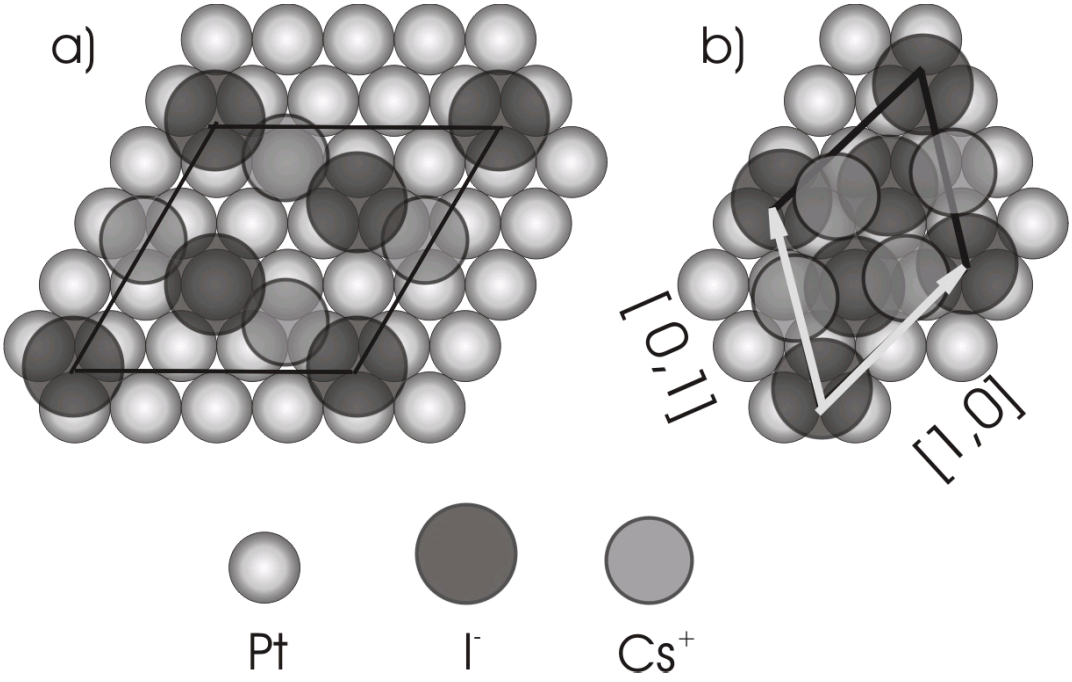

Figure 4.12: Proposed structure for Pt(111)($\sqrt{7}\times\sqrt{7}$)R19.1°-Cs,I layer (b). a) shows Pt(111)(4×4)-CsI structure for comparison.

surface, e.g., for Pt(111)($\sqrt{7}\times\sqrt{7}$)R19.1°-Cs,I the Cs atoms would be substitutionally adsorbed and I would be adsorbed on top of the surface. On clean Pt(111), it is generally accepted that cesium adsorbs on top of the surface [34,40,41,62]. In contrast, incorporation into the surface has been observed for other alkali metal/transition metal adsorption systems (for example Na on Al(111) or Au(111) [50,70]). It has been suggested that K incorporates into the surface layers of Pt(111) at low coverages [29–31]. However, Cs incorporation into the Pt lattice is unlikely for Pt(111)($\sqrt{7}\times\sqrt{7}$)R19.1-Cs,I for two reasons. Firstly, the Cs atom is significantly larger than K atom, making the incorporation less energetically favorable due to the larger lattice distortion [62]. Secondly, dislocated Pt atoms would have to diffuse on the surface to step sites to make the whole process energetically favorable. With a high coverage of I atoms on the surface, the diffusion coefficient of Pt atoms would be greatly reduced, making the incorporation of Cs unlikely.

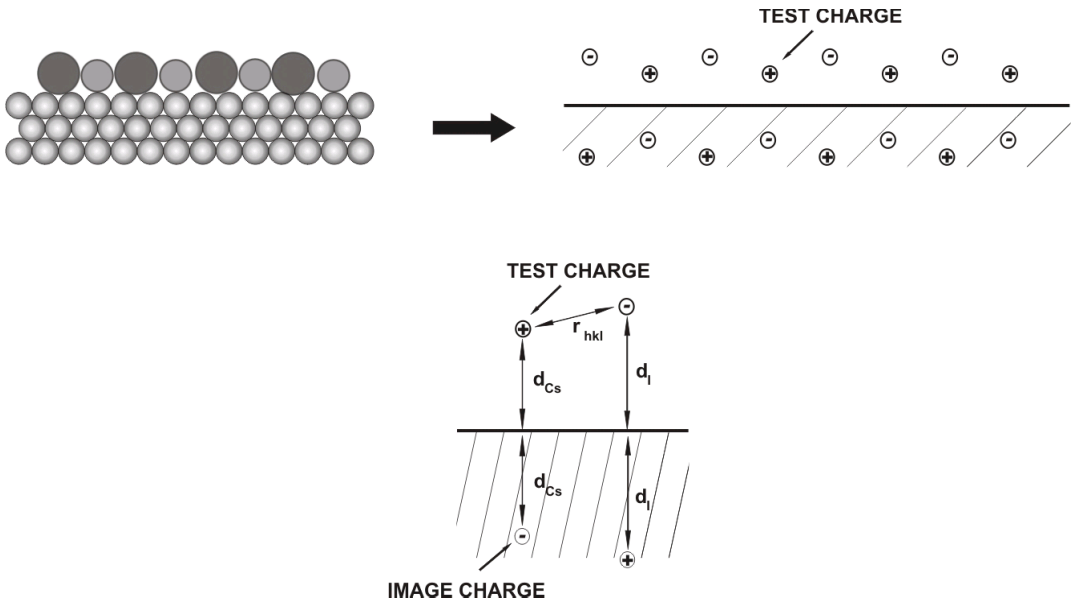

Figure 4.13: The simplified electrostatic model used in theoretical determination of electrostatic energy for different Pt(111)(4×4)-Cs,I unit cells. The adsorbed atoms are substituted by point charges and the Pt substrate is simplified by smooth metalic surface.

Electrostatic model

In order to better understand structural trends of ionic layers and to theoretically support our structural assignments, we use electrostatic energy calculations, similar to those used by Wang at al. [18]. Fig. 4.13 shows the model based on calculating the electric potential acting on test charges located at positions of adsorbed atoms in the unit cell. Adsorbed atoms are replaced by point unit charges, positive for Cs and negative for I. The substrate is approximated by a semi-infinite conductive metal surface. Each adsorbate point charge induces an image charge of opposite sign located in the metal. The electrostatic potential at the location of ith point charge within the unit cell is determined by adding contributions from all other charges (including image charges). Once the electrostatic potential from the surrounding charges is found, the

electrostatic energy, E_i, of the point charge at position i can be determined (Eq. 4.1).

$$E_i = \frac{q_i}{4\pi\varepsilon_0} \cdot \sum_{h=-\infty}^{\infty} \sum_{k=-\infty}^{\infty}{}' \sum_{l=0}^{1} \frac{q_{hkl}}{|r_{hkl}|} - \frac{q_i^2}{4\pi\varepsilon_0} \cdot \frac{1}{2d_j} \tag{4.1}$$

Here q_i is the charge in C of the ith point charge, q_{hkl} is a charge at distance r_{hkl} away from q_i, where indices h and k describe the adsorbate position on the surface with $h = 0, k = 0$ at q_i and l indexes the layers of image charges and normal charges. The distance d_j distinguishes between d_{Cs} or d_I depending on the point charge at ith position. The prime on the double sum indicates the exclusion of $h = 0, k = 0$ from the sum. The second term of the equation refers to the interaction energy with the image charge of q_i (Fig. 4.13). The electrostatic energy, for all real and image charges, is determined for all atomic positions in the unit cell. The sum of the E_i values is used to calculate the electrostatic energy of the unit cell (Eq. 4.2).

$$E = \frac{\sum_{i=1}^{N} E_i}{2 \cdot 2} \tag{4.2}$$

The i index runs over all real and image charges in the unit cell. The total energy is divided by a factor 2 to compensate for the double counting of interactions. In addition, only the electric field above the surface is real, but the calculation includes the fictitious field in the metal. To account for this, the electrostatic energy is further divided by 2.

These sums were evaluated using a program written in C^{++}. The upper bound of the summation was set to 5000 ($h = -5000$ to 5000, $k = -5000$ to 5000) which did not significantly improve the result over an upper bound of 4000. The qualitative validity of the calculations was checked by calculating the electrostatic energy difference between the structures in Fig. 4.11c and Fig. 4.11d and comparing it to the result of Wang at al. [18]. The configuration in Fig. 4.11d. was found to be favoured over the configuration in Fig. 4.11c. Our calculations for the dependence

of the electrostatic energy on the position of the Cs atoms in the 1:1 unit cell has the same shape as found by Wang at al. [18], again confirming the consistency of our model. All calculations for the 1:1 structure (CsI) refer to the configuration shown in Fig. 4.11d because it is the state with lowest energy.

Pt$(111)(4 \times 4)$**-Cs,I** Even though the calculations discussed in this and the next section are for Pt$(111)(4 \times 4)$-Cs,I and Pt$(111)(\sqrt{7} \times \sqrt{7})R19.1$-Cs,I surface structures, the overall conclusion about the dependence of electrostatic energy on the layer stoichiometry, size of unit cell, q and d is universal for all purely ionic layers.

To find the atomic arrangement with the lowest electrostatic energy, we calculated the electrostatic energies of the unit cell for each proposed Pt$(111)(4 \times 4)$-Cs,I structure (Fig. 4.11) as a function of I and Cs distances from the surface (Fig. 4.14).The charges on Cs and I atoms were always $+e$ and $-e$. For each plot, the Cs distance from the surface plane was kept constant and the I distance is varied. It is clear that the stoichiometry of the structure with the lowest energy depends on the distance of Cs atoms from the surface plane. For $d_{\mathrm{Cs}} = 1.75$ Å, the structure with the lowest electrostatic energy is Cs_2I, but as d_{Cs} increases, the CsI structure becomes energetically favorable. Unfortunately, the distance of Cs atoms from the surface in a real system cannot be determined from our experimental data. This value generally depends on the degree of ionicity of the bond, the exact electronic spatial distribution of the metal surface and the electronic overspill. An estimate of the real d_{Cs} is given by the tabulated effective ionic radius for Cs^+, which is 1.67 Å.

Calculated curves for different ionic structures reveal predicted changes in z direction separation between the planes consisting of atoms of opposite polarity. For Cs_2I , there is a well-defined minimum of the curve for $d_{\mathrm{Cs}} < d_{\mathrm{I}}$. This minimum shifts towards higher d_{I} values as d_{Cs} increases. The presence of the minimum suggests formation of a stable structure with iodine atoms located above Cs atoms. The I atoms are about 1.10 Å above the Cs atoms. If there are fewer I atoms in the

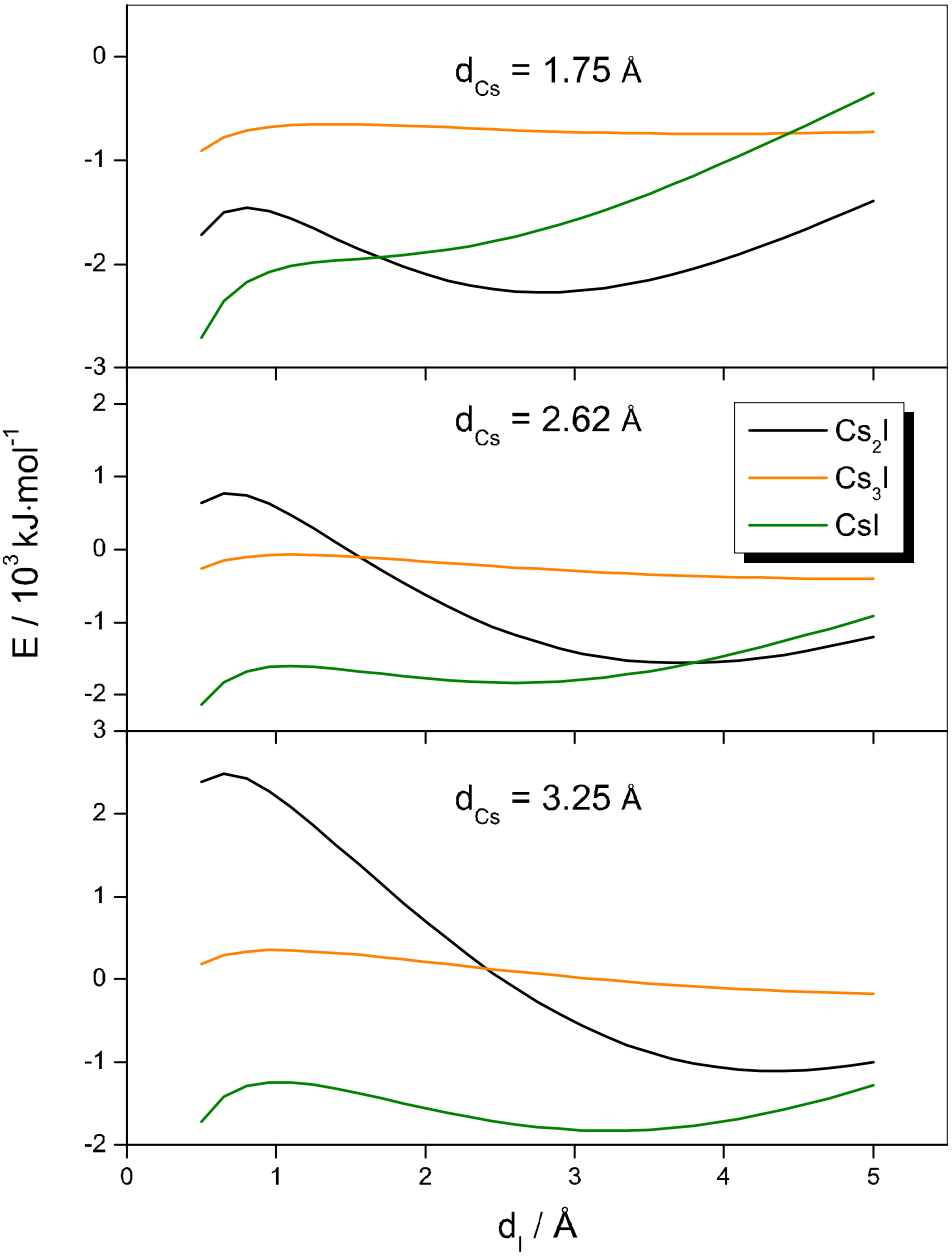

Figure 4.14: Calculated electrostatic energy for Pt(111)(4 × 4)-CsI, Cs_2I and Cs_3I for different ion distances from the metallic surface. Top plot corresponds to d_{Cs} = 1.75 Å, middle plot to d_{Cs} = 2.62 Å and bottom plot to d_{Cs} = 3.25 Å.

structure, there is a tendency for I to move even further from the surface. In the case of Cs_3I (Fig. 4.14, top plot), there is a shallow minimum at about 4 Å. For a charge-balanced CsI layer, the most favorable configuration is perfectly flat and the minimum of the curve is at $d_{Cs} = d_I$. Our calculations therefore suggest that pure ionic layers can have either planar configurations or bilayer configurations depending on the stoichiometry of the layer.

The effect of different charge states of adsorbed atoms on the electrostatic energy of the unit cell for different configurations is shown in Fig. 4.15. The Cs^+ arbitrary distance $d_{Cs} = 2.62$ Å is fixed for all three plots and charges are given in units of e. The overall electrostatic energy of the Cs_2I structure seems to be most affected by the change of the charged state of adsorbed atoms. This is not surprising because the Cs_2I structure has iodine atoms fully surrounded by cesium atoms of opposite sign. If the charge on the Cs atom is decreased, the repulsion between Cs atoms is decreased and the attraction between I and Cs atoms is also decreased. The overall electrostatic energy is slightly lowered as the decrease in repulsion counterbalances the decrease in attraction. However if the charge of the iodine atom is decreased and the charge of the cesium stays at $+e$, the repulsion between Cs atoms remains unchanged, the attraction of I to Cs is decreased which results in an overall increase in the electrostatic energy of the unit cell. I atoms are further apart compared to Cs, and therefore an increase in repulsion between I atoms affects the overall electrostatic energy to a lesser extent. The Cs_3I structure follows the same trend as the Cs_2I structure but the overall electrostatic energy change is smaller due to the larger distances between the atoms.

The CsI structure behaves differently. As the charge of iodine decreases, the energy slightly increases and the minimum becomes more prominent and moves towards higher d_I values. If the charge of Cs is decreased, the minimum becomes less pronounced and shifts towards smaller d_I. In both cases the overall energy change of the minima compared to $q_{Cs} = q_I = e$ is rather small. This is a consequence of the

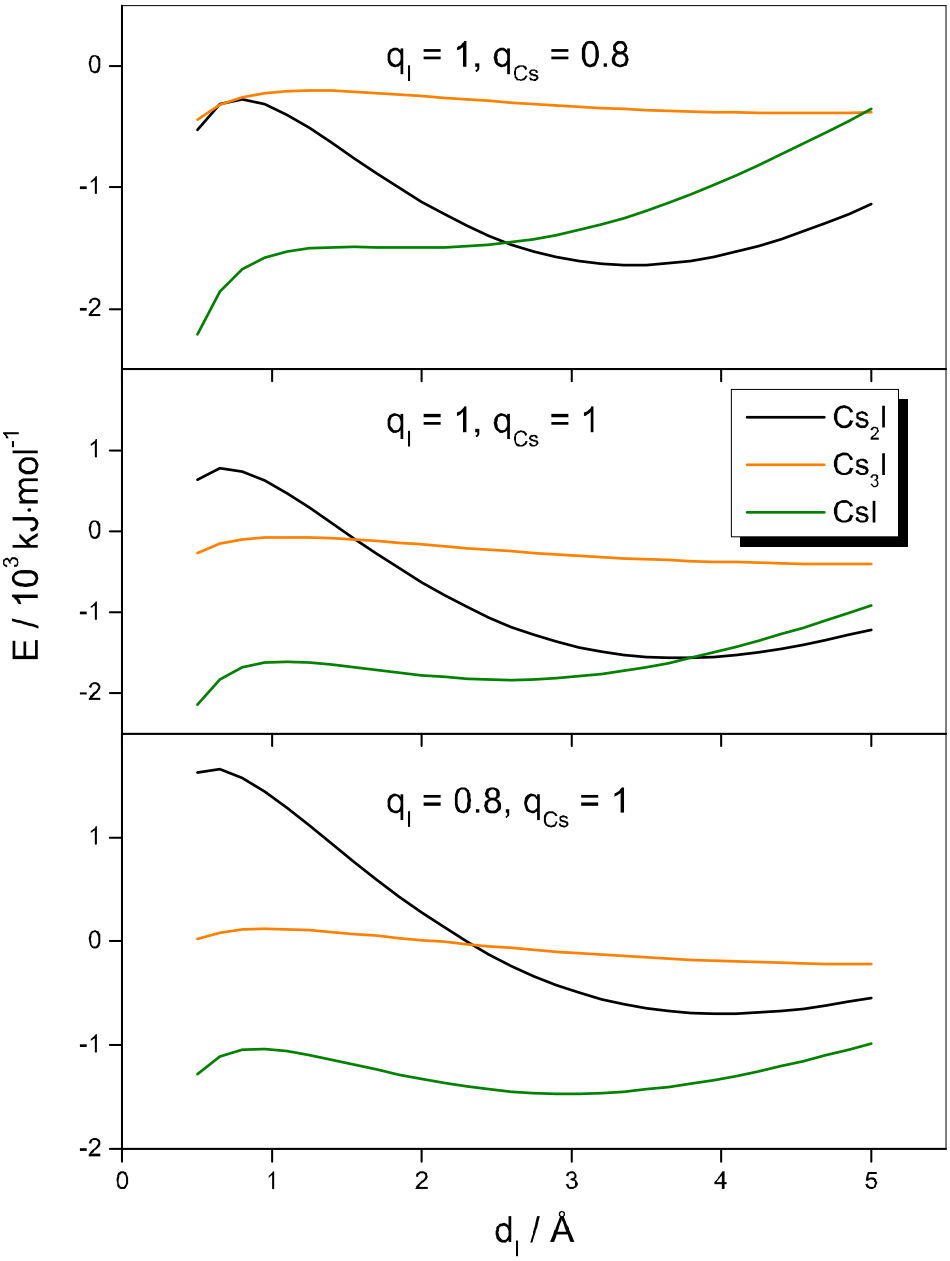

Figure 4.15: Calculated electrostatic unit cell energy for Pt(111)(4×4)-CsI, Cs_2I and Cs_3I for different ionic charges (given in units of e). Top plot corresponds to $q_I = 1$, $q_{Cs} = 0.8$, middle plot to $q_I = 1$, $q_{Cs} = 1$ and bottom plot to $q_I = 0.8$, $q_{Cs} = 1$. $d_{Cs} = 2.62$ Å for all structures.

1:1 ratio, where repulsive interactions in the layer are suppressed due to the larger distance between ions of the same polarity.

All calculated structures show characteristic shifts of the minima depending on the charge of the ions. For example, in the CsI structure the ion with higher net charge tends to be positioned closer to the surface plane than the ion of opposite (smaller) charge. Therefore we infer that in general the shift in z separation between the planes consisting of atoms of opposite polarity of the layer depends not only on the Cs:I ratio, but also on the charge situation within the layer.

Given the calculated results in Fig. 4.14, we conclude that both Cs_2I and CsI structures are equally possible from an electrostatic perspective and Cs_3I seems to be unlikely. The final determination of the most favorable structure needs further investigation of exact atomic positions. It should be also emphasized that this model is only approximate and in real situations more factors, not only electrostatic interactions, come into the play during the formation of the overlayer.

Pt$(111)(\sqrt{7}\times\sqrt{7})R19.1$**-Cs,I** To find out if the proposed structure in Fig. 4.16 is feasible, we modeled this situation with the same electrostatic model we used for the Pt$(111)(4\times4)$-CsI structure. In the case of Pt$(111)(\sqrt{7}\times\sqrt{7})R19.1°$-CsI, the electrostatic energy per unit cell decreases significantly and the minimum becomes more pronounced compared to the (4×4) unit cell (Fig. 4.16).This is a direct consequence of the compression of the unit cell, which decreases the interatomic distances and thereby increases the electrostatic attraction between atoms of opposite sign. Even though the Cs atoms on Pt$(111)(\sqrt{7}\times\sqrt{7})R19.1°$-CsI positioned above the plane of the I atoms attract their image charges more weakly and the I-I and Cs-Cs repulsions are increased, this is more than offset by the increased attraction between the Cs and I atoms. This is depicted in Fig. 4.16, where the energy for Pt$(111)(\sqrt{7}\times\sqrt{7})R19.1°$-CsI is seen to be still negative even for $d_{\mathrm{Cs}} = 4$ Å. Even though ionic layers were hypothesized to be planar by Wang et al. [18], our observations and calculations show

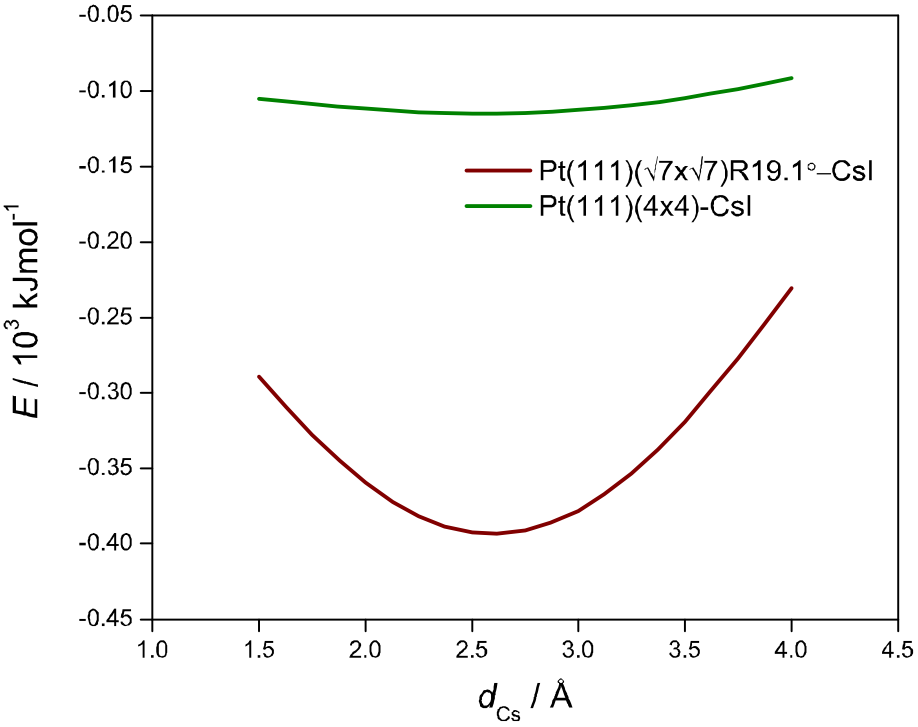

Figure 4.16: Electrostatic energy of Pt(111)$(\sqrt{7}\times\sqrt{7})R19.1°$-CsI and Pt(111)$(4\times4)$-CsI structures in kJ mol^{-1} for the area of a (1×1) substrate unit cell. $d_{\mathrm{I}} = 2.60$ Å.

that both planar and bilayer structures are consistent with ionic principles.

4.6 Conclusions

Cs and I coadsorbed on Pt(111) form different structures, depending on the amount of I and Cs adsorbed, and on the order of Cs and I dosing. Pt(111)(4×4)-Cs,I and Pt(111)$(\sqrt{7} \times \sqrt{7})R19.1$-Cs,I structures are formed if the Cs is dosed first and then I. In reverse dosing order, Pt(111)(4×4)-Cs,I forms first followed by Pt(111)(*ihcp*)-Cs,I.

The Pt(111)(4×4)-Cs,I structure is assigned to a Cs_2I 2D crystal with p6m symmetry and the Pt(111)$(\sqrt{7} \times \sqrt{7})R19.1°$-Cs,I structure is assigned to a bilayer structure with I atoms in a plane closest to the surface, and Cs atoms in a plane above the I layer. The Pt(111)(*ihcp*)-Cs,I structure is similar to that of Pt(111)$(\sqrt{7} \times \sqrt{7})R19.1°$-Cs,I, but with the Cs atoms located closer to the substrate plane than the I atoms. Electrostatic calculations show that these structures are consistent with ionic structures. However, in these structures the proposed I atoms are in the same sites as for the covalent Pt(111)$(\sqrt{7} \times \sqrt{7})R19.1°$-I structure, and therefore ionic interactions between Cs and I can coexist with partially covalent Pt-I interactions. Furthermore, ionic consideration alone are compatible with both mixed monolayers and bilayers, so that the statement that mixed layers are ionic and bilayers are covalent is too simplistic. Therefore, there is not an easy way to deduce the bonding type from structural observations alone.

4.7 Acknowledgments

The authors thank the Natural Sciences and Engineering Research Council of Canada (NSERC) and the University of Victoria for funding.

Chapter 5

Oxygen adsorption on cesium precovered Pt(111) surfaces

5.1 Abstract

The adsorption behavior of oxygen and iodine on a Cs precovered Pt(111) surface is reported. The O adsorption on Pt(111)(*ihcp*)-Cs at 295 K causes an initial work function decrease characteristic for underneath adsorption followed by a sharp increase. In contrast, iodine adsorption on Pt(111)(*ihcp*)-Cs shows only a slight initial decrease dependent on the quality of the crystal. When O is adsorbed on the Pt(111)(2×2)-Cs surface at 295 K, no initial decrease is observed and the work function only increases.

The TDS spectra from Pt(111)-Cs,O layers show complicated desorption kinetics linked to multiple adsorption states. Overlapping mass 133 (Cs) and mass 32 (O_2) TDS peaks at 820 K are assigned to tightly bonded Cs-O. We ascribe the mass 32 (O_2) TDS peak with a maximum at 673 K to adsorbed O in Cs,O islands, loosely bonded to Cs. A third oxygen species is adsorbed between Cs,O islands giving raise to a mass 32 (O_2) TDS peak at 620 K. This oxygen is in direct interaction with the Pt substrate and its bonding is indirectly affected by the coadsorbed Cs. Dosing I on

Pt(111)-Cs,O results in a substitution of O by I in Cs,O islands. The dislocated O either diffuses between Cs,I islands or leaves the surface.

When heated, the Pt(111)-Cs,O surface prepared from Pt(111)(*ihcp*)-Cs undergoes various surface transitions. Desorption of oxygen corresponding to the TDS peak at 650 K induces the surface transition to Pt(111)(4×4)-CsO_2. Further heating to 750 K causes desorption of loosely bound O and the surface structure changes again to Pt(111)(4×4)-CsO. The observed structural changes depend on the initial Cs coverage at/in the layer.

5.2 Introduction

Adsorption of small molecules on alkali-metal modified transition metal surfaces has been extensively studied in the past due to importance in heterogenous catalysis and cathode design [7]. Various techniques have been used to investigate the adsorption of O [5,63,71–73], CO [47,74,75], CH_4 [76] and cyclic hydrocarbons [42] on Pt(111)-alkali metal surfaces.

In this study, we extend this list to the adsorption of O_2 molecules on the Pt(111)-Cs surface. Although a fair amount of research has been done to understand the importance of the presence of electropositive species in relation to oxygen adsorption, the atomic arrangement and the bonding characteristics are not well understood.

The Cs,O layer can be viewed as being ionic due to the expected significant electron transfer from Cs atoms to O atoms. According to Wang et al. [18] only a few hexagonal arrangements are favorable for planar ionic layers on (111) surfaces. In our previous work, we studied the structure of Pt(111)-Cs,I and found a good correlation between Wang's proposed hexagonal layers and our observed LEED patterns [77]. In the present study, we find that another electropositive-electronegative coadsorption system (Pt(111)-Cs,O) forms the same (4×4) structure as the Pt(111)-Cs,I layer,

which further highlights the universality of Wang's approach towards the structural arrangements of 2D ionic crystals.

We show that oxygen initially adsorbs below the Cs layer, which is in contrast to the incorporation of I which is coplanar. The Cs precovered Pt(111) significantly increases oxygen uptake on the surface, similar to the case of Pt(111)-K [5]. Our TDS results show that multiple oxygen adsorption states exist on the Pt(111)-Cs,O surface. We ascribe these adsorbed species to tightly bound O in direct interaction with coadsorbed Cs and loosely bound O. The strong Cs-I bond induced by I adsorption on the Pt(111)-Cs,O causes oxygen in the Cs,O layer to desorb or to move in between Cs,I islands.

5.3 Experimental

Experiments were performed in a stainless steel UHV chamber equipped with Low Energy Electron Diffraction (LEED) optics (used also for Auger Electron Spectroscopy (AES)) and a Kelvin probe for work function measurements. A quadrupole mass spectrometer with a custom lock-in detection scheme was used for Thermal Desorption Spectroscopy (TDS). The detailed experimental setup description can be found in [62].

Two separate crystals, 1 cm in dia., were used in this study. The first crystal was cut from a boule grown by Metal Oxides and Crystals Ltd and the second crystal was obtained as a roughly oriented (111) disc from the same supplier. The preparation procedure for both crystals was the same. The surfaces were polished with diamond paste (Buehler Ltd.) and then oriented by back-Laue diffraction to a (111) plane within 0.5 °. Aluminium oxide slurry (0.05 μm) was used for the final polishing step. The first crystal was replaced in the course of this study due to the deteriorated quality of the surface. All reported experimental results are from the second crystal.

Before each set of experiments, the crystal was cleaned by Ar^+ bombardment followed by annealing to 1150 K. The quality of the crystal surface was also periodically confirmed by annealing in oxygen atmosphere followed by an AES check. This procedure was used to ensure that no contaminants were present and the details can be found in [62].

The reactivity of the crystal surface can be affected by the presence of impurities such as silicon [26]. Therefore, the crystal was periodically annealed for 1 h at 1150 K in a 5×10^{-7} mbar oxygen atmosphere in order to allow possible contaminants to segregate on the surface and form stable oxides, which were subsequently removed by Ar^+ bombardment.

The Cs was dosed on the Pt crystal using a cesium dispenser (SAES Getters, Cs/NF/2.2/12 FT10+10) located 10 cm from the surface. The cleanliness of the sample during dosing was verified by work function (WF) measurement. If the change to WF minimum was more than 4 eV, the Cs layer was considered clean. A custom built doser, based on a solid-state Ag_4RbI_5 electrochemical cell, was used to dose iodine on the surface [27]. Oxygen was dosed by exposing the crystal to 1×10^{-7} mbar of O_2.

The coverages for various surfaces were obtained with AES. The peaks corresponding to the different atomic species were normalized relative to the Pt peak at 237 eV. These normalized peaks were then compared to reference structures with known coverages. For Cs the reference structure was Pt(111)(*ihcp*)-Cs (incommensurate hexagonal close packed, $\theta_{\mathrm{Cs}} = 0.41$ ML), for I the reference structure was Pt(111)$(\sqrt{7} \times \sqrt{7})R19.1°$-I ($\theta_{\mathrm{I}} = 0.43$ ML) [36–39] and for O, the reference structure was Pt(111)(2×2)-O ($\theta_{\mathrm{O}} = 0.25$) [56, 57]. The reference structures were prepared by dosing at ambient temperature (295 ± 2 K) until no WF change was observed.

Temperatures for Cs, I and O dosing varied from 290 K to 300 K, but were kept constant during dosing. We observed no temperature-dependent variations in the

work function or other data over this range.

5.4 Results

5.4.1 Work function change during the adsorption of oxygen and iodine

Similar to other alkali metal/transition metal adsorption systems, adsorption of Cs on Pt(111) at 295 ± 2 K follows the usual work function response trend [6]. The WF initially decreases by about 5 eV (Fig. 5.1). After reaching a minimum, corresponding to the Pt(111)(2 × 2)-Cs structure ($\theta_{Cs} = 0.25$) [40, 47, 62, 77], the WF starts to increase towards the value of Cs saturated surface. During the WF increase, the surface undergoes several phase transitions [40, 47, 62, 77]. The Pt(111)(2 × 2)-Cs changes to Pt(111)($\sqrt{3} \times \sqrt{3}$)-Cs ($\theta_{Cs} = 0.33$), which further evolves to Cs saturated Pt(111)(*ihcp*)-Cs ($\theta_{Cs} = 0.41$) . The break in slope of the WF ("kink") occurring between about -1.8 to -3 eV during the initial WF decrease has been previously assigned to the phase transition from the anomalous (Cs^+) to the normal (neutral Cs) adsorption state [29, 62].

To better understand the properties of a Pt(111)-Cs layer towards iodine and oxygen adsorption, we performed various experiments where the WF was monitored. The first step in each experiment was the preparation of a Pt(111)-Cs layer at a constant temperature between 290 K and 300 K (±2 K). We chose three well-defined Cs structures to be further studied for their adsorption properties. These structures were Pt(111)(*anom*)-Cs ($\theta_{Cs} = 0.12$, WF kink), Pt(111)(2 × 2)-Cs (WF minimum) and Pt(111)(*ihcp*)-Cs (Cs saturated structure). Once these structures were prepared, I_2 or O_2 was dosed and the WF monitored (Figs. 5.1 and 5.2). Both electronegative species cause the WF to increase upon adsorption, independently of the initial Cs coverage. This is not surprising as introducing an adsorbate of opposite charge to the

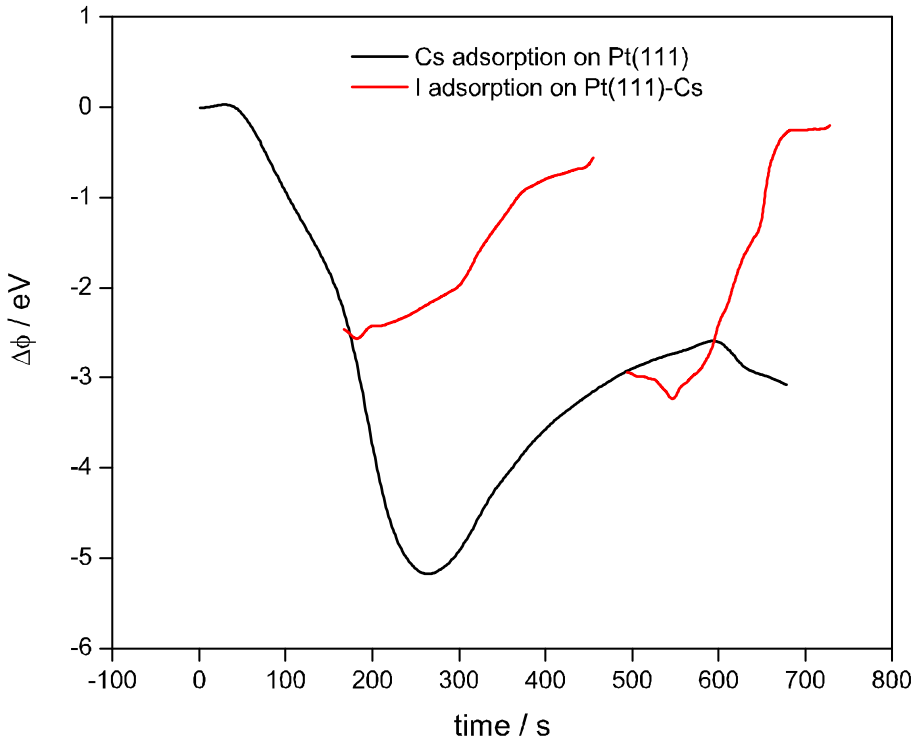

Figure 5.1: The black curve shows the WF response upon Cs dosing. The red curves correspond to the WF response to I_2 adsorption on a Cs-precovered Pt(111) surface. The initial structures are Pt(111)(*ihcp*)-Cs ($\theta_{Cs} = 0.41$) and Pt(111)(*anom*)-Cs ($\theta_{Cs} = 0.15$) respectively. During dosing the Pt crystal was held at a constant temperature between 290 and 300 K.

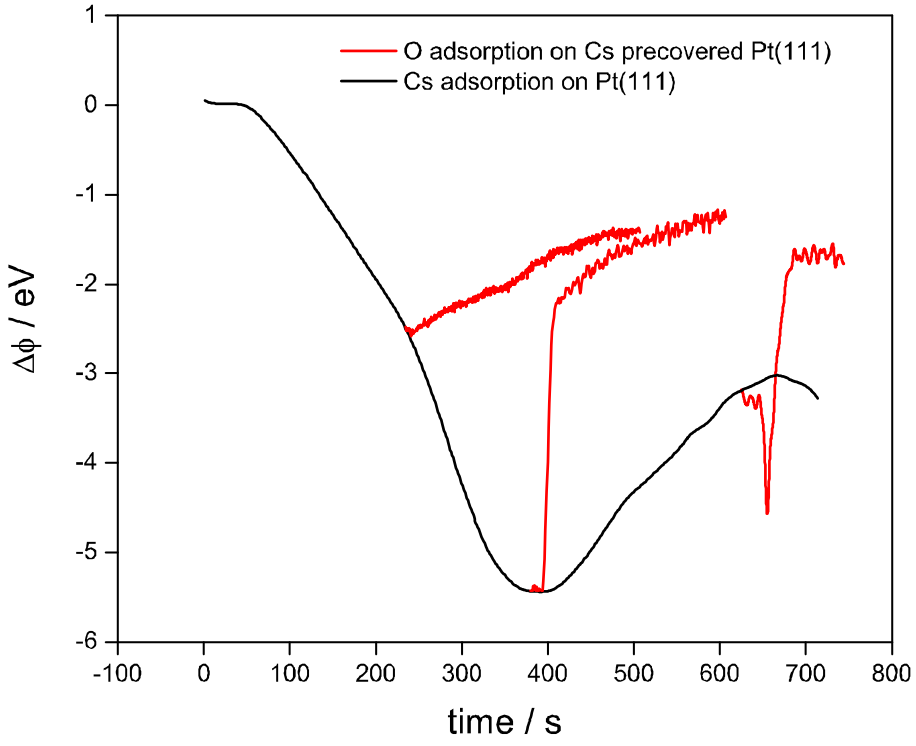

Figure 5.2: The black curve shows the WF response upon Cs dosing. The red curves correspond to the WF response of O_2 adsorption on a Cs-precovered Pt(111) surface. The initial structures are Pt(111)(*ihcp*)-Cs ($\theta_{Cs} = 0.41$), Pt(111)(2×2)-Cs ($\theta_{Cs} = 0.25$) and Pt(111)(*anom*)-Cs ($\theta_{Cs} = 0.15$) respectively. During dosing the Pt crystal was held at a constant temperature between 290 and 300 K.

$Cs^{\delta+}$ is expected to increase the WF. However, the value of the overall increase and the shape of the WF response differs between iodine and oxygen.

I_2 adsorption on a Pt(111)(*ihcp*)-Cs surface shows a slight initial WF decrease followed by a WF increase of about $2.5-3$ eV (Fig. 5.1). In our previous experiments [77], we also observed the work function increase of 2.5 eV for the same experiment, but the slight decrease at the beginning of the dosing was not evident. This is most likely due to the improved quality of the (111) surface (as checked by LEED) when compared to the surface used in previous experiments. I_2 adsorption on Pt(111)(*anom*)-Cs also exhibited an overall increase in WF. In this case, the initial shallow minimum was absent and the increase was smaller, about 1.5 eV. Independently of the initial Cs coverage, the final value of the work function of the I saturated Pt(111)-Cs,I surface approaches the work function of the Pt(111)$(\sqrt{7}\times\sqrt{7})R19.1°$-I and the layer has $(\sqrt{7}\times\sqrt{7})R19.1°$ LEED pattern [33, 77, 78]. We will refer to those surfaces as Pt(111)$(\sqrt{7}\times\sqrt{7})R19.1°$-Cs,I.

Fig. 5.2 shows the WF response to O_2 dosing on various Pt(111)-Cs surfaces. Oxygen adsorption on Pt(111)(*ihcp*)-Cs causes an initial sharp WF decrease followed by an increase of about 2.5 eV to the saturated value. However, this initial decrease disappears if the dosing temperature is changed to 150 K (result not shown), indicating a thermally-activated process. The coverages for the oxygen saturated surface are $\theta_{Cs} = 0.32 \pm 0.10$ and $\theta_O = 1.03 \pm 0.24$, as determined by AES. The Cs:O ratio is 1:3.2 which is close to the 1:3 ratio found by Ayyoob at al. for the saturated Pt(*poly*)-Cs,O surface [72]. When O_2 is dosed on Pt(111)(2×2)-Cs, the WF shows only an increasing trend until saturation. The overall increase is $3-3.5$ eV and the coverages at saturation are $\theta_{Cs} = 0.19 \pm 0.05$ and $\theta_O = 0.86 \pm 0.24$ (from AES). Similarly, O_2 adsorption on Pt(111)(*anom*)-Cs causes the WF to increase about 1 eV without any initial decrease. Estimated coverages for this structure at saturation are $\theta_{Cs} = 0.15$ and $\theta_O = 0.57$, as determined by TDS [62]. The final WF value after O_2 dosing for all three Cs precovered surfaces is similar: approx. $1.5-2$ eV lower than the WF of

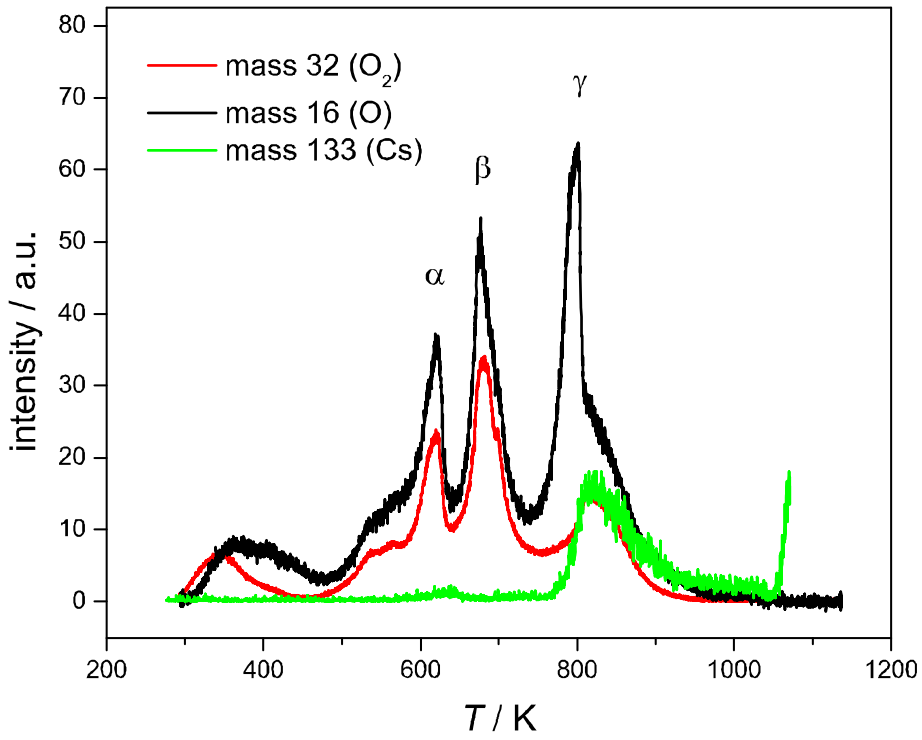

Figure 5.3: TDS spectra for various masses from a Pt(111)-Cs,O surface prepared from Pt(111)(*ihcp*)-Cs. Black curve - mass 16 (O), red curve - mass 32 (O_2) and green curve - mass 133 (Cs). The heating rate is 5 $K\,s^{-1}$.

a clean Pt(111) surface.

5.4.2 Desorption from Pt(111)-Cs,O

Oxygen saturated Pt(111)-Cs,O layers

Desorption spectra for various masses from the Pt(111)-Cs,O layer prepared by dosing O_2 on Pt(111)(*ihcp*)-Cs until saturation are depicted in Fig. 5.3. The presence of multiple peaks implies numerous kinetic processes during the desorption. The

low temperature peak around 350 K for O (mass 16) and O_2 (mass 32) spectra has been previously suggested to be due to the desorption of molecularly adsorbed oxygen [5]. This peak will not be further discussed. It should be noted that there is no O_2 molecular adsorption on the unmodified Pt(111) surface at temperatures above 150 K [79–82].

Sharp peaks at 620 K (α) and 673 K (β) appear to be of zeroth order and will be discussed later in the report. The O_2 peak at 820 K (γ) coincides with the Cs desorption peak and Cs and O_2 simultaneously desorb at this temperature with an apparent desorption energy of 215 $\mathrm{kJ\,mol^{-1}}$(Redhead analysis, $k_0 = 10^{13}$ $\mathrm{s^{-1}}$). The γ peak in the O TDS spectrum also differs from the same peak in the O_2 spectrum. The O:O_2 peak height ratios for the α and β peaks are very similar: 1.6 and 1.5. In contrast, the same ratio for the γ peak is 4.2. In other words, the γ peak in the O TDS spectrum is relatively higher than the α and β peaks when compared to the O_2 TDS. More in-depth analysis is provided in the discussion section.

There is no evidence for Cs_xO_y cluster desorption in the γ peak. Even though the γ peak for Cs and O_2 overlaps, no desorption of CsO (mass 149), CsO_2 (mass 165) or Cs_2O (mass 282) was measured.

The effect of various initial Cs coverages on oxygen adsorption is plotted in Fig. 5.4. The O_2 (mass 32) TDS spectrum (red) shows the desorption from a Pt(111)-Cs,O layer prepared by exposing Pt(111)(2×2)-Cs to O_2 until saturation at 295 ± 2 K. The black spectrum corresponds to O (mass 16) desorption and the green spectrum corresponds to the Cs (mass 133) desorption from the same surface. There are interesting differences between these spectra and the spectra in Fig. 5.3 from the Cs saturated surface. Comparison indicates that the number of adsorbed oxygen atoms is increased with increasing Cs coverage. This is consistent with AES measurement (section 5.4.1). First, there is extra O_2 desorbing as a low temperature feature between $300 - 600$ K for the layer prepared from Pt(111)(*ihcp*)-Cs. Second, there is a fine structure of peak β (673 K) on the high temperature side which is not evident

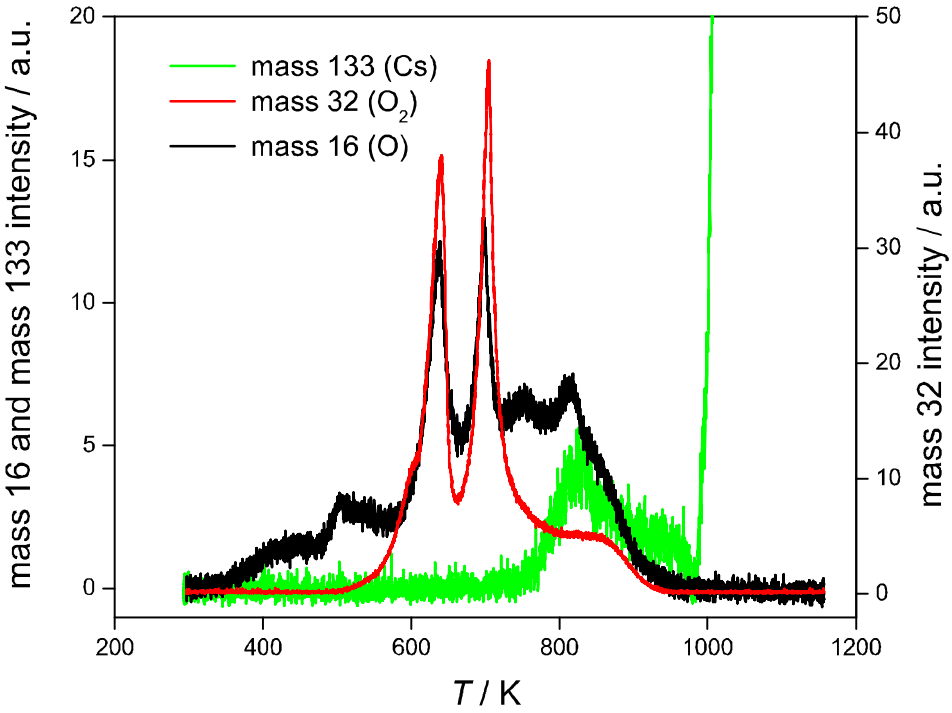

Figure 5.4: Mass 32 (O_2, red), mass 16 (O, black) and mass 133 (Cs, green) TDS spectra from a Pt(111)-Cs,O surface prepared from Pt(111)(2 × 2)-Cs by O_2 dosing to saturation. The heating rate is 5 $\mathrm{K\,s^{-1}}$.

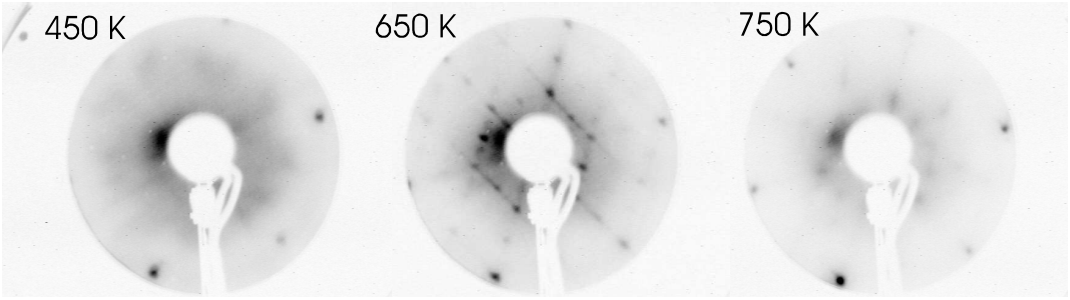

Figure 5.5: LEED patterns of a Pt(111)-Cs,O surface prepared from Pt(111)(*ihcp*)-Cs after heating to various temperatures (450 K, 650 K and 750 K). The LEED patterns were taken at 100 K with a 10 nA beam current.

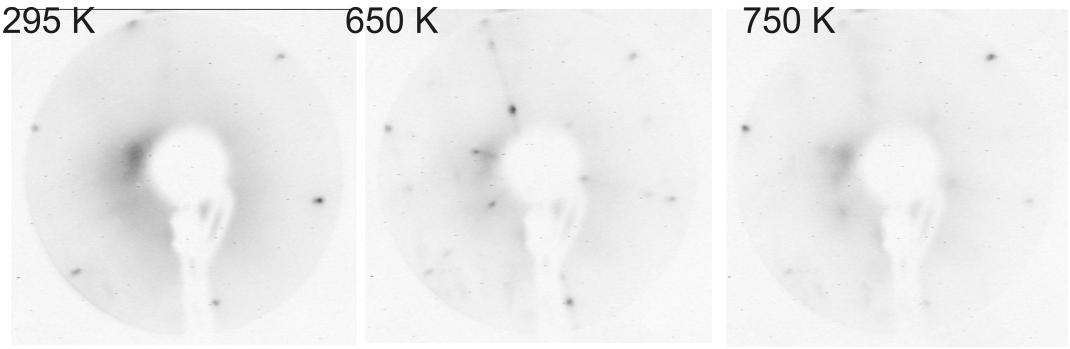

Figure 5.6: LEED patterns of a Pt(111)-Cs,O surface prepared from Pt(111)(2 × 2)-Cs after heating to various temperatures (450 K, 650 K and 750 K). The LEED petterns were taken at 100 K with a 10 nA beam current.

for the layer prepared from Pt(111)(2 × 2)-Cs. Lastly, the γ peak at 820 K, coincident with Cs desorption, retains its position for both layers, but is higher in intensity for the layer prepared from Pt(111)(*ihcp*)-Cs. The γ peak height difference is most pronounced in the O TDS spectrum.

The LEED diffraction patterns observed during the desorption experiments from the Pt(111)-Cs,O surfaces are shown in Figs. 5.5 and 5.6. The surfaces were heated to various temperatures between the sharp TDS peaks, and then cooled down, before LEED measurements at 100 K.

In Fig. 5.5, the Pt(111)-Cs,O surface was prepared by exposing Pt(111)(*ihcp*)-Cs

to O_2 until saturation at 295 ± 2 K. Heating the sample to 450 K resulted in a diffuse LEED pattern (Fig. 5.5 at 450 K) suggesting that no long-range order is present. Further heating to 650 K (between the α and β peaks of the O_2 TDS spectrum, Fig. 5.3) leads to the formation of a sharp (4×4) LEED pattern (Fig. 5.5, 650 K). Finally, heating to 750 K (between the β and γ peaks of the O_2 TDS spectrum) results in a (4×4) LEED (not very sharp), resembling the LEED from a Pt(111)(4×4)-Cs_2I layer [77].

Fig. 5.6 shows the diffraction patterns from surfaces prepared by dosing O_2 until saturation at 295 ± 2 K on a Pt(111)(2×2)-Cs surface. The first pattern shows the surface after O_2 dosing (295 K). After annealing the sample to 650 K, a (6×6) LEED pattern appears. Further annealing of this structure to 750 K results in the formation of a weak (2×2) pattern with a diffuse background.

Initial stages of Pt(111)-Cs,O layer formation

TDS spectra obtained from the pre-saturation of oxygen adsorption on a Cs saturated Pt(111) surface are shown in Fig. 5.7.

The starting structure in both cases was Pt(111)(*ihcp*)-Cs ($\theta_{Cs} = 0.41$) prepared at 295 ± 2 K. O_2 was dosed at 295 ± 2 K, until the WF passed the minimum and increased again to the starting value (Fig. 5.7 a.) and then until the overall work function change was between $0.5 - 1$ eV from the starting value (Fig. 5.7 b.). The exposures were 1.3×10^{-4} Pa s (1.3×10^{-4} Pa s = 1 Langmuir) and 3.3×10^{-4} Pa s respectively. Initially, O_2 dissociates on the surface and most of the oxygen desorbs in the atomic form as a sharp peak at 785 K (Fig. 5.7 a. black curve). Cs (mass 133, green curve) desorbs at higher temperatures with a peak maximum at 833 K (green curve). There is also a small amount of O_2 leaving the surface in the broad peak at 870 K (red curve). The O spectrum does not follow the O_2 peak at 870 K in Fig. 5.7 b. for two reasons: (i) the sensitivity of the instrument must be lowered for

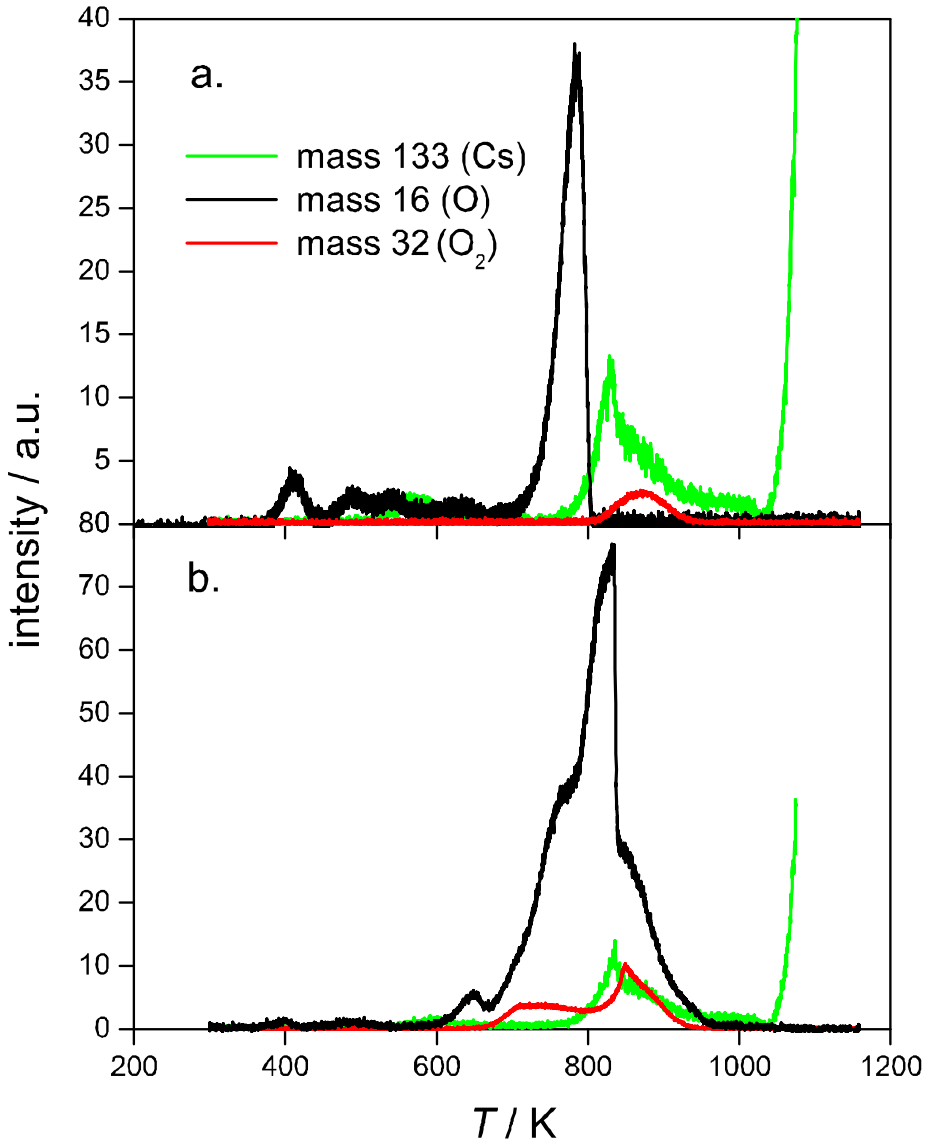

Figure 5.7: First set of TDS spectra from initial stages of Pt(111)-Cs,O layer formation. The layers were prepared by dosing O_2 on the Pt(111)(*ihcp*)-Cs surface at 295 ± 2 K. O_2 exposures: (a) 1.3×10^{-4} Pa s and (b) 3.3×10^{-4} Pa s.

mass 16 in order to measure the full height of the sharp desorption peak at 785 K, and (ii), the initial structures might not have been identical because in order to take three different spectra, new surface structures were prepared each time.

Spectra in Fig. 5.7 b. are for a higher exposure of O_2. The Cs peak retains its position and intensity compared to Fig. 5.7 a. Both O (mass 16) and O_2 (mass 32) spectra now show two desorption peaks. The peak above 800 K in the O_2 spectrum most likely develops from the small peak originally at 870 K, and overlaps with the Cs peak. This peak is for the same process as the γ peak in Fig. 5.3. The second peak at 730 K in the O_2 spectrum is the onset of the β peak formation. The O TDS spectrum also shows the onset of β peak formation as a shoulder at 760 K. The γ peak in O TDS spectrum is fully developed and resembles the γ peak in the spectrum from the Cs and O saturated surface (Fig. 5.3).

A similar evolution of TDS spectra is observed when the starting structure is Pt(111)(2×2)-Cs ($\theta_{Cs} = 0.25$) prepared at 295 ± 2 K (Figs. 5.8 a. and b.).

Dosing of 6.7×10^{-5} Pa s of O_2 (work function increase $1 - 1.5$ eV) on the surface at 295 ± 2 K results again in complete dissociation of O_2 (Fig. 5.8 a). O desorbs in a broad peak with maximum at 685 K (black curve) and no O_2 desorption is registered (red curve). The Cs (green curve) TDS spectrum shows one peak with maximum at 800 K.

Increased exposure of O_2 (1.3×10^{-4} Pa s, work function change of $2 - 2.5$ eV) causes a shift in the Cs peak maximum to 870 K (Fig. 5.8 b). The O_2 TDS spectrum shows two desorption peaks with maxima at 720 K and 850 K respectively, which can again be related to the β and γ peaks in Fig. 5.3. The O TDS spectrum also shows β and γ peaks, but in this case the intensity of the γ peak is significantly lowered when compared to the Cs saturated surface (Fig. 5.7). The small features in the O TDS spectra at low temperatures ($400 - 600$ K) are related to minor contamination of the surface.

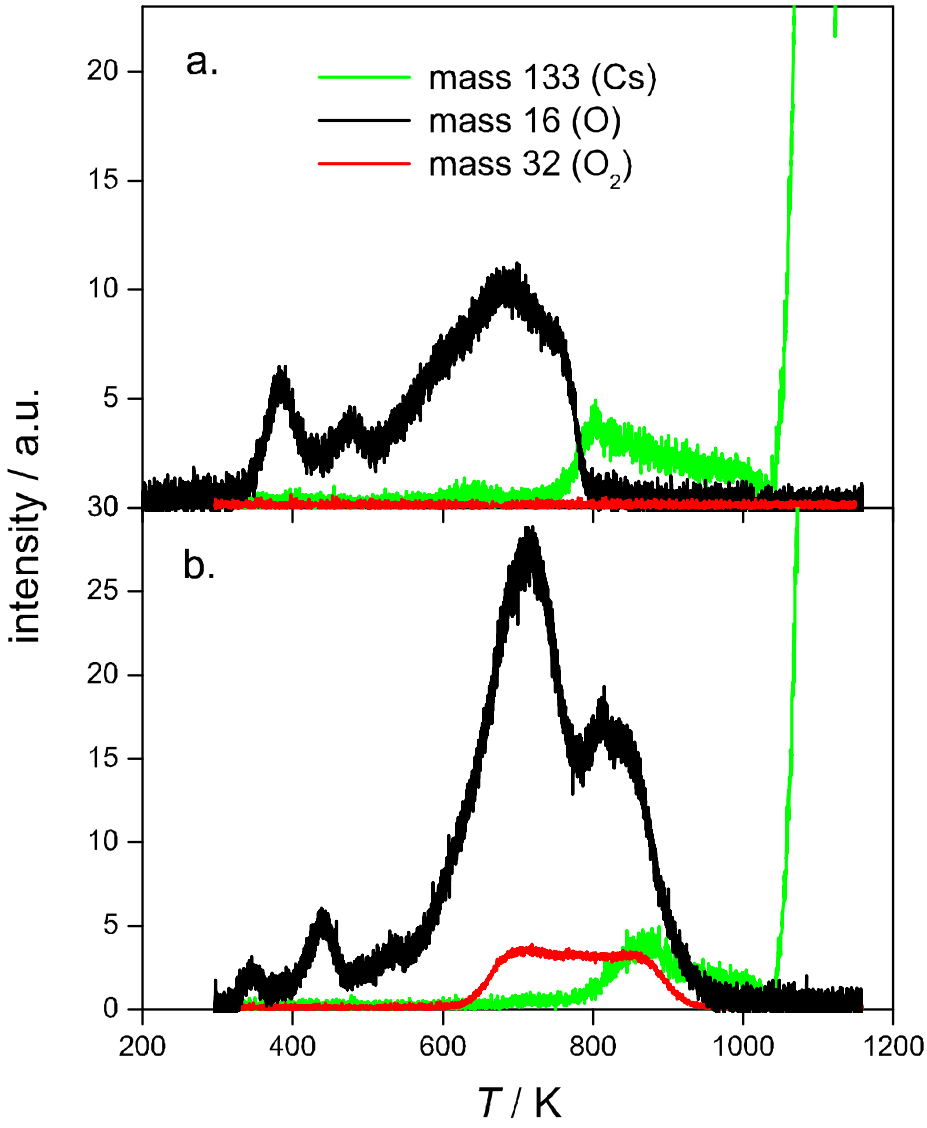

Figure 5.8: Second set of TDS spectra from the early stages of Pt(111)-Cs,O layer formation. The layers were prepared by dosing O_2 on Pt(111)(2×2)-Cs surface at 295 ± 2 K. O_2 exposures: (a) 6.7×10^{-5} Pa s and (b) 1.3×10^{-4} Pa s.

5.4.3 Iodine adsorption on Pt(111)-Cs,O

Fig. 5.9 shows the WF response of iodine adsorption on a Pt(111)-Cs,O layer prepared by exposing the Pt(111)(*ihcp*)-Cs surface to 1×10^{-7} mbar of O_2 at 295 ± 2 K until no further change of the WF was observed ($\approx 1.3 \times 10^{-3}$ Pa s). The adsorption of iodine on this layer results in a further increase of the work function by 1.5 eV. The AES measurement reveals the presence of O, I and Cs on the surface. The peaks for I and O in the AES spectra partially overlap, which makes coverage determination unreliable. If the I_2 and O_2 dosing order is reversed and O_2 is adsorbed on a Pt(111)$(\sqrt{7} \times \sqrt{7})R19.1°$-Cs,I layer, no WF change is observed. It can be concluded that the Pt(111)$(\sqrt{7} \times \sqrt{7})R19.1°$-Cs,I layer is passivated towards O_2 adsorption. Therefore, the dosing order during the ternary layer preparation affects the resulting surface structure.

The TDS spectra from a Pt(111)-Cs,O,I layer for Cs, I and O_2 are shown in Fig. 5.10. The I and Cs spectra have very similar shapes resembling the TDS spectra from the Pt(111)-Cs,I layers [77]. The main feature is a sharp desorption peak at 600 K, followed by a smaller broad peak with a maximum around 700 K. The TDS spectra of O_2 (mass 32) dramatically changes compared to the iodine-free Cs,O surface. Whereas multiple peaks in the case of Pt(111)-Cs,O spectra are found, only one sharp peak with a maximum at 640 K is present in the Pt(111)-Cs,O,I TDS. It should be noted that this peak is not aligned with either the Cs or I desorption peaks.

Exposure of the Pt(111)$(\sqrt{7} \times \sqrt{7})R19.1°$-I surface to oxygen did not lead any adsorption. In these experiments, the I TDS spectrum resembles the desorption of iodine without surface exposure to oxygen. There was no detectable desorption of O_2 or IO and also no WF change during O_2 dosing.

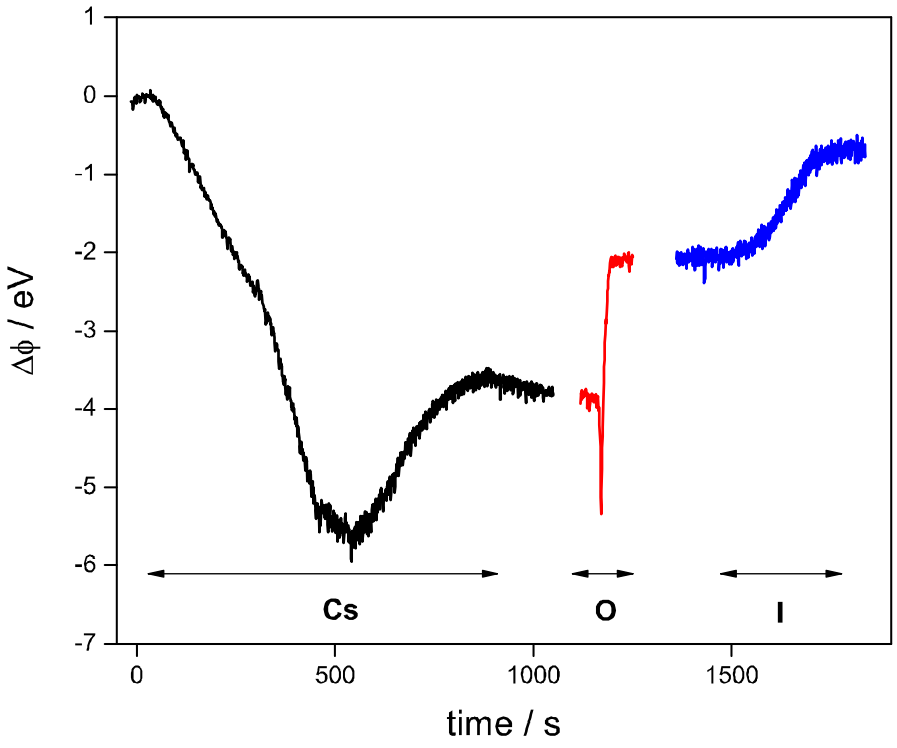

Figure 5.9: The black curve shows the WF response upon Cs dosing. The red curve corresponds to the subsequent WF change during O adsorption on Pt(111)(*ihcp*)-Cs ($\theta_{Cs} = 0.41$). The blue curve is the WF response upon I_2 adsorption on a Pt(111)-Cs,O surface. During dosing the Pt crystal was held at a constant temperature of 295 ± 2 K.

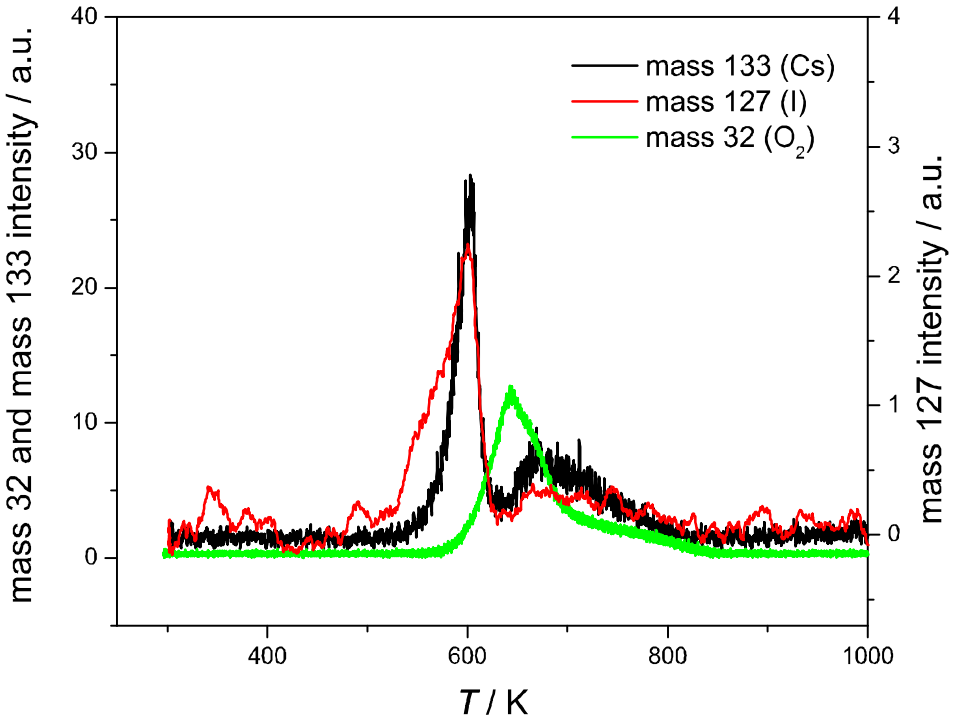

Figure 5.10: TDS spectra for various masses from Pt(111)-Cs,O,I. The layer was prepared by dosing O_2 on a Pt(111)(*ihcp*)-Cs surface to saturation, followed by I_2 adsorption to saturation. Black curve - mass 133 (Cs), red curve - mass 127 (I) and green curve - mass 32 (O_2). The heating rate is 5 $\mathrm{K\,s^{-1}}$.

5.5 Discussion

Oxygen coadsorption with alkali metals on transition metal surfaces is important in catalysis and has been extensively studied. The bulk of the literature for group 10 transition metal substrates is for coadsorption on Ni surfaces [83–89]. Nevertheless, some studies on Pt surfaces have been reported [5, 63, 72, 73, 90]. The current findings will be related to the literature and an adsorption/desorption model for the Pt(111)-Cs,O layer will be proposed.

5.5.1 Sub-saturation Cs adsorption

In this section, the initial WF decrease observed when O_2 is adsorbed on a Pt(111)(*ihcp*)-Cs surface will be discussed. The initial decrease has been observed for numerous O/alkali metal/transition metal coadsorption systems ([15, 84, 91] and references therein). However, the mechanism of this behavior is not well understood. Two competing adsorption models explaining this feature have been proposed, one by Rhead [14, 15], and the other by Heskett et al. [91].

For the Rhead model, the structure of the alkali metal layer is a key factor. When alkali metals are being adsorbed on a metallic surface, the atoms are initially considered as randomly distributed. When the surface coverage reaches a critical coverage (in most cases the coverage of WF minimum $\theta_{\text{min-alkali}}$), islands of dense, close packed structure start forming. These islands have a WF value close to the value of the pure alkali-metal crystal surface, which is higher than the WF at $\theta_{\text{min-alkali}}$. As island growth continues, more surface is covered and the WF continues to increase toward saturation (Fig. 5.1). Oxygen can adsorb only under these dense islands and the maximum amount of sublayer adsorbed oxygen is directly proportional to the size of the islands [15]. The sublayer adsorption is also responsible for the sharp initial work function decrease. Adsorption of oxygen below the Cs plane causes the formation of polar Cs-O bonds which results in the formation of a dipole array with

negative charges close to the substrate. Once all sub-layer adsorption sites have been occupied, oxygen starts to adsorb on other available sites located either in-plane or above Cs. This cause the WF to increase.

The Rhead model further divides adsorption behavior into two categories. In category I, the initial WF decrease upon oxygen adsorption occurs for coverages both lower and higher than $\theta_{\text{min-alkali}}$. Category II describes adsorption behavior where the WF initially decreases only for alkali coverages higher than $\theta_{\text{min-alkali}}$. For category I behavior, oxygen induces the formation of dense alkali islands and adsorbs underneath. Therefore, the initial WF decrease upon O_2 adsorption is independent of the initial alkali coverage. For category II behavior, the densely packed islands must exist prior to oxygen adsorption and hence alkali atoms must attain the critical coverage on the surface allowing the island formation.

The competing model by Heskett et al. [91, 92] explains the initial WF behavior in terms of increased polarization of Cs-Pt bonds. In the initial stages of oxygen adsorption, electronegative O polarizes the Cs-Pt bond and the WF decreases. The increase in the bond polarization is caused by the electrostatic field induced by coadsorbed O. This field acts on the Cs-Pt bond increasing the valence electron-Cs nucleus separation and minimizing the potential energy.

The progression of induced WF change depends on the interplay between the WF increase due to the O-Pt dipole moment (opposite polarity of the Cs-Pt dipole) and the WF decrease due to the further polarization of Cs-Pt bonds. This model predicts a decrease in the WF for planar layers and layers where O is above Cs.

Our oxygen adsorption on Pt(111)(*ihcp*)-Cs data can be suitably explained by the Rhead model, category II (Fig. 5.2). The onset of formation of densely packed Cs islands begins at the minimum WF. This minimum corresponds to the Pt(111)(2×2)-Cs structure which does not accommodate any O sub-layer adsorption, as there is no indication of an initial decrease of the WF. As the Cs coverage increases, the LEED

observations show the onset of the formation of a dense Pt(111)($\sqrt{3} \times \sqrt{3}$)R30-Cs layer, which changes into saturated Pt(111)(*ihcp*)-Cs [40,47,62,77]. We propose that both Pt(111)($\sqrt{3} \times \sqrt{3}$)R30-Cs and Pt(111)(*ihcp*)-Cs are able to accommodate sub-layer oxygen adsorption and therefore the WF decrease upon O_2 adsorption appears only for $\theta > \theta_{\text{min-alkali}}$.

The exact position of the sub-layer oxygen is not directly determinable from our measurements and will be discussed later. However, we note here that in order to form an electrical double layer, the O does not need to be directly below the Cs. Similar to the case of the Rh(0001)($\sqrt{3} \times \sqrt{3}$)R30-Cs,O layer [93], it is possible that O may be located in between Cs atoms but directly interacting with the substrate. Because O atoms are significantly smaller than Cs, negatively charged O can be located closer to the substrate, and together with the positively-charged Cs, forms the electrical double layer responsible for the WF decrease.

The difference in adsorption behavior between Cs,I and Cs,O can be explained by the different size of adsorbed atoms. The radius of O^- is 1.76 Å, whereas the radius of I^- is 2.20 Å. Therefore, oxygen atoms can move more easily through a Cs layer and fit better under the Cs than I^-, which is similar in size to the the Cs^+ ions. The iodine cannot easily penetrate below a Cs layer and therefore the initial decrease of the WF is minimal. A more detailed discussion of planar versus bilayer ionic structures can be found in [77].

In the current study, the model developed by Heskett et al. can be rejected for two reasons: incompatibility with the observed WF behavior upon I adsorption on Pt(111)(*ihcp*)-Cs (Fig. 5.1) and the WF response at low temperatures:

1. For I adsorption on Pt(111)(*ihcp*)-Cs, only a very shallow or no minimum was measured, dependent on the quality of the ordering of the Pt(111) substrate. If the Heskett et al. model were applied in this case, in-plane iodine adsorption on Pt(111)(*ihcp*)-Cs should cause a similar significant initial WF decrease. This

is because both I and O are electronegative species, and therefore both are expected to have a similar re-polarization effect on the Pt-Cs bond. This effect is field induced and therefore relatively independent of the exact position of adsorbed atoms in the unit cell.

2. Further evidence comes from the WF response upon O_2 adsorption on Pt(111)(*ihcp*)-Cs at low temperatures. In this case, no initial WF decrease is observed, suggesting a temperature activated process is present. This is expected for sub-layer adsorption, where Cs atoms need to move from their equilibrium positions in order to accommodate O atoms. At low temperatures, the thermal energy of adsorbed O atoms is not sufficient to overcome the activation barrier for sublayer adsorption and O is adsorbed above the Cs layer. The observed disappearance of the initial decrease at low temperature is therefore inconsistent with the Heskett et al. model. According to that model, the re-polarization of Cs-Pt bond would occur independently of the O position in the unit cell (because it is a field effect). As a result, the observation of the initial WF decrease is predicted by this model to appear even at low temperatures.

5.5.2 Desorption and structural behavior of Cs saturated Pt(111)-Cs,O

Our TDS and LEED results from Pt(111)(*ihcp*)-Cs,O have some commonalities with the data measured by Garfunkel at al. for a Pt(111)-K,O layer [5]: i) the O TDS spectrum has multiple sharp desorption peaks, ii) annealing the sample between TDS peaks results in ordering of the surface, and iii) the presence of oxygen thermally stabilizes the adsorbed alkali metal atoms. Interestingly, the spectra taken for $\theta_{\mathrm{KO}} = 0.65$ and $\theta_{\mathrm{KO}} = 0.9$ are very similar to our O_2 TDS spectra from Pt(111)(2×2)-Cs,O ($\theta_{\mathrm{Cs}} = 0.24$, Fig. 5.3) and Pt(111)(*ihcp*)-Cs,O ($\theta_{\mathrm{Cs}} = 0.34$, Fig. 5.4). Therefore the characteristic shape of the TDS spectra is independent of the different size of the

alkali metal atoms, pointing to the same bonding mechanism in each case.

The unexpected feature in our experiments is the presence of changing O:O_2 intensity ratios in the spectra, suggesting some desorption of O in its atomic form. On the clean Pt(111) surface, the adsorbed oxygen recombines to O_2 molecules prior to desorption [57, 58]. The associative behavior can be explained by formation of a strong O-O bond during desorption, which stabilizes the O_2 molecule. Our results show that for most of the measured TDS spectrum, O leaves the surface as O_2, as shown by the constant O:O_2 ratio (Fig. 5.3). However, the γ peak consists of two parts. The high intensity peak with the sharp trailing edge corresponds to atomic O desorption and the low intensity, broader part corresponds to O_2 desorption. This observation points to the existence of an adsorption state on the surface that favours the desorption of the atomic O (the "γ-atomic" state). Such desorption behavior can be caused by either a strong Cs-O interaction, or a hindered surface diffusion of adsorbed O atoms preventing oxygen transition to the activated intermediate state needed for O_2 desorption. Most likely both phenomena occur, because the layer is very crowded, which hinders the surface diffusion, and the ordering seen by LEED implies that there is a strong interaction between Cs and O. The γ-atomic peak component is very sharp with an almost vertical trailing edge, suggesting the zero-order desorption, i.e., the activation energy for desorption of γ-atomic oxygen does not depend on the oxygen coverage.

As the oxygen is removed in the γ peak, the Cs is no longer stabilized and it is released from the surface (Fig. 5.3). There is no significant Cs desorption for temperatures below 820 K, i.e. the Cs coverage remains at its initial value of 0.32 ± 0.07 (from AES) until it reaches this temperature. This is in contrast with Cs adsorbed on the Pt(111), where the high coverage Cs ($0.25 < \theta_{Cs} < 0.41$) desorbs at temperatures below 600 K [5,62]. We suggest that this thermal stabilization is caused by attractive electrostatic interactions within the Cs,O layer [16,77]. Interestingly, the anomalously adsorbed (low coverage) Cs does not directly interact with the coadsorbed O and the

Cs spectrum is unaffected [62].

Only a small amount of oxygen is needed to stabilize the Cs and delay its desorption and the thermal stabilization is clearly caused by the oxygen in γ-atomic state. This can be inferred from the TDS spectra for the initial stages of O_2 adsorption (Fig. 5.7 a), where the majority of oxygen desorbs in the O TDS peak and the O_2 TDS peak is small in comparison.

A stabilization effect is also seen for Pt(111)-Cs,I [77]. In this case, however, the interaction between coadsorbed Cs and I atoms and the substrate is weaker, and a sharp, overlapping peak for Cs and I appears at 500 K. The same sharp peak is also observed for I_2 adsorption on Pt(111)(*anom*)-Cs (low coverage Cs) pointing to a similar interaction between Cs and I, regardless of the initial coverage [62].

The thermal stabilization in Cs,O layers is accompanied by structural changes. Heating the Cs saturated Cs,O layer to 650 K causes ordering to a sharp (4×4) LEED pattern (Fig. 5.5), and further heating to 750 K leads to a less sharp (4×4) LEED. Evidently, the amount of coadsorbed oxygen significantly affects the ordering and we propose that the increased ionicity of the layer is responsible. The intensity of electrostatic field on the surface induced by polar Cs-O and O-Pt bonds increases with increase in the electronegative oxygen coverage. The result is a secondary increase in the polarization of the Cs-Pt bond minimizing the overall electrostatic energy of the layer, which further leads to strengthened electrostatic interactions between adsorbates of opposite polarity. Therefore sharper LEED patterns are observed for Cs,O layers with higher oxygen coverage.

The same ordering behavior was also observed for the K,O layer [5]. In that case, heating the layer to 650 K caused formation of the (4×4) LEED pattern, but at 750 K the K,O layer underwent a transition to a (10×2) structure. Another adsorption system where the coadsorption of electronegative and electropositive species causes ordering is Pt(111)-Cs,I [77]. There, dosing electronegative iodine on the

Pt(111)(*ihcp*)-Cs layer causes formation of a Pt(111) (4×4)-Cs,I layer.

We hypothesize that the common (4×4) LEED pattern in all three adsorption systems is due to the ionicity of Cs bonding within the layers [18]. If the bonding were more covalent, the different bonding of Cs to I, O and Pt would likely produce different surface geometries for each layer.

In the initial stages of oxygen adsorption on the Pt(111)(*ihcp*)-Cs surface, oxygen is adsorbed in the γ-atomic state, which allows desorption of O in its atomic form. This can be seen in the TDS spectra from the early stages of Cs,O layer formation (Fig. 5.7). The O peak at 785 K is the most prominent feature. As the coverage of oxygen on the surface increases, the amount of desorbing O_2 also increases, as seen from the developing β and γ-molecular peaks (Fig. 5.7 b.). We conclude that the γ-atomic state is filled first, and once it is saturated the oxygen populates the β and γ-molecular states simultaneously.

5.5.3 Cs coverage dependent effects

In this section we discuss the commonalities and differences between the experimental results obtained from the Cs-saturated Cs,O layer and results obtained from the Cs,O layer with medium Cs coverage. The TDS spectra for all measured masses have desorption peaks at the same positions, but the relative intensities of those peaks are different (Figs. 5.3 and 5.4). Interestingly, the WF response upon oxygen adsorption depends dramatically on the initial Cs coverage (Fig. 5.2) and the observed surface structures during heating are also different (Figs. 5.5 and 5.6).

Comparison of the TDS spectra in Figs. 5.3 and 5.4 and the AES measurements (section 5.4.1) clearly imply that the amount of adsorbed oxygen depends on the initial Cs coverage. At lower Cs coverages, there is a significant reduction in the γ-atomic to β peak ratio and a reduction in the O_2 and O TDS peak at 400 K. Unfortunately, the O_2 and O TDS peak intensities cannot be directly compared between the spectra in

Figs. 5.3 and 5.4 because the intensity changes slightly from experiment to experiment and the sensitivity of the instrument had to be different for the O TDS from the Pt(111)-Cs,O with medium Cs coverage (Fig. 5.4). The change in the relative γ peak intensity in the O_2 TDS spectrum is significantly more dramatic then for the α and β peaks. The α:β peak intensity ratio is slightly higher for the surface prepared from Pt(111)(2×2)-Cs, pointing to an increase of oxygen coverage in the α adsorption state. However, the increase in the α:β ratio is within the experimental error.

The γ oxygen does not seem to adsorb underneath Cs in the Pt(111)(2×2)-Cs structure as there is no observed WF decrease at the initial stages of oxygen adsorption (Fig. 5.2). This can be explained by the lower Cs coverage. The initial Cs coverage is 0.25 in this case and therefore the surface is only partially covered. Oxygen has more room to accommodate in between Cs atoms and does not need to adsorb underneath Cs in order to directly interact with the substrate.

In the initial stages of oxygen adsorption, the behavior is similar to the Cs saturated layers. First, oxygen adsorbs into the γ-atomic state and once that is filled it adsorbs simultaneously into the β and γ-molecular states (Fig. 5.8).

The γ oxygen also seems to stabilize Cs on the Pt(111)(2×2)-Cs surface, but the interactions between Cs and O are not as strong as in the case of the Cs-saturated Cs,O layer discussed above. As a result, the γ-atomic TDS peak is rather broad and shifted to lower temperatures when compared to Cs-saturated layers (Fig. 5.8). This is most likely a consequence of the less crowded layer at the initial stages of adsorption (i.e., Cs and O atoms are more separated and therefore the interaction is weaker). The initial Cs coverage also plays a role in the structural changes during desorption. When O_2 is adsorbed on Pt(111)(2×2)-Cs, a Cs,O layer with a (6×6) LEED pattern forms upon heating to 650 K. The structural difference compared to the saturated Cs structure is not surprising given the fact that the initial stages of layer formation also differs depending on the initial Cs coverage e.g., the initial work function decrease is missing in the case of lower Cs coverage, and the γ-atomic peak

is smaller).

5.5.4 Bonding states in the Pt(111)-Cs,O layer

Alkali metal-O layers on transition metal surfaces

To better understand the structure and bonding arrangements within a Pt(111)-Cs,O layer, we recapitulate what is already known about the coadsorption of alkali metals and oxygen on transition metal surfaces. We focus on Pt(111) and Ni surfaces.

Studies of oxygen adsorption on Pt(111)-K at 300 K by Pirug at al. [73] using UPS and XPS found two consecutively filled oxygen adsorption states (A and B). The A state, appearing at lower O_2 doses, was assigned to a tightly bound K-O species. It was suggested that this molecule is likely not K_2O due to the difference in position of the UPS peak relative to oxidized bulk K samples. The B peak, found at higher O_2 doses, was attributed to adsorption of O atoms on bare Pt between K-O islands. This assignment was based on changes in the Pt UPS peak intensity at 0.25 eV, which is characteristic for a clean surface. The coverage of oxygen on the potassium-free part of Pt(111) was calculated as $\theta_O = 1.1$ or higher [73]. The existence of K-O species was suggested to promote the adsorption of O on the bare Pt surface.

Cassuto et al. [90] found the same A-state UPS peak in their study of O_2 adsorption on low-coverage Pt(111)-K. However, they suggested that this peak could be safely assigned to K_2O because shifts around $2-3$ eV are consistent with the bulk values. K_2O can exist in the gas phase [5], but the nature of the K-O interaction on a Pt surface is still unclear. The K_2O stoichiometry is believed to be one of the few stable arrangements in ionic layers, and is important in understanding the formation of 2D ionic crystals [18].

An XPS study by Ayyoob and Hedge [72] of Cs and K adsorption on a Pt(*poly*)-O surface concluded that oxygen is predominantly dissociatively chemisorbed and

not necessarily associated with any particular species such as superoxide (KO_2) or peroxide (K_2O_2). In contrast, Riwan et al. [63] from an Angular Resolved Ultra-violet Photoelectron Spectroscopy (ARUPS) study of oxygen adsorption on a partially-covered Pt(111)(2×2)-Cs layer tentatively identified two different oxygen species: a peroxo-like O_2^{t-}, with $t \lesssim 2$ at low O_2 exposures, and CsO_2 at 6.5×10^3 Pa s (50 L) O_2 exposures.

Adsorption of oxygen on alkali-metal precovered Ni surfaces shows slightly different results than described above. For low alkali metal coverages, the alkali-metal and oxygen are not directly bonded, and interactions between adatoms are substrate mediated [86, 87]. As the coverage of alkali metal atoms increases, the interaction between oxygen and alkali-metals also increases [86, 87]. The oxygen-substrate bond becomes stronger and more ionic [83] and charge transfer takes place from the alkali metal to oxygen [86]. The Spot Profile Analysis-LEED (SPA-LEED) and Scanning tunneling microscopy (STM) study by Murray et al. [89] on Ni(100)-K,O showed that at low coverages K is adsorbed on top of the oxygen-covered substrate [89]. Ikari et al. [86] also suggested that at high O coverages, oxygen atoms tend to be transported to subsurface sites. In contrast, data from normal exit Li^- spectroscopy on Ni(111)-Cs,O were explained by O atoms lying *above* Cs adsorption sites for high Cs coverages and low O exposures [85].

Oxygen bonding states

In this section we tentatively assign the observed TDS and work function experimental features to possible adsorption states.

In the initial stages of oxygen adsorption on Pt(111)(*ihcp*)-Cs, the γ-atomic state is populated (Fig. 5.7 a). Given the initial work function decrease at the beginning of adsorption (Fig. 5.2), the oxygen in this adsorption state likely adsorbs under the Cs layer. As soon as the γ-atomic state is saturated, oxygen starts to adsorb in the

γ-molecular state. This state clearly differs from the γ-atomic state as identified from the different desorption behavior (desorbs as O_2) and from the opposite sign of the work function change, which increases the work function upon adsorption.

The oxygen adsorbed in both the γ-atomic and the γ-molecular states are both closely bound to the alkali metal. We identify the γ oxygen state with the oxygen A adsorption state of Pirug at al. [73] or the K_2O species of Cassuto et al and Garfunkel et al. [5, 90]. Our assignment is based on the observation that oxygen in the γ states causes the stabilization and ordering of the Cs,O structure (Figs. 5.3 and 5.5), and is therefore strongly interacting with Cs. Our experimental results do not allow us to decide if oxygen in the γ-atomic or γ-molecular states or both are responsible for the stabilization and ordering.

Oxygen in the β adsorption state (desorbing in the β O_2 TDS peak) improves the ordering of the Pt(111)(4×4)-Cs,O (Fig. 5.5), but in contrast to the γ state, does not desorb with Cs (Fig. 5.3). We suggest that the oxygen in the β state is still interacting with Cs (as evidenced by the sharp (4×4) LEED pattern), but to a lesser extent than the γ oxygen. As the β state fills, the overall electrostatic interactions of electronegative oxygen with electropositive Cs increase and the layer shows better ordering. An increase of the Cs-O and Cs-Pt bond polarization with increasing oxygen coverage is expected. Cs atoms will become more charged, which is in accordance with the observations from alkali-metal/oxygen/Ni surfaces [86, 87].

It is tempting to assign oxygen in the α adsorption state to oxygen bound to the bare Pt surface between Cs,O islands (the B state assigned by Pirug et al.), but we have insufficient evidence to prove this.

5.5.5 Proposed structure of the Cs,O layer

The bonding types deduced above allow some sensible suggestions for the atom locations within the unit cell. We focus on the arrangement for oxygen in the γ and β

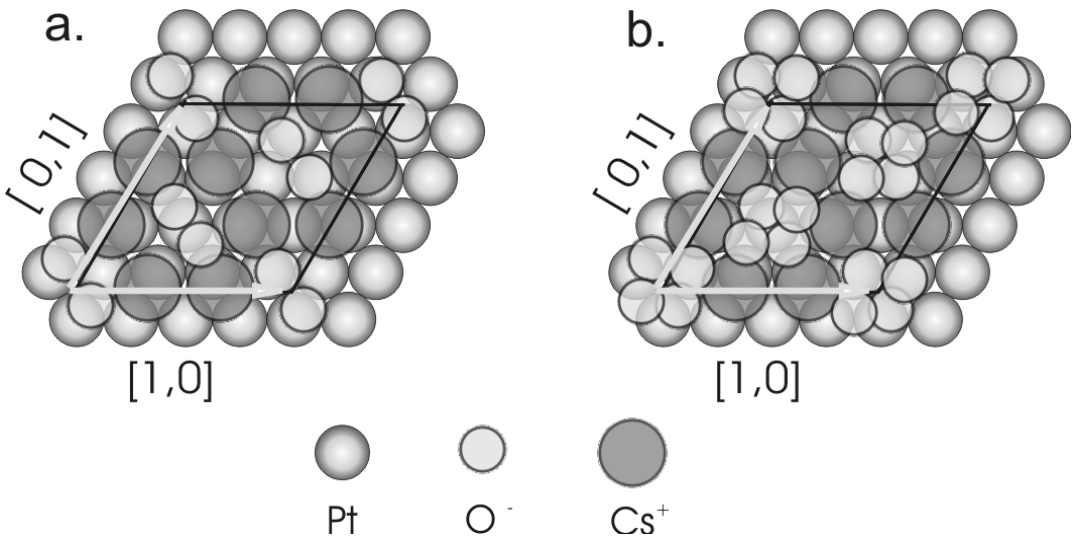

Figure 5.11: Suggested surface structures for Pt(111)-Cs,O layer after heating to 650 K (b., Cs_2O) and to 750 K (a., CsO)

adsorption states. Given the observed (4×4) LEED pattern and the expected ionicity of the Cs-O bond, we suggest a similar unit cell arrangement as assigned in our previous work for Pt(111)(4×4)-Cs_2I [77]. We propose that in the Pt(111)(4×4)-Cs,O arrangement, Cs atoms form a honeycomb lattice with O atoms located in the centers of the hexagons (Fig 5.11). Fig. 5.11a. shows the proposed structure after heating the Cs and O saturated Pt(111)-Cs,O layer to 750 K. Fig 5.11b. shows the proposed structure after heating to 650 K.

From our O_2 TDS spectra, we estimate that about 1/3 of the O coverage at saturation corresponds to each of α, β and γ peaks (Fig. 5.3). Given that the Cs:O ratio is 1:3.2 at saturation (from AES measurement), ratios of 1:2 at 650 K and 1:1 at 750 K are reasonable. The same Cs:O ratios of 1:2 and 1:1 were also suggested as most probable on Pt(*poly*)-Cs,O surfaces by Ayyoob at al. [72]. Therefore in our proposed arrangements, two (1:1 ratio) or four (1:2 ratio) O atoms, respectively, are located in the center of the hexagons. This unit cell geometry, with negative charges located in the center of positively-charged hexagons, was identified by Wang at al. [18]

as one of the more stable arrangements for 2D ionic layers. A high packing density of O is reasonable, because adsorbed O is significantly smaller than adsorbed Cs, and it is well known that high O coverages of up to 2.9 ML can be prepared on Pt surfaces by various techniques [54, 57].

5.5.6 Iodine adsorption on Pt(111)-Cs,O

In this section, we will discuss the Cs,I,O adsorption/desorption experiments. We show that oxygen in this layer does not interact with Cs or I, but rather directly interacts with bare Pt sites in between the Cs,I islands.

Dosing iodine on a Pt(111)-Cs,O layer causes the WF to increase without any initial decrease (Fig. 5.9). As discussed in section 5.5.1, this means that iodine adsorbs on or in the Cs,O layer, but not underneath it. From the WF measurement alone, it cannot be established if oxygen simultaneously desorbs during iodine adsorption. However, O_2 TDS spectra clearly show that a significant amount of oxygen is left on the surface after I_2 dosing (Fig. 5.10). The LEED pattern from a Pt(111)-Cs,O,I surface is diffuse, showing the lack of long range order in the layer.

By comparing I TDS (mass 127) from Pt(111)-Cs,I,O with the I TDS from Pt(111)-Cs,I [77], the bonding properties of iodine in the layer can be examined. The Cs and I signals from the Pt(111)-Cs,O,I layer resemble those from Pt(111)$(\sqrt{7}\times\sqrt{7})R19.1$-Cs,I with a characteristic sharp peak around 500 K. It is therefore concluded that most of the iodine is interacting with Cs in the layer, the oxygen presence does not influence I or Cs desorption, and the oxygen has only weak interaction with both Cs and I.

Given the evidence above and comparison with literature data, we suggest that the oxygen in the Pt(111)-Cs,I,O is bonded to the Pt substrate and is located between Cs,I islands. This suggestion is mainly based on the significant similarities between O_2 TDS spectra from Pt(111)-Cs,I,O and from Pt(111)-O at high coverage

O ($\theta_O = 1.26$) [57]. The spectrum of Weaver et al. [57] is identical to our measured spectrum, showing that O in the Cs,I,O layer most likely desorbs from dense islands of O which are not interacting with Cs,I. Similar surface structures for K,O and O islands were used to explain UPS experimental results by Pirug et al. [73] (see section *5.5.4*). Adsorption between Cs,I islands was also observed for oxygen adsorption onto a Pt(111)(4×4)-Cs_2I surface [77].

However, other explanations are possible. Iodine can adsorb on top of the layer, effectively trapping the oxygen underneath. This would also result in a work function increase due to the iodine electronegativity. When the surface is heated, the Cs and I desorption at 500 K would allow oxygen (originally trapped below the layer) to leave the surface in the sharp peak resembling the desorption from Pt(111)-O surface. This mechanism could also lead to the TDS spectrum in Fig. 5.9.

5.6 Conclusions

Coadsorption of oxygen and Cs on Pt(111) results in complex structures with oxygen bonding to the various surface sites.

During the oxygen dosing on the Pt(111)(*ihcp*)-Cs, oxygen is first adsorbed in a site located below the Cs (γ-atomic site), which causes the initial work function to decrease. As the oxygen coverage increases, oxygen starts to adsorb in a different adsorption state (γ-molecular). When desorbing, γ-molecular oxygen leaves the surface as an O_2 molecule and γ-atomic oxygen leaves in its atomic form. The γ-molecular oxygen TDS peak overlaps with the Cs TDS peak. Therefore we conclude that the γ-molecular oxygen closely interacts with Cs. The oxygen in both γ states is responsible for the thermal stabilization of Cs on the surface.

Further oxygen dosing causes oxygen to adsorb in the β adsorption state. This oxygen is not as strongly bound to Cs as the γ oxygen, but some interaction exists

as seen from the increased ordering of the layer and sharper (4×4) LEED pattern. This LEED pattern was assigned an arrangement where oxygen atoms are located in the centers of hexagons of Cs atoms.

The observed (4×4) LEED pattern is the same as for the Pt(111)(4×4)-Cs_2I surface, pointing to the similarity of bonding between Cs-O and Cs-I. Given the large electronegativity of both O and I and the low electronegativity of Cs, this finding is not surprising. Both layers are expected to show ionic bonding character, resulting in the similar observed structures.

We suggest the following behavior for I adsorption on Pt(111)-Cs,O. Because I interacts more strongly with Cs than O, oxygen is replaced by I in the Cs,O layer. The resulting surface consists of Cs,I islands with oxygen adsorbed in between those islands. Upon heating the surface, oxygen desorbs independently of the Cs,I islands. Other explanations of the observed adsorption/desorption behavior, such as O adsorbed below the Cs,I layer, are also possible.

5.7 Acknowledgements

This work was financially supported by the Natural Sciences and Engineering Research Council (NSERC) of Canada.

Chapter 6

Monte Carlo investigation of cesium adsorption on a Pt(111) surface

6.1 Abstract

A Monte Carlo model for alkali metal adsorption/desorption from transition metals was proposed. Inclusion of the experimentally observed surface phases to the model allowed to fit the experimental TDS and work function curves from Pt(111)-Cs adsorption system with unprecedented detail. The long range interactions between adsorbed atoms are assumed to have a dipole-dipole character and are calculated from first principles. We found that the inclusion of depolarization into the model plays a significant role in modeled thermal desorption curves, however, it has only a minimal effect on the modeled work function of the surface.

6.2 Introduction

Alkali metal adsorption on transition metal surfaces received significant attention in the past due to its theoretical and experimental simplicity and its numerous industrial applications [7, 11, 12, 94, 95]. In this paper, we provide a theoretical framework explaining the experimentally observed behavior of Cs adsorbed on Pt(111) surface. With the same model, we are able to fit measured experimental WF and thermal desorption spectroscopy (TDS) data with satisfactory results.

The first attempt to explain the characteristic WF response upon an alkali metal adsorption on a metal surface was done in the work of Topping [6, 10]. In this dipole model, the curvature in the initial WF decrease is related to the depolarization of originally ionic alkali-substrate bonds. The depolarization is caused by the electrostatic field induced by other adsorbed atoms. According to the Topping model, the WF change is described by Eq. 6.1 [6, 96].

$$\Delta\phi = -\frac{e}{\varepsilon_0} \cdot \frac{n_0 \mu_0 \theta}{1 + F\alpha' \left(n_0 \theta\right)^{\frac{3}{2}}} \tag{6.1}$$

Here e is elementary charge, n_0 is the substrate surface density in atoms per m^2, θ is the fractional coverage, μ_0 is dipole moment at $\theta = 0$, F is a geometric factor dependent on the substrate geometry and α' is the polarizability volume ($\alpha' = \alpha/4\pi\varepsilon_0$, α is polarizability in SI units). Although, the Topping classical view was later justified by the quantum Langmuir–Gurney (LG) model [8, 9, 11], Eq. 6.1 is capable of explaining only the first decreasing part to the minimum of the WF curve corresponding to the initial stages of adsorption.

Alternative models were developed to better explain the WF increase at higher alkali coverage. Verhoef et al. [13] suggested that the increasing part of the WF response is caused by a change of the adatoms polarizability α. At low coverages, α is close to the polarizability of gas phase alkali metal ion and as the coverage

increases, the polarizability also increases to the value of the bulk alkali metal atoms. This model fits the experimental WF results perfectly. However, as discussed below, it fails to explain the Thermal Desorption Spectroscopy (TDS) features.

Another explanation for the WF curve was provided by Rhead [14, 15]. He suggested, based on the theory by Sidorski [97], that the WF minimum corresponds to the initiation of a dense (2-D solid) phase condensation. As the coverage increases, the condensed phase islands grow and the WF approaches the value of the bulk alkali metal surface. The same approach was taken by Neugebauer and Scheffler to explain the WF change during Na and K adsorption on Al(111) [98] with satisfactory results.

Models incorporating bond depolarization have also been used to explain the TDS spectra from alkali metal layers adsorbed on various substrates [16, 17, 96]. Many of these spectra are characterized by a broad adsorption peak with a "plateau" at low temperatures [5, 96, 99–102]. Even though the general broad shape has been attributed to repulsive interactions within the layer [16,17], the fine features, e.g., the low temperature "plateau", are yet to be explained.

The first approach to model the TDS spectra relied on the Topping model, in which adsorbed atoms are substituted by point charges [16,96]. The total electrostatic energy of the adsorbed point charges is calculated from the model and then related to the activation energy of desorption ($E_{\mathrm{d}}(\theta)$). The desorption rate is found from

$$r(\theta, T) = -n_0 \frac{d\theta}{dt} = k_0 n_0 \theta \exp\left(-\frac{E_{\mathrm{d}}(\theta)}{RT}\right) \tag{6.2}$$

where k_0 is the preexponential factor, T is the absolute temperature and R is the gas constant. TDS spectra modeled by this approach match the trailing edge of experimental spectra, but fail to explain the "plateau" at lower temperatures.

The second method (Uñac et al.) is based on Monte Carlo (MC) simulations [17]. The Uñac et al. model is capable of mimicking the fine TDS features by incorporating only close neighbor interactions and by introducing an "attenuation function" to

calculate $E_{\mathrm{d}}(\theta)$. The close neighbor interactions and attenuation function are model fitting parameters and are not determined from electrostatic interactions. Therefore the model is rather empirical and does not explain theoretically the observed behavior.

The essence of our model is in the consideration of various adsorption phases on the surface. The advantage of the MC approach in our case is that we determine the relative surface coverage of each phase during the desorption simulation. Using this information we can also find the WF change of the surface as a function of coverage. The explicit knowledge of the size and number of islands for each phase is not needed to successfully model the TDS spectrum and WF curve because the essential variable (the relative surface coverage of each phase) is independent on the surface topology. Therefore, we use a simplified version of MC algorithm, where only the number of atoms in each phase are determined at each step and the interaction energies are found from a mean field electrostatic calculation. Our MC model could also be extended to include short range interactions and explicitly model the island growth on the surface, but this would increase the complexity of the model without improving the quality of the simulated curves fits to the experimental data. In our case the desorption energies are calculated from an adiabatic "Maschhoff" electrostatic model which includes the depolarization effect. In the MC model each adsorption phase has a different set of parameters (μ and α') describing the response to the induced electrostatic field. Such differences between adsorption phases are expected because each adsorption phase will interact differently with electrostatic field due to the variations in electronic structure.

In the case of Cs on Pt(111), the existence of multiple phases is well supported by experimental evidence. [40, 47, 62, 77]. In the initial stages of adsorption, Cs forms a strong ionic bond with the Pt substrate (anomalous adsorption) [62]. The LEED for low-coverage Cs is diffuse suggesting the lack of a long range order. Increasing the Cs coverage results in a formation of Cs islands with (2×2) LEED. Eventually, the substrate becomes fully covered with the (2×2) overlayer and the work function (WF) reaches the minimum (Pt(111)(2×2)-Cs surface). Further Cs dosing induces

Pt(111)($\sqrt{3} \times \sqrt{3}$)-Cs island formation which then transform to the Cs saturated Pt(111)(*ihcp*)-Cs incommensurate hexagonal closely packed layer.

6.3 Experimental

Experiments were performed in a custom built, stainless steel UHV chamber equipped with a Low Energy Electron Diffraction (LEED) optics (used also for Electron Auger Spectroscopy (AES)), a Kelvin probe for work function measurements and a Hiden HAL 321 mass spectrometer. In order to improve the signal-to-noise ratio in TDS, spectra were measured using a custom lock-in detection scheme [25]. More details about the experimental setup are in [62].

The (111) platinum crystal surface was prepared from a Pt boule grown by Metal Oxides and Crystals Ltd. The boule was cut with a diamond saw, pre-polished with diamond paste, aligned by back-Laue X-Ray diffraction and polished again with successive grades of diamond paste (Beuhler Ltd.). The final polishing step was done with a fine aluminum oxide slurry (0.05 μm).

Prior to each set of experiments, the surface was cleaned by Ar^+ ion sputtering, followed by an annealing to 1150 K. The crystal was also periodically tested for impurities by annealing in a oxygen atmosphere. Details about the crystal preparation can be found in [62].

Cs was dosed using a SAES cesium dispenser (SAES Getters, Cs/NF/2.2/12 FT10+10) located 10 cm from the surface. Cs atoms were collimated with a stainless steel tube. The purity of the layer was determined by measuring the work function during the dosing. The layer was considered clean if $\Delta\phi$ at the minimum was lower than -4 eV [62].

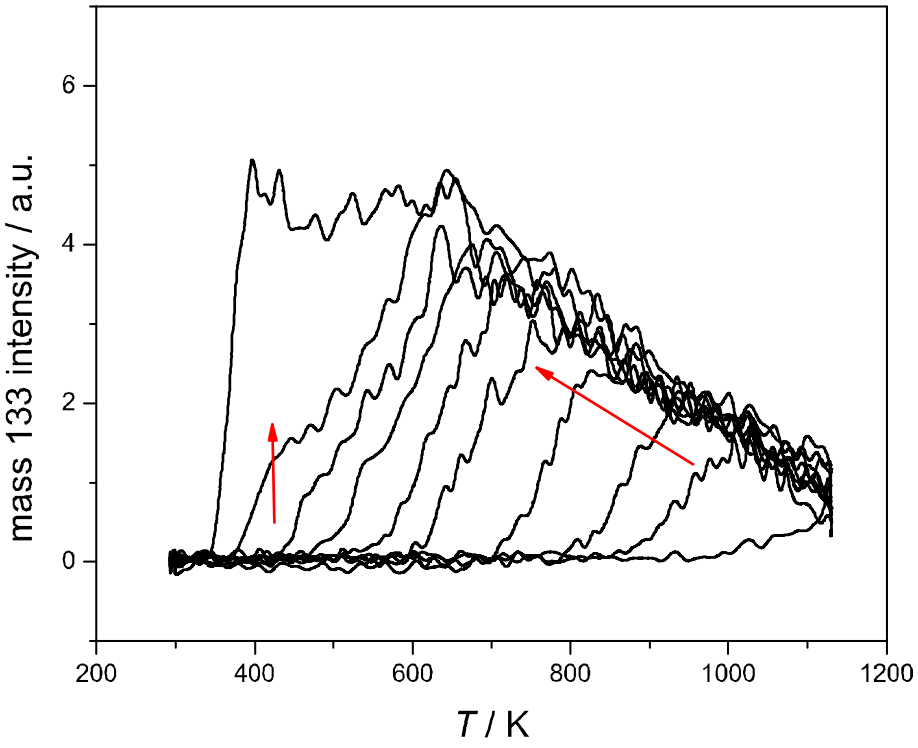

Figure 6.1: TDS spectra from Cs covered Pt(111) surfaces. Pt(111)-Cs layers were prepared at 295 K. Different curves correspond to the different initial coverages of 0.41 (full ML), 0.35, 0.31, 0.29, 0.26, 0.24, 0.21, 0.18, 0.16, 0.15 (from left to right). The heating rate is 5 $\mathrm{K\,s^{-1}}$ for all presented spectra.

6.4 Experimental results

6.4.1 TDS from Pt(111)-Cs

TDS spectra from Pt(111)-Cs surfaces with various initial Cs coverages (Fig. 6.1) are characterized by a broad peak whose maximum shifts to lower temperatures with increasing coverage. This behavior was previously associated with the repulsive interactions within the layer and the depolarization effect [5, 16, 74, 96, 103]. At Cs

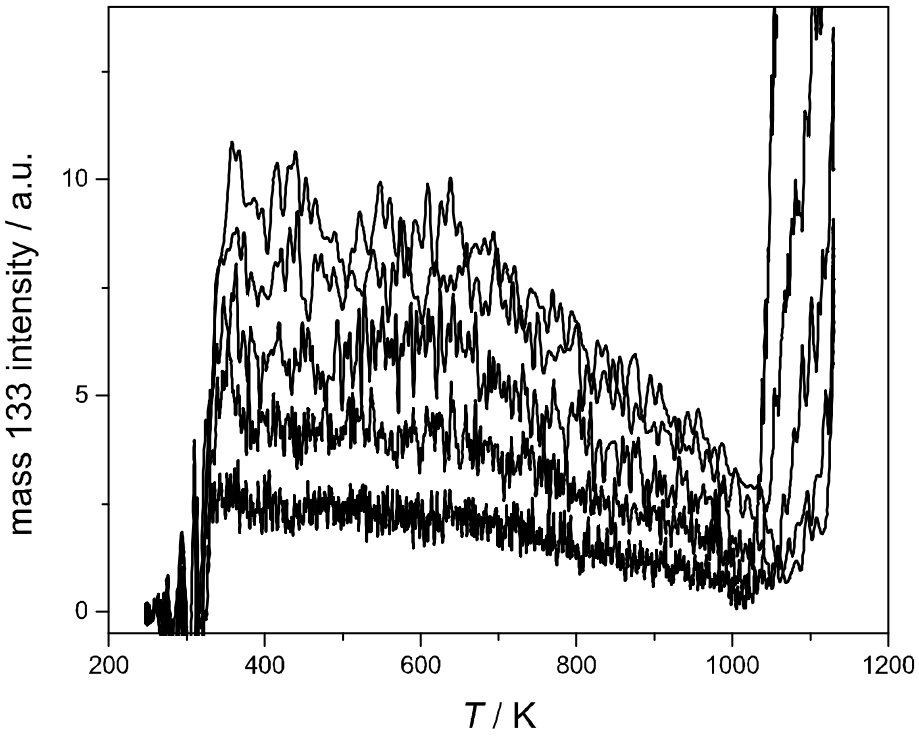

Figure 6.2: Figure shows TDS spectra measured from 1ML Pt(111)-Cs. Temperature ramp rates are 3, 5, 7, 9 and 11 $\mathrm{K\,s^{-1}}$. Low temperature peak from multilayer desorption is subtracted from the spectra.

initial coverages between $0.33-0.41$ ML, a new peak with a maximum at 400 K starts to form. The TDS spectrum from the Cs saturated Pt(111)-Cs layer ($\theta = 0.41$) has a sharp rise at 330 K, followed by a "plateau" and a slow trailing edge from 600 K. This is consistent with the spectra obtained by Garfunkel et al. [5] from Pt(111)-K surfaces, pointing to the same bonding mechanism for Cs and K.

At low coverages ($\theta \leq 0.15$), Cs is adsorbed in an "anomalous" state which is manifested in TDS as a high temperature Cs^+ peak at $T > 1000$ K (Fig. 6.2) [62]. In order to determine the coverage of normally adsorbed Cs more reliably, this peak

is suppressed in Fig. 6.1 by applying a negative voltage to the sample. Therefore, the overall integral of the TDS spectra accounts only for the normally adsorbed Cs, i.e., the presented TDS from full monolayer shows only desorption of 0.26 ML Cs (0.41 − 0.15). Cs coverages in Fig. 6.1 are found from

$$\theta_x = \frac{I_x}{I_{0.41}} \cdot 0.26 + 0.15 \tag{6.3}$$

, where θ_x is coverage corresponding to the integral I_x of spectrum x, $I_{0.41}$ is the integral from the saturated Pt(111)-Cs spectrum and 0.15 is the coverage of the anomalous Cs (signal suppressed in the spectra).

6.4.2 Desorption energy determination

We use two methods to find the desorption energy: Redhead analysis and the method of constant coverages. Redhead analysis (assuming first order desorption and 10^{13} s^{-1} preexponential factor) of the TDS spectra in Fig. 6.1 only roughly estimates $E_d(\theta)$ (Fig. 6.3, blue diamonds).

To find the desorption energy more accurately, we use the method of constant coverages. In this method the crystal is heated using different heating rates which reaches different surface coverages at the same temperature. To make sure that the crystal is fully covered with Cs prior to the desorption, the surface is prepared at low temperature (250 K) allowing multilayer formation. This is an important preparation step, because dosing at room temperature often results in the crystal inhomogeneously covered by Cs. Desorption from multilayer Pt(111)-Cs results in a additional, low-temperature sharp peak at 290 K (not shown). This multilayer peak was fitted by a Gaussian curve and the fit was subtracted from the spectrum.

The TDS from saturated Pt(111)-Cs used for this analysis are in Fig. 6.2. We

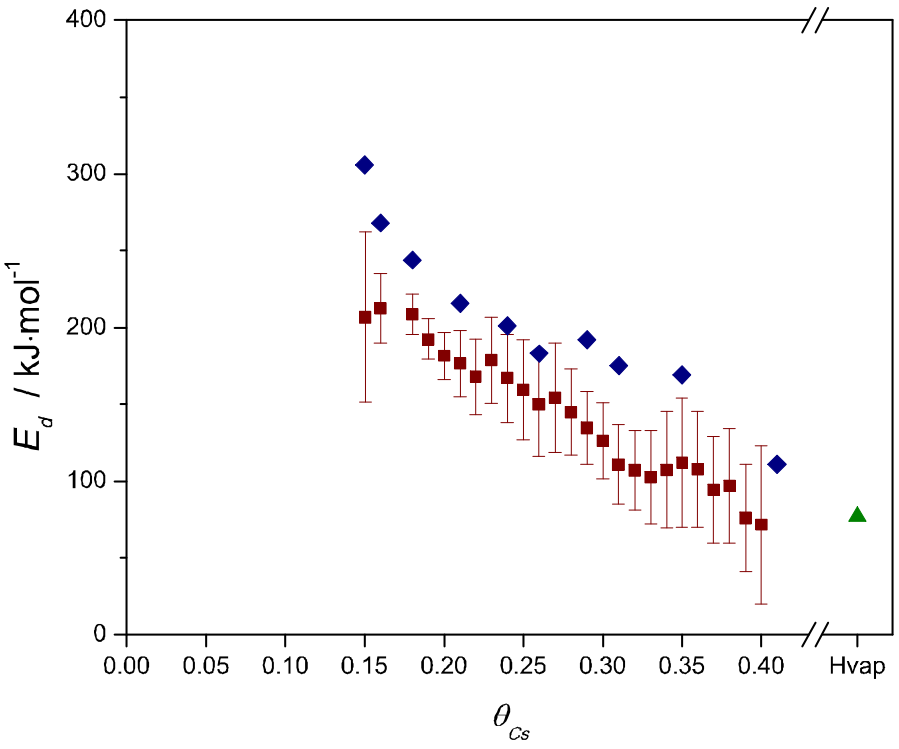

Figure 6.3: Desorption energies $E_{\mathrm{d}}(\theta)$ for different Cs coverages on Pt(111)-Cs. Diamonds (blue) are from rough estimates using Redhead analysis of the spectra in Fig. 6.1. Squares (red) correspond to $E_{\mathrm{d}}(\theta)$ from constant coverage analysis (Fig. 6.2). The vaporization enthalpy, H_{vap}, of solid Cs is shown by the triangle (green).

assume the desorption rate to follow the Arrhenius equation

$$P \propto -s\frac{d\theta}{dT} = k(T)f(\theta)\exp\left(\frac{-E_{\mathrm{d}}(\theta)}{RT}\right) \tag{6.4}$$

where s is the temperature ramp rate, $k(T)$ preexponential factor, $f(\theta)$ is determined by the order of desorption and E_{d} is the desorption energy. The slope of an Arrhenius plot ($\log P$ vs $1/T$) for one particular coverage gives $E_{\mathrm{d}}(\theta)$ for that coverage (Fig. 6.3, red squares) [45], where the coverage was found by integrating the TDS spectra.

Contrary to Fig. 6.1, spectra used in the method of constant coverages were measured without applying a negative potential to the crystal. Therefore, the spectra show the leading edge of the high-temperature anomalous Cs desorption peak at $T > 1000$ K [62].

Both methods (Redhead and constant coverage) to determine $E_{\mathrm{d}}(\theta)$ gave similar results (Fig. 6.3). The overall shape is common for alkali metal adsorption on metallic substrates [5, 74, 104–106]. The decrease of activation energy with coverage can be explained by repulsive lateral interactions within the adsorbed alkali metal layer and the depolarization of Pt-alkali metal bonds [16, 17].

It was proposed by Garfunkel et al. [5], that $E_{\mathrm{d}}(\theta)$ in the case of alkali metal desorption can be rationalized by assuming the activation energy has two terms:

$$E_{\mathrm{d}} \approx H_{\mathrm{vap}} + P(\theta)\ . \tag{6.5}$$

H_{vap} is heat of vaporization of bulk alkali metal and $P(\theta)$ is a polarization term dependent on the coverage with $P(0.41)$ close to zero. In our case, the enthalpy of vaporization of Cs is 77 kJ mol^{-1} [107], which agrees well with the measured E_{d} value at $\theta = 0.41$ (≈ 70 kJ mol^{-1}).

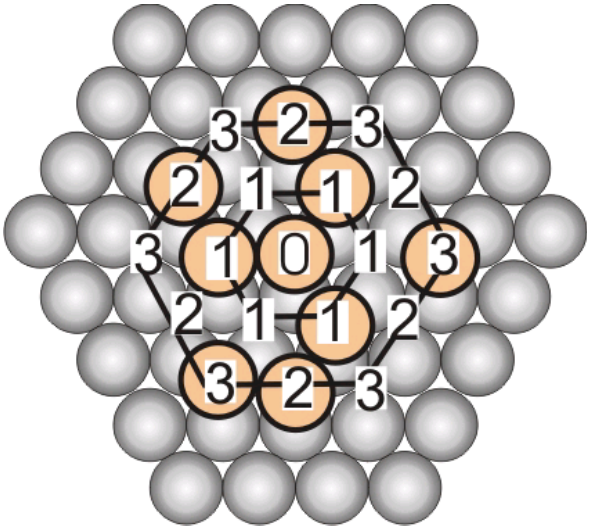

Figure 6.4: The (111) surface representation in MC simulation. The substrate is represented by a triangular grid. Cs atoms are initially randomly distributed on the surface. In order to determine the different adsorption environement that atoms belong to (e.g. atom 0 in the Figure), the neighbours atoms are assigned a number corresponding to a different adsorption shell (1, 2 and 3). Atoms in an adsorption shell 1 are the closest neighbors, atoms in adsorption shell 2 are located further from the desorbing atom and atoms in adsorption shell 3 are the furthest neihgbors considered.

6.5 Model

The (111) surface is represented by a 200×200 rhombic shaped triangular lattice with periodic boundary conditions and a lattice parameter of 2.78 Å (distance between substrate atoms). For the real surface we assume equivalence of hcp and fcc sites and only one kind of site is used in the simulation. Initially, the number of Cs atoms corresponding to $\theta = 0.41$ are randomly distributed at 280 K at the threefold adsorption sites on the surface and the structure is relaxed to thermal equilibrium. The surface temperature is gradually increased and a new surface configuration is calculated at each temperature step. The MC algorithm for each temperature step is:

1. The adsorption environment i for each adsorbed atom is determined depending

on the number of closest neighbors.

2. The desorption energy $E_{\mathrm{d}}^{j,i}$ for all atoms is calculated. An index j runs through all adsorbed atoms on the surface, $j = 1..N$ (N number of adsorbed atoms at each temperature step).

3. The desorption probability of each adsorbed atom is calculated according to

$$\Pi^j = \frac{\Delta T}{s} \cdot k_0 \exp\left(-\frac{E_{\mathrm{d}}^{i,j}}{RT}\right) \tag{6.6}$$

where ΔT is the temperature step (1 K), s is the temperature ramp rate (5 $\mathrm{K\,s^{-1}}$) and k_0 is the preexponential factor (10^{13} $\mathrm{s^{-1}}$).

4. The WF is calculated from the known surface distribution of atoms with different adsorption environments.

5. For each adsorbed atom, a random number $0 < \xi < 1$ is generated. If $\xi < \Pi^j$, the atom is desorbed.

6. The average desorption energy is calculated by averaging the desorption energies of all atoms desorbed in the previous algorithm step.

7. The surface is thermally relaxed.

8. A new coverage is calculated based on the number of desorbed atoms. New temperature $T_{\mathrm{new}} = T_{\mathrm{old}} + \Delta T$ is set.

The surface environment that surrounds a particular adsorbed atom is determined from the number of atoms in the three closest neighbor shells (n_{g}). An arbitrary situation is depicted in Fig. 6.4. Atom 0 is the atom whose adsorption environment we are trying to find. The biggest outer hexagon in Fig. 6.4 shows the shell of maximum distance, where the neighbor atoms are taken into the consideration. There are 12 Pt atoms in that hexagonal cell. The Cs atoms located in the first neighbor shell

(described by symbol 1 in Fig. 6.4) contribute 1 to the total numbers of neighbors because the whole atom is located inside the big hexagon. Atoms from the second shell contribute 1/2 and atoms from the third cell contribute 1/3 as only 1/2 and 1/3 of the atom is located inside the hexagonal cell. For the particular situation in Fig. 6.4, the number of neighboring atoms is $5\frac{1}{6}$. If the number of neighbor atoms $n_{\mathrm{g}} > 3$ ($\theta > 0.33$), then the atom is surrounded by the surface environment with the highest coverage. Similarly, if $n_{\mathrm{g}} > 2$ $(0.25 < \theta \leq 0.33)$, the atom is surrounded by the environment with the second highest coverage and if $n_{\mathrm{g}} \geq 0.8$ $(0.15 < \theta \leq 0.25)$, the atom is surrounded by the environment with the third highest coverage. For $n_{\mathrm{g}} < 0.8$, the atom is surrounded by the surface environment with the lowest coverage. In the following, the limiting coverages for each phase will be denoted as θ_l^i ($\theta_l^{anom} = 0$, $\theta_l^{2\times2} = 0.15$, $\theta_l^{\sqrt{3}\times\sqrt{3}} = 0.25$, $\theta_l^{ihcp} = 0.33$). Using this assignment, atoms on the island boundaries pertain to the structure with the higher coverage.

The model was found to be sensitive to the conditions determining the different adsorption environments. Changes in θ_l^i resulted in worse-fitting curves even when other parameters were varied. The relative heights of the TDS peaks changed, but the peak positions remained the same

The derivation of desorption activation energy, $E_{\mathrm{d}}^{i,j}$, is taken from the "Maschhoff model" of Maschhoff and Cowin [108]. Many current models use the ionic approximation, where the electron is completely transferred from the adsorbed Cs to the substrate and a dipole is formed by the ionized atom and its image charge (Topping model). However, there is strong evidence from DFT calculations that this is not the case for structures with higher alkali metal coverages, where the bond has a mixed metallic-ionic character [109–113]. The dipole moment is caused by a shift of the alkali metal valence electron towards the substrate, but the electron is not completely removed from adsorbed atom. This situation is better described by the Maschhoff model in which both the adsorbate and its image charges are dipoles (Fig. 6.5).

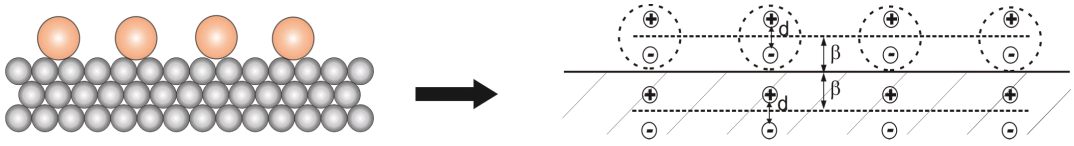

Figure 6.5: The representation of Maschhoff electrostatic model used in $E_{\mathrm{d}}^{\mathrm{j,i}}$ determination. The metal substrate is substituted by the semi-infinite conducting surface. Adsorbed atoms are represented as dipoles which induce an image charge in the substrate.

In our case the Pt substrate is described by a *semi-infinite* metallic surface and the nuclei and valence electrons are replaced by point charges (Fig. 6.5). $E_{\mathrm{d}}^{i,j}(\theta)$ is found from $U_{\mathrm{tot}}^{i}(\theta)$, the total bonding energy of an atom belonging of the surface environment i

$$E_{\mathrm{d}}^{i,j}(\theta) = -\frac{d(\theta U_{\mathrm{tot}}^{i}(\theta))}{d\theta} \ . \tag{6.7}$$

This differential form, also known as adiabatic approximation, takes into consideration the energy change due to the thermal relaxation after desorption [108]. U_{tot}^{i} is approximated by the sum of an electrostatic part ($U_{\mathrm{elec}}^{i}(\theta)$) and a constant "covalent" part (U_{cov}^{i})

$$U_{\mathrm{tot}}^{i}(\theta) = U_{\mathrm{elec}}^{i}(\theta) + U_{\mathrm{cov}}^{i} \ . \tag{6.8}$$

Therefore $E_{\mathrm{d}}^{i,j}$ from Eq. 6.7 can be written as Eq. 6.9.

$$E_{\mathrm{d}}^{i,j} = -\frac{d(\theta U_{\mathrm{elec}}^{i}(\theta))}{d\theta} - U_{\mathrm{cov}}^{i} \tag{6.9}$$

The electrostatic energy of an atom surrounded by the surface environment i depends on the total surface coverage and following Maschhoff [108] is calculated by

$$U_{\mathrm{elec}}^{i}(\theta) = \frac{\left(\mu_0^i\right)^2}{8\pi\varepsilon_0} \cdot \frac{1}{\left(\frac{4\pi}{\sqrt{3}CR_s(\theta)^3}\left(1+\frac{1}{\left[1+\left(\frac{2\beta}{CR_s(\theta)}\right)^2\right]^{3/2}}\right)-\frac{1}{4\beta^3-\beta d^2}\right)^{-1}+\alpha'^i} \tag{6.10}$$

where μ_0^i is adatom dipole moment at zero coverage and infinite distance from the conducting surface (discussed later). α'^i is the effective polarizability volume, $C = 0.658$ is a constant related to the integration limit of dipole summation, and R_s is the nearest-neighbor distance calculated from the surface density

$$R_s(\theta) = \frac{\left(\frac{4}{3}\right)^{0.25}}{\sqrt{n_0\theta}} \ . \tag{6.11}$$

β and d are parameters related to the distance of the adsorbed atom from the metallic surface (Fig. 6.5).

The $E_\mathrm{d}(\theta)$ for the lowest coverage environment is conveniently set to a constant value. This allow us to decrease the calculation time while the high temperature TDS peak can still be fitted to the experimental spectrum. The anomalous peak could be also fitted with $E_\mathrm{d}^{4,j}$ from Eq. 6.7 using a different set of parameters, but this would not change the discussion and conclusions of the paper significantly.

At a given coverage (temperature step), the total WF of the surface is determined as a weighted average of WF of adsorbed atoms surrounded by environment i. First the number of atoms with the same environment is counted and then converted to a surface coverage θ^i ($\theta^i = \frac{N_i}{n_0 A}$, $\theta = \sum_i \theta^i$). A is the area of the 200×200 triangular lattice. The total WF of the surface is calculated by adding the weighted WF of each phase

$$\Delta\phi = \sum_i -\frac{e \cdot n_0 \cdot \mu_{\phi,0}^i}{\varepsilon_0} \cdot \theta^i \ . \tag{6.12}$$

The values of $\mu_{\phi,0}^i$ differs from the μ_0^i used in the TDS simulation.

A simplified relaxation procedure is carried after each MC step. The first step is to randomly choose an occupied and an unoccupied adsorption site. If the number of neighbors of the unoccupied site is less then the number of neighbor of the occupied site ($n_\mathrm{g}^\mathrm{un} < n_\mathrm{g}^\mathrm{o}$) , the adsorbed atom moves from the occupied site to the unoccupied site (second step). These two steps are repeated until no switch is required for 100

occupied-unoccupied pairs in a row. This process aims to distribute the adatoms on the surface by minimizing the number of neighbors (as should be the case for repulsive interactions).

The value of dipole moment at different coverages for different phases is calculated from the expression given by Maschhoff [108]

$$\mu^i(\theta) = \frac{\mu_0^i}{1 + \alpha'^i \left(\frac{4\pi}{\sqrt{3} C R_s(\theta)^3} \left(1 + \frac{1}{\left[1 + \left(\frac{2\beta}{C R_s(\theta)} \right)^2 \right]^{3/2}} \right) - \frac{1}{4\beta^3 - \beta d^2} \right)} \tag{6.13}$$

We use Mersenne Twister random number generator [114] which requires seed at the beginning of each simulation. In order to get more accurate results, we run the same simulation with 100 different seeds and the average is used for TDS, WF and energy plots. The model parameters were found by simple mapping of parameter space.

6.6 Model results

6.6.1 TDS

Adsorption phases coexisting on the surface are described by the same electrostatic model with variable input parameters (Eqs. 6.7-6.10), therefore assigning different sets of parameters to each phase allowed us to distinguish quantitatively between the phases and find common trends in substituted parameters.

The simulated TDS spectra for initial Cs coverages of 0.41, 0.33 and 0.25, scaled to match the height of the experimental curve, are shown in Fig. 6.6. The correlation with the experimental TDS for all three initial coverages is reasonably good. The spectrum from the Cs saturated surface ($\theta_{\mathrm{Cs}} = 0.41$) clearly shows the plateau at low

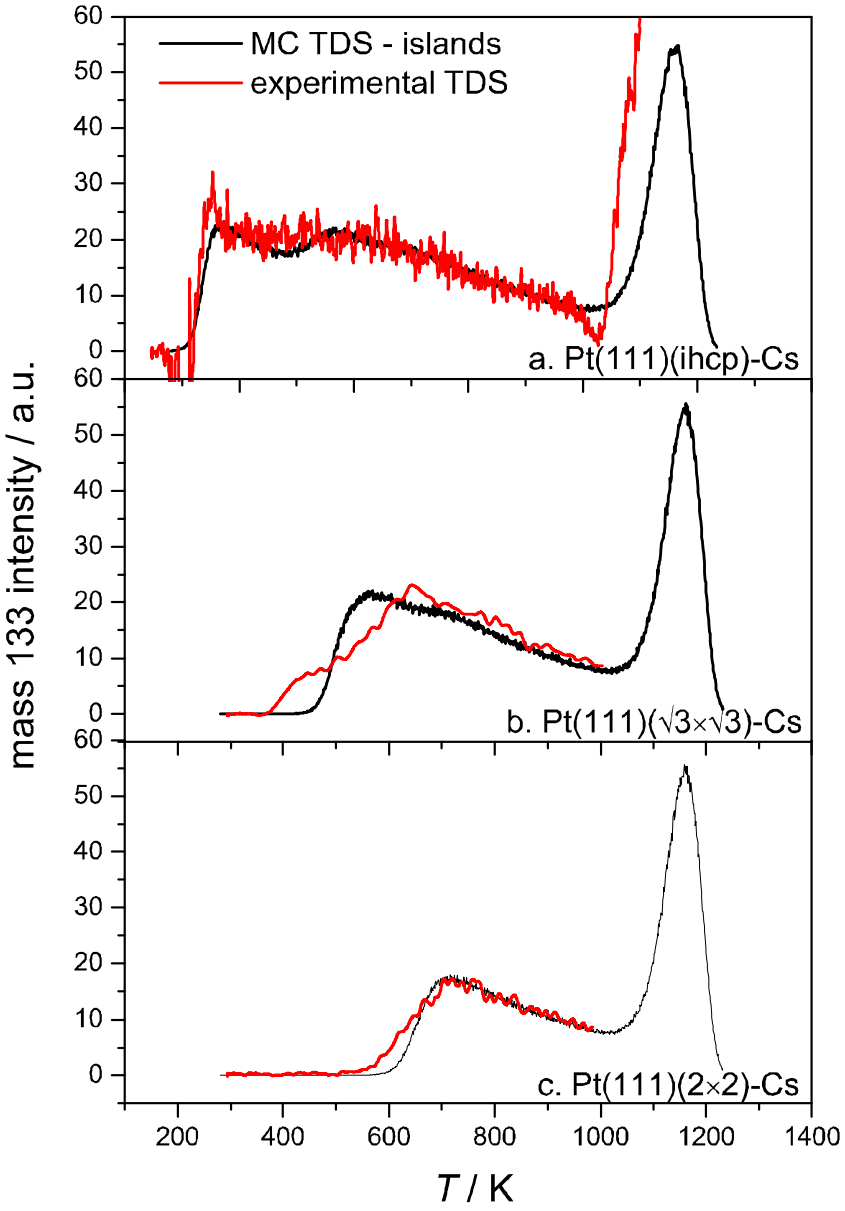

Figure 6.6: Simulated TDS spectra from Pt($ihcp$)-Cs (a., $\theta^{ihcp} = 0.41$), Pt(111)($\sqrt{3} \times \sqrt{3}$)-Cs (b., $\theta^{\sqrt{3}\times\sqrt{3}} = 0.33$) and Pt(111)(2 × 2)-Cs (c., $\theta^{2\times2} = 0.25$). The corresponding model parameters are $\{E_{\mathrm{cov}}^{ihcp} = -410\ \mathrm{kJ\,mol^{-1}}$, $\alpha'^{ihcp} = 4.5 \cdot 10^{-30}\ \mathrm{m^3}$, $\mu_0^{ihcp} = 2.6{\cdot}10^{-29}\ \mathrm{C\,m}\}$, $\{E_{\mathrm{cov}}^{\sqrt{3}\times\sqrt{3}} = -365\ \mathrm{kJ\,mol^{-1}}$, $\alpha'^{\sqrt{3}\times\sqrt{3}} = 6{\cdot}10^{-30}\ \mathrm{m^3}$, $\mu_0^{\sqrt{3}\times\sqrt{3}} = 2.5{\cdot}10^{-29}\ \mathrm{C\,m}\}$, $\{E_{\mathrm{cov}}^{2\times2} = -360\ \mathrm{kJ\,mol^{-1}}$, $\alpha'^{2\times2} = 7{\cdot}10^{-30}\ \mathrm{m^3}$, $\mu_0^{2\times2} = 2.5{\cdot}10^{-29}\ \mathrm{C\,m}\}$, $\{E_{\mathrm{cov}}^{anom} = -308\ \mathrm{kJ\,mol^{-1}}\}$, $d = 1.1 \cdot 10^{-10}$ m, $\beta = 1.8 \cdot 10^{-10}$ m. The modeled high temperature desorption peak of anomalous Cs does not reflect different ionization cross sections for neutral Cs and Cs^+ ion [62], but shows the correct peak position.

desorption temperatures, which consists of the two overlapping TDS peaks originated from the Pt(111)($\sqrt{3} \times \sqrt{3}$)-Cs and Pt(111)(*ihcp*)-Cs surface structures.

The main parameters used in the MC simulation are μ_0 and α'. The α' describes the influence of the electrostatic field induced by adsorbed atoms on the dipole moment and μ_0 is a hypothetical dipole moment of a Cs atom far from the surface. There is a common peak behavior related to those parameters observed for all surface phases. As the value of μ_0^i increases and the value of α'^i decreases, the peak maximum corresponding to surface phase i shifts to a lower temperature and the peak has a longer and less steep trailing edge. We found that the following conditions must satisfied in order to obtain the correct TDS spectra: $\mu_0^{ihcp} > \mu_0^{\sqrt{3}\times\sqrt{3}} > \mu_0^{2\times2}$ and $\alpha'^{ihcp} < \alpha'^{\sqrt{3}\times\sqrt{3}} < \alpha'^{2\times2}$. This way the overlapping TDS peaks from *ihcp* and $\sqrt{3}\times\sqrt{3}$ phase forming the low temperature "plateau" have the right shape with the slowly decreasing trailing edge.

The comparison of calculated $-\frac{d(\theta U^i_{\mathrm{elec}}(\theta))}{d\theta}$ (the electrostatic part of $E^i_{\mathrm{d}}(\theta)$) shows the reason for the trend in μ_0 and α' (Fig. 6.7). In order to sustain an almost linear character of $E_{\mathrm{d}}(\theta)$ at high coverages, each subsequent surface structure must have higher μ_0 and lower α'. For example μ_0 and α' for the (2×2) structure would not be sufficient to fit the experimental $E_{\mathrm{d}}(\theta)$ over the whole temperature range because the slope of $-\frac{d(\theta U^{2\times2}_{\mathrm{elec}}(\theta))}{d\theta}$ at high coverages is close to 0.

Changing the d and β parameters has a similar effect as varying U_{cov}, μ_0 and α'. This is expected at least for d because the dipole moment is defined as $q{\cdot}d$ (q is a charge of the dipole) and a change in d will result in a change of μ_0. For the sake of simplicity we keep d and β constant for all phases and the differences between the phases are described only by U_{cov}, μ_0 and α. It should be noted, however, that the change in $\beta(z)$ is expected on the real surface, because as the ionic character of alkali metal-substrate bond decreases with increasing coverage, the alkali metal size increases and the alkali metal atoms move slightly away from the surface [49, 109, 112, 113]. In this regard, numerical values of U_{cov}, μ_0 and α' parameters are less important than their

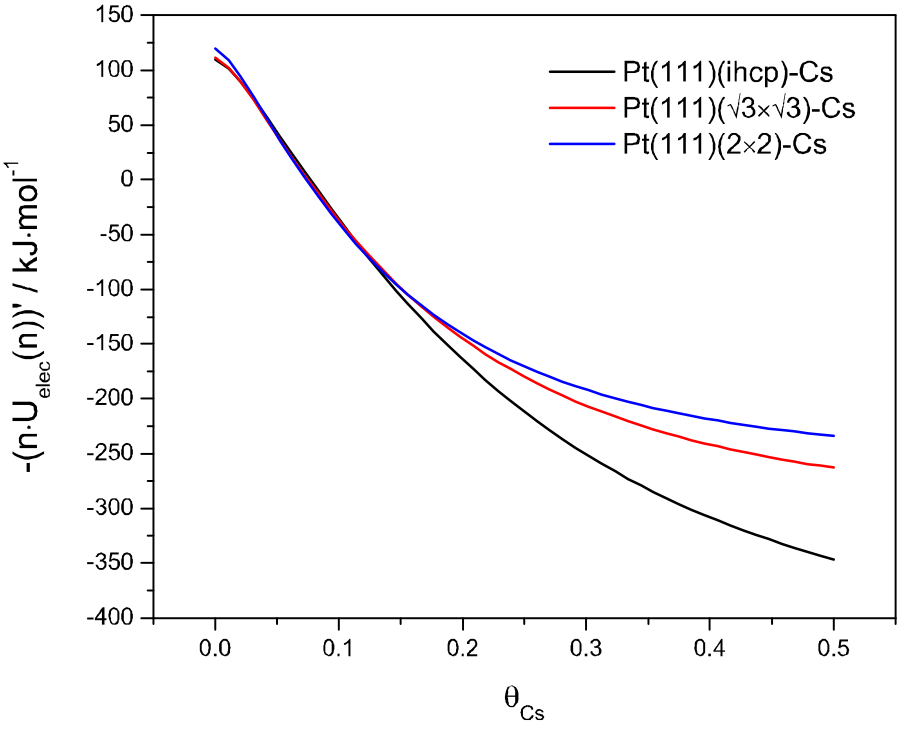

Figure 6.7: Calculated $-\frac{d(\theta U^i_{\rm elec}(\theta))}{d\theta}$ (Eq. 6.10) using the parameters from MC simulation for Pt(111)(*ihcp*)-Cs (black curve), Pt(111)($\sqrt{3} \times \sqrt{3}$)-Cs (red curve) and Pt(111)(2×2)-Cs (blue curve).

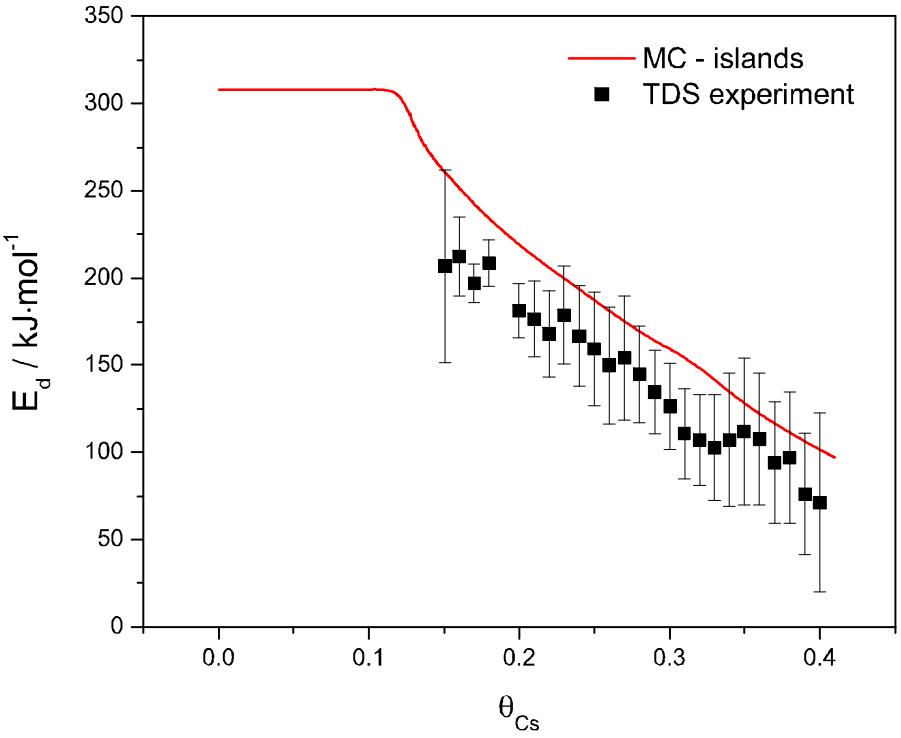

Figure 6.8: Calculated desorption energies $E_{\mathrm{d}}^{i}(\theta)$ (red curve). Black squares show the measured values from TDS experiments.

trends because we do not have enough information about how the d and β parameters affect the overall fit. Some of the parameters (β, μ_0) could be possibly obtained from a first principles calculation. It is also reasonable to expect the preexponential factor k to change with coverage [96, 115].

Fig. 6.8 shows activation energies of desorption, $E_{\mathrm{d}}(\theta)$, calculated using our MC model. The simulated curve reasonably follows, within the error, the experimentally determined E_{d} (black squares). For $\theta < 0.12$, the desorption energy is constant as defined in our MC simulation for anomalously adsorbed Cs.

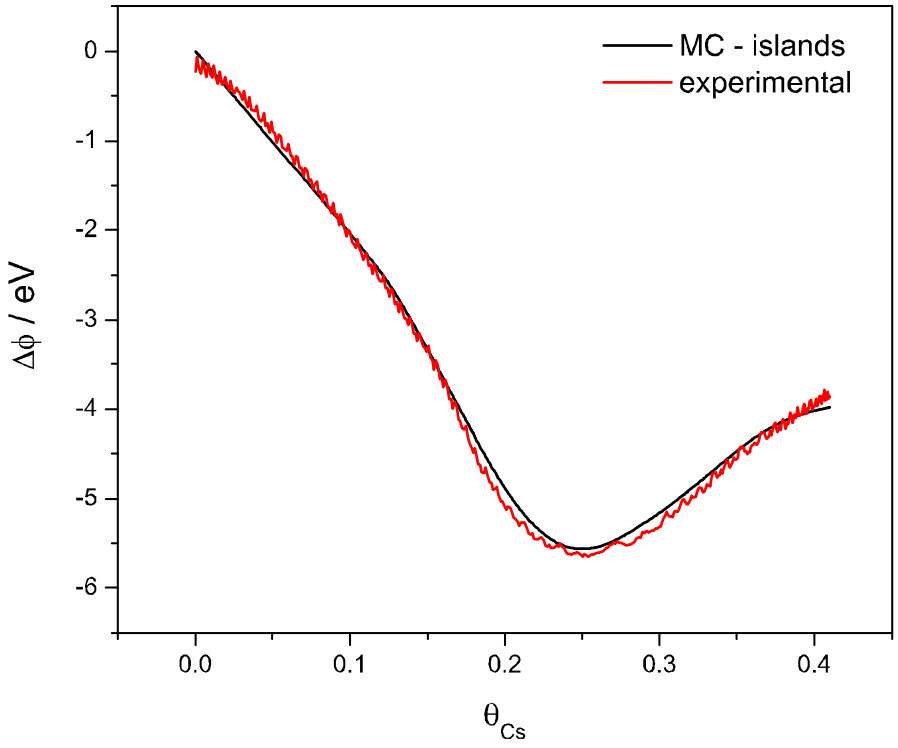

Figure 6.9: WF response ($\Delta\phi$) during the MC desorption simulation (black curve, $\mu_{\phi,0}^{ihcp} = 0.56$ C m, $\mu_{\phi,0}^{\sqrt{3}\times\sqrt{3}} = 0.90$ C m, $\mu_{\phi,0}^{2\times2} = 1.70$ C m, $\mu_{\phi,0}^{anom} = 1.20$ C m). The red curve shows the experimental WF change while the Cs is adsorbed on the surface.

6.6.2 Work Function

For a WF simulation (Fig. 6.9), we use only a simple expression (Eq. 6.12) to show the striking fact, that no depolarization is needed to explain the WF curve. At a given coverage (temperature step in MC simulation), each atom on the surface is assigned fixed $\mu_{\phi,0}^{i}$ depending on the adsorption phase i the atom belongs to. The WF of the whole surface is then found as a weighted average of $\mu_{\phi,0}^{i}$, depending on the relative numbers of adsorbates in each phase i (Eq. 6.12). Therefore the WF is determined by the amount of surface covered by each structure. As the Cs coverage

increases, the fraction of surface covered by the different phases changes and the WF of the surface changes as well.

The modeled curve matches almost perfectly the measured WF. A similar result can also be obtained with a more complicated expression involving depolarization terms α', but only it shows a slight improvement of the fit. This highlights the fact that depolarization does not need to be included in the modeling of the WF but an plays an essential role during the desorption.

6.6.3 Parameters comparison

In order to compare parameters used in the TDS simulation with literature values and $\mu^i_{\phi,0}$ from WF fit, dipole moments of atoms in close proximity to the surface are calculated for each adsorption phase as a function of the total coverage (Eq. 6.13, Fig. 6.10). The parameters μ^i_0 fitted in MC TDS simulation (Eq. 6.10) describe the hypothetical dipole moment of a Cs atom in a free space (away from the surface) and in the limit of zero coverage. When atoms are located close to the metallic surface, however, they are in the field of its image charges and the dipole moment, even at zero coverage, differ from μ^i_0.

Fig. 6.10 shows the dipole moments of adsorbed atoms for each adsorption structure as a function of coverage. Interestingly, the surface structure with the highest dipole moment at zero coverage is Pt(111)(2×2)-Cs, even though it has the lowest μ^i_0. This is caused by the highest Cs polarizability volume α' of Pt(111)(2×2)-Cs because as the value of α' increases, the field induced by the image charge close to the surface has a stronger effect on the resulting dipole moment.

According to Fig. 6.10, the dipole moments determined from the TDS simulation for the surfaces fully covered by one structure are $\mu^{2\times2} = 1.95 \cdot 10^{-29}$ C m ($\theta = 0.25$), $\mu^{\sqrt{3}\times\sqrt{3}} = 1.68 \cdot 10^{-29}$ C m ($\theta = 0.33$) and $\mu^{ihcp} = 1.67 \cdot 10^{-29}$ C m ($\theta = 0.41$). This resulting trend agrees well with the trend observed in DFT calculations of Na and

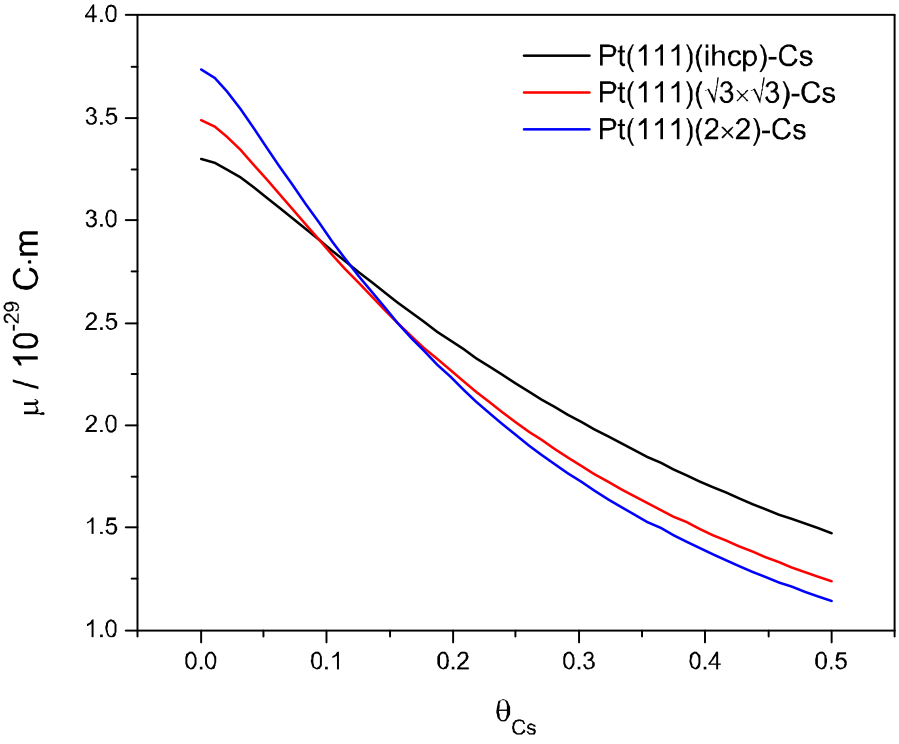

Figure 6.10: Calculated dipole moments $\mu(\theta)$ for different adsorption phases.

K adsorption on Rh(111) [113] and in the Langmuir-Gurney model for alkali metal adsorption on metallic surfaces [8, 9, 11]. In both cases, adsorbed atoms were found to be more polarized with a higher dipole moment on the surface with lower alkali metal coverage than on the surface with higher coverage.

Despite the favorable trend, the values from the TDS simulation are significantly different than the values obtained from the WF simulation ($\mu_{\phi,0}^{anom} = 1.20$ C m, $\mu_{\phi,0}^{2\times2} = 1.70$ C m, $\mu_{\phi,0}^{\sqrt{3}\times\sqrt{3}} = 0.90$ C m, $\mu_{\phi,0}^{ihcp} = 0.56$ C m). The same disrepancy between the dipole moments obtained from fitting the WF and TDS experimental data with the same electrostatic model was observed before [16,96]. It was noted, that this could be due to the coverage dependence of the preexponential factor k [96]. However, other factors such as non-electrostatic long range interactions can also play a role. Long range interactions mediated by the substrate have been suggested by Yamada et al. for Cs on Pt(111) [34]. These could be incorporated in our model by allowing $U_{\rm cov}$ to be a function of coverage while substituting the values of $\mu_{\phi,0}$ obtained from the WF fit. Unfortunately, this would not likely result in a better understanding of the adsorption/desorption behavior due to the unknown nature of $U_{\rm cov}(\theta)$.

6.7 Discussion

The MC model has a few key assumptions. First, we use the experimentally observed saturation coverages for each phase for θ_l^i. We found during the study that the model was sensitive to θ_l^i values and using other than the experimental values resulted in a worse agreement with the experimental TDS spectra even though other parameters were varied.

Second, we compare the experimental WF curve obtained during the adsorption and the calculated WF during the modeled desorption. The assumption is that the phase distribution on the surface is the same for all temperatures for the given coverage and does not depend on the history of the surface, i.e. the work function response

is exactly the same during adsorption and desorption.

6.7.1 Comparison of models

In this section, we will relate our model to existing models and will discuss the differences, strengths and weaknesses of our approach.

Thermal desorption

The most popular approach for modeling TDS spectra of polar molecules or alkali metal atoms adsorbed on a metallic substrate is based on a calculation of desorption energy from repulsive electrostatic interaction using Eqs. 6.7-6.8 [16, 96]. The expression for U^i_{elec} differs in each model but in both cases the surface is approximated by one surface structure with only one set of parameters and the desorption energy depends exclusively on a global coverage or a lattice parameter. Even though this approach can explain some of the experimental TDS features (slow trailing edge at high temperatures), the fine features (e.g., the low temperature "plateau") cannot be duplicated [96]. We find that the incorporation of experimentally observed island growth in our model significantly improves the accuracy of the fit.

In contrast to the classic approach, the Monte Carlo simulation used by Uñac et al. [17] emphasize the short range interactions with closest neighbors. For each atom adsorbed on a surface at a given temperature step, the desorption energy E_{d} is calculated using interactions with up to third order neighbors and the contributions from farther atoms are neglected. The depolarization effect is incorporated into the model as an attenuation function (fitting parameter) dependent on the global coverage. The calculated $E_{\text{d}}(\theta)$ is obtained from the simulated TDS spectra as a model output and is used to determine μ and α by least squares fit to the Topping model. The determined parameters are further utilized to calculate theoretical WF curve using Helmholtz and Topping formula.

We also calculated the electrostatic interaction energy based on the occupational numbers n_{g} in close proximity of evaluated atom. We deployed the same algorithm as Uñac et al., but instead of using an attenuation parameter $\varphi(\theta)$ and constant interaction energies as a fitting parameters, we defined the interaction energies with the closest neighbors according to the Maschhoff electrostatic model [108]. For each neighboring shell, the interaction energy had a discrete value calculated from the electrostatic model and the contribution from atoms beyond third neighbor shell was calculated using the mean field approximation. The modeled TDS spectra were identical to the spectra calculated using just the mean field approximation for all neighboring shells. In both cases we found that we need to include the depolarization and three different sets of parameters for each surface structure in order to simulate properly the desorption spectrum.

The Uñac et al. approach has one significant drawback. Even though it seems to accurately describe the interaction energy with the closest neighbors, the desorption energy refers to the sudden desorption limit [108] and does not incorporate surface relaxation after desorption. It is in contrast to the formula used in Eq. 6.8, where the relaxation of the surface is accommodated by the first derivative of $U^{i}_{\mathrm{elec}}(\theta)$. In order to calculate the desorption energy in adiabatic approximation using the interactions with closest neighbors, the first derivation of $U^{i}_{\mathrm{tot}}(\theta)$ needs to be evaluated. This evaluation is not possible in Uñac's case because the exact adsorbate distribution on the surface must be known for two subsequent temperature steps to find out the change in occupation numbers $n_{\mathrm{g},1}$, $n_{\mathrm{g},2}$, $n_{\mathrm{g},3}$.

We feel that the mean field approximation is sufficient to describe the adsorbate-adsorbate interactions on the surface. In our view, the observed TDS and WF behavior is a result of coexistence of various adsorption phases on the surface rather than the exact spatial correlations of adsorbed atoms as suggested by Uñac et al. We also chose the presented mean field approximation because we believe that in our case the inclusion of the adiabatic desorption limit is more important than exact description

of the electrostatic interactions with the closest neighbors. Those interactions are averaged anyway in the calculation of average desorption energy for each temperature step (section 6.5). The importance of the adiabatic desorption limit is discussed in Ref. 108.

Work function

Larger deviation between the theoretical predictions of various models and experimental results can be seen for WF change. The classical Topping formula (Eq. 6.1) fails to describe the observed WF increase at high alkali metal coverages [13–15]. Two different solutions are provided in the literature: (i) introduction of the depolarization as a function of coverage [13] or (ii) the adsorbed species are divided into gas-like adsorbates and adsorbates embedded in islands and the WF is related to the fraction of surface covered by islands [98]. The second approach is similar to our model with the exception that only two surface phases are considered in the literature.

We checked the first approach by setting $\alpha'(\theta)$ as a linear function with $\alpha'(0) = 3\times10^{30}$ m^3 and $\alpha'(0.41) = 37\times10^{-30}$ m^3 and using only one set of parameters during a MC simulation. The linear approximation of α' fits well to the $\alpha'(\theta)$ function proposed by Verhoef and Assher [13]. We succeeded in duplicating the results for WF, but this approach failed to match the experimental TDS and $E_\mathrm{d}(\theta)$ (results not shown). The $E_\mathrm{d}(\theta)$ showed a minimum with a rising trend for high Cs coverage, which is inconsistent with the decreasing desorption energy trend obtained in our experiments.

The rising trend of $\alpha'(\theta)$ proposed by Verhoef and Assher is opposite to the trend found in our MC simulation. We found that $\alpha'^{ihcp} < \alpha'^{\sqrt{3}\times\sqrt{3}} < \alpha'^{2\times2}$ (decreasing trend) must be maintained in order to successfully reproduce the TDS data. Verhoef and Assher justified their finding by comparing the calculated $\alpha'(\theta)$ to the α' of alkali metal cations and neutral atoms. Because at low coverages the bond between

alkali metal and substrate has more ionic character, the α' is close to the low α' value of alkali metal cations in a 3D ionic crystal. As the coverage increases, the Pt-Cs bond becomes more depolarized and adsorbate atoms become more neutral. The polarizability shifts towards the higher value of neutral alkali metal atom in gas phase. Our inability to model the TDS spectra with the $\alpha'(\theta)$ trend proposed by Verhoef and Assher points to the fact that the polarizability of the alkali metal on the surface might not be simply related to the polarizability of the neutral gas phase atom or positively charged ion.

6.8 Conclusions

We have shown that the adsorption/desorption behavior of Cs on a metallic surface is mainly governed by the phase distribution on the surface. Both work function and TDS data are best fit by including the postulated island formation into the model. According to our MC simulation, the depolarization of the Cs-Pt bond plays a significant role in explaining the observed TDS spectra. However, contrary to other models, we find that the effect of depolarization does not need to be included when modeling the overall work function behavior of the surface. For the first time, a model is able to explain both TDS and WF data for alkali metal adsorbed on a Pt(111) surface in unprecedented detail.

6.9 Acknowledgements

This work was financially supported by the Natural Sciences and Engineering Research Council (NSERC) of Canada.

Chapter 7

Conclusions

In the third chapter we showed that an anomalous adsorption state of Cs exists on Pt(111) at low Cs coverages. The phase transition between anomalously adsorbed Cs and normally adsorbed Cs is detected as the change in the slope of the WF curve. Cs adsorbed in the anomalous state desorbs in the high temperature TDS peak (> 1000 K) as a positive ion. When using a TDS lock-in detection technique, Cs^+ desorption results in a TDS signal phase shifted by $180\,^\circ$ when compared to the signal from a neutral Cs. Therefore using the lock-in technique allows us to distinguish the desorption of positively charged and neutral atoms in one TDS experiment.

We found that the anomalously adsorbed Cs shows catalytic activity towards oxygen adsorption. The maximum oxygen coverage on Pt(111)(*anom*)-Cs surface is significantly increased when compared to the bare Pt(111). This effect may have consequences in heterogenous catalysis that involves breakage of the O_2 bond. Anomalously adsorbed Cs may lower the activation barrier for O_2 dissociation, and yet the Cs-O interaction appears to be weak enough that subsequent reaction of adsorbed O with other species would not be inhibited. Furthermore the Cs is not easily removed from the surface. Therefore Pt(111)(*anom*)-Cs seems to be a good model catalyst for further investigation.

Iodine adsorption on Pt(111)(*anom*)-Cs to saturation results in an ordered structure with a $(\sqrt{7} \times \sqrt{7})R19.1°$ LEED pattern. The LEED pattern is the same as for the saturated Pt(111)$(\sqrt{7} \times \sqrt{7})R19.1°$-I layer. Therefore we propose that the iodine interactions with the surface determine the resulting structure and the Cs interactions play only a minor role. When the Pt(111)$(\sqrt{7} \times \sqrt{7})R19.1°$-Cs,I surface is heated, the Cs desorbs together with I in the sharp peak at 560 K as a Cs_xI_y $(x/y \geq 1)$ cluster.

The preparation and study of Pt(111)-Cs,I layers with $\theta_{Cs} > 0.15$ was carried out. When I_2 is adsorbed on Pt(111)(*ihcp*)-Cs, the WF increases and the resulting structure depends on the amount of I on the surface. A new (4×4) LEED pattern appears at $\Delta\phi \approx 1 - 1.5$ eV during the I_2 dosing, . This LEED pattern was assigned a planar Pt(111)(4×4)-Cs_2I structure with p6m symmetry. Further I_2 dosing to saturation results in a formation of Pt(111)$(\sqrt{7} \times \sqrt{7})R19.1°$-Cs,I surface structure with a $\left(\sqrt{7} \times \sqrt{7}\right)$ LEED pattern. In this bi-layer structure, I atoms are located close to the surface and Cs atoms are above the I layer. When the dosing order is reversed and the Cs is dosed on the Pt(111)$(\sqrt{7} \times \sqrt{7})R19.1°$-I surface, the WF decreases and the final structure has the (*ihcp*) LEED pattern. The TDS from all mixed Cs,I layers shows a sharp peak around 600 K suggesting the Cs_xI_y cluster desorption.

In order to correlate our experimental results with structures predicted for 2D ionic crystals, we performed simple electrostatic energy calculations for various surface geometries. We found that both the planar Pt(111)(4×4)-Cs_2I structure and the bilayer Pt(111)$(\sqrt{7} \times \sqrt{7})R19.1°$-Cs,I can be rationalized from electrostatic principles and are consistent with ionic structures.

Experimental results on Cs,O led to a better understanding of their structure and formation on Pt(111). We found four main oxygen adsorption states: α, β, γ-atomic and γ-molecular. During the oxygen dosing on the Pt(111)(*ihcp*)-Cs, oxygen is first adsorbed to a site located below Cs (γ-atomic site) and causes the initial work function decrease. As the O coverage increases, oxygen starts to adsorb in a different adsorption state (γ-molecular). When desorbing, γ-molecular oxygen leaves

the surface as the O_2 molecule and γ-atomic oxygen leaves the surface in its atomic form. The γ-molecular oxygen TDS peak overlaps with the Cs TDS peak and therefore we conclude that the γ-molecular oxygen closely interacts with Cs. The oxygen in both γ states is responsible for the thermal stabilization of Cs on the surface.

After both γ states are occupied, oxygen starts to adsorb in the β adsorption state. This oxygen is not as strongly bound to Cs as the γ oxygen, but some interaction exists as seen from the increased ordering of the layer and the sharper (4×4) LEED pattern. The (4×4) LEED pattern was assigned to an arrangement where oxygen is located in the center of Cs hexagons.

The observed (4×4) LEED pattern is the same as for the Pt(111)(4×4)-Cs_2I surface, pointing to the similarity in bonding between Cs-O and Cs-I. Given the large electronegativity of both O and I and the low electronegativity of Cs, this finding is not surprising. Both layers are expected to show ionic bonding character which results in the similar observed structures.

We suggest the following behavior for I_2 adsorption on Pt(111)-Cs,O. Because I interacts more strongly with Cs than O, oxygen in the Cs,O layer is replaced by I. The resulting surface consists of Cs,I islands with oxygen adsorbed in between these islands. Upon heating the surface, oxygen desorbs independently of the Cs,I islands.

An explanation of the observed WF curves and TDS spectra for Pt(111)-Cs surfaces has been given in terms of theoretical model. This MC model for the first time incorporates observed island formation. We found that the phase distribution on the surface is responsible for the observed characteristic WF curve with a minimum corresponding to the Pt(111)(2×2)-Cs structure. The inclusion of various phases also explained the observed low temperature "plateau" in TDS spectra.

According to our MC simulation, the depolarization of the Cs-Pt bond plays a significant role in explaining the observed TDS spectra. However, contrary to other models, we find that the effect of depolarization does not to be included in our model

in order to fit the overall work function behavior of the surface. For the first time, a similar model is able to explain both TDS and WF data in unprecedented detail.

This study demonstrates that Cs is indeed a good model catalyst to investigate, especially due to its ability to dissociate oxygen molecules. The high thermal stability and relative simplicity of Pt(111)(*anom*)-Cs could be used to explore new catalytic layers. The next step would be to incorporate the properties of the Pt(111)(*anom*)-Cs surface into practical applications. This would include the study of stability and behavior of Pt(111)(*anom*)-Cs under catalytic conditions and in an aqueous environment. Density Functional theory (DFT) calculations can be used to find the cause of such special behavior by examining the change in electronic properties of the surface when compared to the bare Pt and higher coverage Pt(111)-Cs surfaces.

The coadsorption experiments were aimed at revealing the structural behavior of bimetallic layers and their relation to bonding. Studying layers composed of highly electropositive Cs and electronegative I and O helped to understand the formation and structure of ionic layers. Our results support the predictions of coplanar hexagonal structures, however, some unexpected behavior was observed for Pt(111)-Cs,I layers with high I coverage. Namely, the layer seems to form a bi-layered structure even though the bond is expected to be ionic. Clearly, more systems need to be studied before general predictions of layer structure based on observed bonding (or vice versa) can be made, but we believe our studies are an important contribution toward this goal.

Appendix A

Equivalence of energy and work for charges above a metal surface

We will show, that the equation (Eq. 3.1) to calculate the electrostatic energy of the ionic layer is consistent with another approach, where the energy of the layer is calculated from the work needed to disassemble the layer.

The model situation for a mixed layer with three real charges is depicted in Fig. A.1. d is the charge distance from the surface and u is the distance between charges. The total electrostatic energy is calculated as a sum of electrostatic energies of each charge and its image charge using

$$E = \frac{\sum_{i=1}^{6} E_i}{2 \cdot 2} \tag{A.1}$$

$$E_i = \frac{q_i}{4\pi\varepsilon_0} \cdot \sum_{h} \sum_{l=0}^{1} \frac{q_{hl}}{|r_{hl}|} - \frac{q_i}{4\pi\varepsilon_0} \cdot \frac{1}{2d} \tag{A.2}$$

The index h sums all real charges excluding the ith charge, and the index l distinguishes between a real charge and an image charge at the h position. The $2 \cdot 2$ denominator is related to a double counting of interactions and the fact that the field only exists above the metallic surface, therefore, only taking up half of the space.

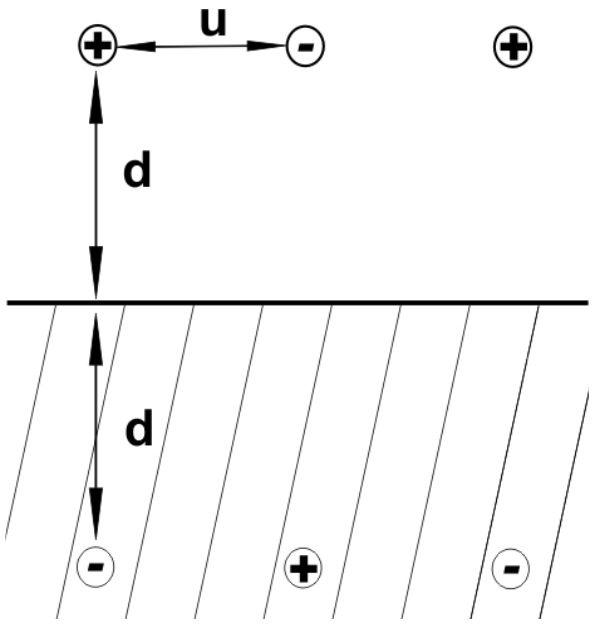

Figure A.1: The setup for electrostatic energy calculation of three charges close to the metallic surface.

The second approach to determine the electrostatic energy of an ionic layer involves the calculation of work done when charges are removed from their positions one by one. The work to remove the first charge is denoted W_1, the second charge W_2 and the third charge W_3. The electric field in the z direction when the first charge is being removed is denoted F_1. Similarly, the electric field when the second charge is being removed is F_2 and the field when the last charge is being removed is F_3. The work W_x $(x = 1, 2, 3)$ is calculated as

$$W_x = \int_d^\infty F_x(z)dz \tag{A.3}$$

. The total work done by taking the layer apart is

$$W = \sum_{x=1}^{3} W_x \tag{A.4}$$

. If Eq. A.1 is correct, $E - W = 0$.

In our particular case of three charges, the electrostatic energy E calculated from Eq. A.1 is

$$\begin{aligned} E &= k\left(4\cdot\left(-\frac{1}{2d}-\frac{1}{u}+\frac{1}{\sqrt{u^2+(2d)^2}}+\frac{1}{2u}-\frac{1}{\sqrt{(2u)^2+(2d)^2}}\right)+\right. \\ &\quad \left. 2\cdot\left(-\frac{1}{2d}-\frac{2}{u}+\frac{2}{\sqrt{u^2+(2d)^2}}\right)\right) \\ &= \frac{4}{k}\left(-\frac{3}{d}-\frac{6}{u}+\frac{8}{\sqrt{u^2+4d^2}}-\frac{2}{\sqrt{u^2+d^2}}\right) \end{aligned} \tag{A.5}$$

$$k = \frac{1}{4\pi\varepsilon_0} \tag{A.6}$$

To calculate W_1, we have to first find the field which acts on the desorbing charge. (F_1).

$$\begin{aligned} F_1 &= k\left(-\frac{1}{(2z)^2}+\frac{d+z}{\sqrt{(d+z)^2+u^2}}\cdot\frac{1}{(z+d)^2+u^2}-\right. \\ &\quad \frac{z-d}{\sqrt{(z-d)^2+u^2}}\cdot\frac{1}{(z-d)^2+u^2}- \\ &\quad \frac{d+z}{\sqrt{(d+z)^2+(2u)^2}}\cdot\frac{1}{(z+d)^2+(2u)^2}+ \\ &\quad \left.\frac{z-d}{\sqrt{(z-d)^2+(2u)^2}}\cdot\frac{1}{(z-d)^2+(2u)^2}\right) \end{aligned} \tag{A.7}$$

z is the distance from the surface in the direction perpendicular to the surface. The $-\frac{1}{(2z)^2}$ term is the field induced by the image charge of the desorbing charge. The

work done to remove the first charge in the field F_1 is

$$\begin{aligned} W_1 &= \int_d^\infty F_1(z)dz \qquad (A.8) \\ &= -\frac{k}{4}\cdot\left(\frac{\sqrt{u^2+4d^2}u\sqrt{u^2+d^2}+2\sqrt{u^2+4d^2}ud}{\sqrt{u^2+4d^2}u\sqrt{u^2+d^2}d}+\right. \\ &\quad \left.\frac{2\sqrt{u^2+4d^2}\sqrt{u^2+d^2}d-4u\sqrt{u^2+d^2}d}{\sqrt{u^2+4d^2}u\sqrt{u^2+d^2}d}\right) \end{aligned}$$

Once the first charge is completely removed, the field acting on the second desorbing charge (F_2) is

$$F_2 = k\left(-\frac{1}{(2z)^2}+\frac{d+z}{\sqrt{(d+z)^2+u^2}}\cdot\frac{1}{(z+d)^2+u^2}-\frac{z-d}{\sqrt{(z-d)^2+u^2}}\cdot\frac{1}{(z-d)^2+u^2}\right) \qquad (A.9)$$

Similarly

$$\begin{aligned} W_2 &= \int_d^\infty F_2(z)dz \qquad (A.10) \\ &= -\frac{k}{4}\cdot\frac{(\sqrt{u^2+4d^2}u+4\sqrt{u^2+4d^2}d-4ud)}{\sqrt{u^2+4d^2}ud} \end{aligned}$$

For the last charge,

$$F_3 = -\frac{1}{4}\cdot\frac{k}{z^2} \qquad (A.11)$$

$$W_3 = \int_d^\infty F_3(z)dz = -\frac{1}{4}\cdot\frac{k}{d} \qquad (A.12)$$

Total work done to disassemble the layer is

$$\begin{aligned} W &= W_1 + W_2 + W_3 \\ &= -\frac{k}{4} \cdot \left(\frac{3\sqrt{u^2+4d^2}u\sqrt{u^2+d^2} + 2\sqrt{u^2+4d^2}ud}{\sqrt{u^2+4d^2}u\sqrt{u^2+d^2}d} + \right. \\ &\quad \left. \frac{6\sqrt{u^2+4d^2}\sqrt{u^2+d^2}d - 8u\sqrt{u^2+d^2}d}{\sqrt{u^2+4d^2}u\sqrt{u^2+d^2}d} \right) \end{aligned} \tag{A.13}$$

Manipulating the expressions for W and E results in

$$W - E = 0 \tag{A.14}$$

We have shown that W and E are equal, and therefore it is appropriate to use the formula A.1 for calculating the electrostatic energy of mixed layers. The calculation was done using Maple 10 software.

Appendix B

Calculation of electrostatic energy

The electrostatic energy of the mixed CsI layer is calculated using Visual C^{++} development studio. It is evaluated separately for each atom and its image charge in the unit cell. The overall energy for the unit cell is then calculated from

$$E = \frac{\sum_{i=1}^{N} E_i}{2 \cdot 2} \tag{B.1}$$

where the index i runs through all the real charges and image charges in the unit cell. The origin of the $2 \cdot 2$ term is discussed in appendix A and chapter *4*. The electrostatic energy for each charge and its image charge in the unit cell is calculated from

$$E_i = \frac{q_i}{4\pi\varepsilon_0} \cdot \sum_{h=-\infty}^{\infty} \sum_{k=-\infty}^{\infty}{}' \sum_{l=0}^{1} \frac{q_{hkl}}{|r_{hkl}|} - \frac{q_i^2}{4\pi\varepsilon_0} \cdot \frac{1}{2d_j} \tag{B.2}$$

. Here q_i is charge of the ith point charge, q_{hkl} is a charge at distance r_{hkl} away from q_i, where indices h and k describe the adsorbate position on the surface relative to the ith position. l distinguishes between image charges and normal charges and d_j distinguishes between d_+ or d_- depending on the ith charge sign. The prime on the double sum indicates the exclusion of $h = 0, k = 0$ from the sum**.** The last term corresponds to the energy from an induced image charge attraction. Because it is

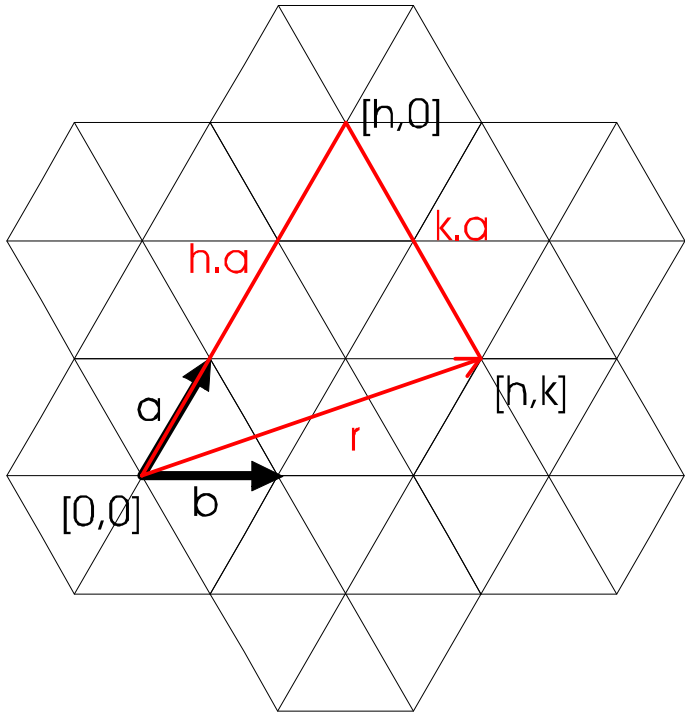

Figure B.1: Pt(111) hexagonal structure used to evaluate the Madelung sum. Lattice vector $|\overrightarrow{a}| = \left|\overrightarrow{b}\right|$. Every point in the grid can be described by the vector $\overrightarrow{r}_{hk} = h\overrightarrow{a} + k\overrightarrow{a}$.

impossible to calculate an infinite sum, the limits for h,k are set to $-5000..5000$. The energy contribution from a charge and its image charge is the same, therefore only E_i for real charges was explicitly calculated.

The surface is divided into 6 different "pizza" wedges (defined by vectors $\overrightarrow{a}$ and $\overrightarrow{b}$), where the charge, for which we calculate the energy, is located in the center of the "pizza" $[0,0]$ (Fig. B.1). The Madelung sum

$$summ = \sum_{h=1}^{5000} \sum_{k=0}^{h} \frac{q_i \cdot q_{hk}}{|r_{hk}|} \tag{B.3}$$

needs to be calculated for each wedge, because it can generally differ between wedges. However, evaluation of the sum for each wedge is not always necessary as some of

the calculated structures have rotational symmetry. The details are provided in the source codes.

The electrostatic energy of the positive charge (Cs) and the negative charge (I) within the unit cell is generally different and the Madelung sum for each is calculated separately. The nomenclature of the code is as follows: Madelung sum for positive charges (Cs) at the $[0,0]$ position

$$ss = \sum_{h=1}^{5000} \sum_{k=0}^{h} \frac{q_{Cs} \cdot q_{hk}}{|r_{hk}|} \tag{B.4}$$

and for negative charges (I) at the $[0,0]$ position

$$xx = \sum_{h=1}^{5000} \sum_{k=0}^{h} \frac{q_{I} \cdot q_{hk}}{|r_{hk}|} \tag{B.5}$$

Those sums are further separated into two parts**:** the contribution of surrounding positive charges to the overall Madelung sum and the contribution of surrounding negative charges to the overall Madelung sum.

$$ss = ssCs + ssI \tag{B.6}$$

$$xx = xxCs + xxI \tag{B.7}$$

This is necessary as the $|q|$ of atoms is not the necessarily same for I and Cs. The contribution to the overall sum (ss) from Cs atoms (positive charges) is denoted as

$$ssCs = \sum_{h'} \sum_{k'} \frac{q_{Cs} \cdot q_{Cs,h'k'}}{|r_{h'k'}|} \tag{B.8}$$

where indexes $h'k'$ include only Cs atoms. Similarly

$$ssI = \sum_{h^*} \sum_{k^*} \frac{q_{Cs} \cdot q_{I,h^*k^*}}{|r_{h^*k^*}|} \tag{B.9}$$

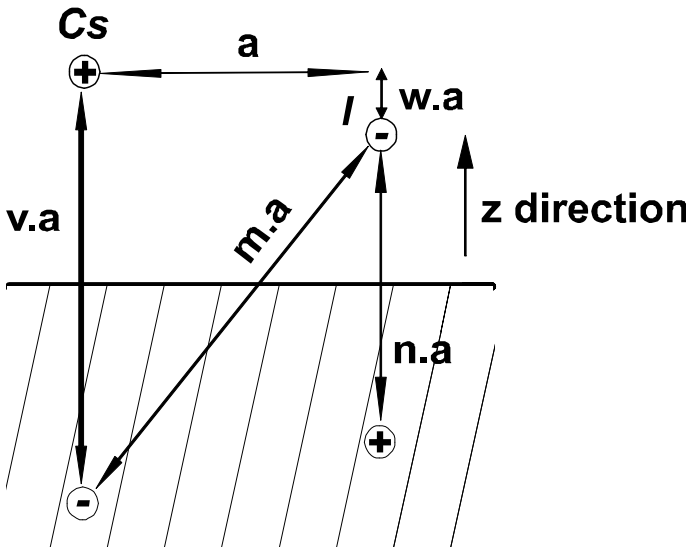

Figure B.2: The graphical interpretation of terms used in the electrostatic calculations for mixed CsI layers.

h^*k^* include only I atoms. When the electrostatic energy is calculated for negative charges in the unit cell, the Madelung sums are denoted as

$$xxCs = \sum_{h'} \sum_{k'} \frac{q_I \cdot q_{Cs,h'k'}}{|r_{h'k'}|} \tag{B.10}$$

$$xxI = \sum_{h^*} \sum_{k^*} \frac{q_I \cdot q_{I,h^*k^*}}{|r_{h^*k^*}|} \tag{B.11}$$

The $|r_{hk}|$ term can be expressed as a multiple of a as depicted in Fig. B.2, and the a can also be put in front of the sum. The $v,\ m,\ w,\ n$ coefficients are calculated given the geometry of the surface.

The Madelung sums are evaluated in Visual C^{++} and the final summation for E_i in a Microsoft Excel spreadsheet.

B.1 Source code for electrostatic energy calculation of first structure (Fig. 4.11a)

```
#include <iostream>
#include <fstream>
#include <iomanip>
#include <math.h>
#include <conio.h>
#include <string>

using namespace std;

int main () {
int N;
double v,w,m,n,rhk,d;
double sss, ssCs, sssCs, ssI, sssI, xxx, xxCs, xxxCs, xxI, xxxI;
char s[50];
string op;

// the calculation is divided into multiple sum:
// ssCs − cs atom is the test charge, contribution to the sum from other Cs atoms;
// only from one wedge
// sssCs − cs atom is the test charge, contribution to the sum from other Cs atoms;
// total from the all atoms
// ssI− cs atom is the test charge, contribution to the sum from other I atoms;
// only from one wedge
// sssI − cs atom is the test charge, contribution to the sum from other I atoms;
// total from the all atoms
// sss − total sum, sssCs+sssI
// xxCs − I atom is the test charge, contribution to the sum from other Cs atoms;
// only from one wedge
// xxxCs − I atom is the test charge, contribution to the sum from other Cs atoms;
// total from the all atoms
```

```
// xxI − I atom is the test charge, contribution to the sum from other I atoms;
// only from one wedge
// xxxCs − I atom is the test charge, contribution to the sum from other I atoms;
// total from the all atoms
// xxx − total sum, xxxCs+xxxI

cout << "Enter number of neighbors (N): ";
cin >> N; // nubmer of neighborhood atoms in one row

cout << "Enter file name including path: ";
cin >> s;

ofstream file1; // open file
file1.open (s);

// write headers of the file
file1 << setw(6) << setiosflags(ios::left) << "N" << setw(15) << "sssTotal"
<< setw(15) << "sssCs" << setw(15) << "sssI" << setw(15) << "xxxTotal"
<< setw(15) << "xxxCs" << setw(15) << "xxxI" << setw(10) << "v"
                    << setw(10) << "w" << endl;

// v sampling (horizontal), for different Cs distances from the surface
for (int i=0; i<=20; i++) {
d=(1.5+(4−1.5)/20∗i);
        v=2∗d/3.71; //distance of Cs and its image charge

        // w sampling(horizontal), for different I distances from the surface,
        // negative sign−I is above Cs, positive sign−I is below Cs
for (int j=0; j<=30; j++) {
w=(d−(0.5+(5−0.5)/30∗j))/3.71;
           m=v−w; // z distance of I ion and Cs image charge
           n=v−2∗w; //distance between I and its image charge
sss=0; ssCs=0; sssCs=0; ssI=0; sssI=0;
xxx=0; xxCs=0; xxxCs=0; xxI=0; xxxI=0;
```

```
// sampling the surface over atoms with coordinates k,h in hexagonal grid
for (int k=1; k<=N; k++) {
        for (int h=0; h<=k; h++) {
        rhk=h*h+k*k-h*k;

        // atoms on the sides of the wedge, shared with neighborhood wedge
        if ((h==0) || (k==h)) {

// Cs atom in the center
                if ((((h+k)-1)     // contribution from I atoms
            ssI=ssI+((-1)/sqrt(rhk+w*w)+1/sqrt(rhk+m*m))/2;
else
                        // contribution from Cs atoms
            ssCs=ssCs+(1/sqrt(rhk)-1/sqrt(rhk+v*v))/2;

// I atom in the center
if (((h+k)  xxI=xxI+(1/sqrt(rhk)-1/sqrt(rhk+n*n))/2;
else
  xxCs=xxCs+((-1)/sqrt(rhk+w*w)+1/sqrt(rhk+m*m))/2;
        }
        else { // the rest of atoms located inside the wedge

// Cs atom in the center
if ((((h+k)-1)     // contribution from I atoms
         ssI=ssI+((-1)/sqrt(rhk+w*w)+1/sqrt(rhk+m*m));
else
                        // contribution from Cs atoms
         ssCs=ssCs+(1/sqrt(rhk)-1/sqrt(rhk+(v*v)));

//I atom in the center
if (((h+k)  xxI=xxI+(1/sqrt(rhk)-1/sqrt(rhk+n*n));
else
xxCs=xxCs+((-1)/sqrt(rhk+w*w)+1/sqrt(rhk+m*m));
```

```
                    }
                    }
            }
// multiply by 6 wedges (6 fold symetry)

            // total contribution from all Cs atoms when calculating sum for Cs
sssCs=6*ssCs;
            // total contribution from all I atoms when calculating sum for Cs
sssI=6*ssI;
sss=sssCs+sssI;

// total contribution from all Cs atoms when calculating sum for I
            xxxCs=6*xxCs;
            // total contribution from all I atoms when calculating sum for I
xxxI=6*xxI;
xxx=xxxCs+xxxI;

// output of calculated sum
            file1 << setiosflags(ios::left) << setw(6) << N
<< setw(15) << setiosflags(ios::fixed) << setprecision(10) << sss
                    << setw(15) << sssCs << setw(15) << sssI << setw(15) << xxx
                    << setw(15) << xxxCs << setw(15) << xxxI << setw(10) << setprecision(6)
                        << v << setw(10) << w << endl;


          }
}
file1.close();
cout << "done" <<endl ;
cout << "Press enter";
getch();
return 0;
}
```

B.2 Source code for electrostatic energy calculation of second structure (Fig. 4.11b)

```
#include <iostream>
#include <fstream>
#include <iomanip>
#include <math.h>
#include <conio.h>
#include <string>

using namespace std;

int main () {
  int N;
  double v,w,m,n,rhk,d;
  double sss, ssCs1, sssCs, ssI1, sssI, xxx, xxCs, xxxCs, xxI, xxxI, ssCs2, ssI2;
  char s[50];
  string op;

  cout << "Enter number of neighbors (N): ";
  cin >> N; // nubmer of neighborhood atoms in one row

  cout << "Enter file name including path: ";
  cin >> s;

  ofstream file1; // open file
  file1.open (s);

  // write headers of the file
  file1 << setw(6) << setiosflags(ios::left) << "N" << setw(15) << "sssTotal"
        << setw(15) << "sssCs" << setw(15) << "sssI" << setw(15) << "xxxTotal"
        << setw(15) << "xxxCs" << setw(15) << "xxxI" << setw(10) << "v"
                << setw(10) << "w" << endl;
```

```
// v sampling (horizontal), for different Cs distances from the surface
for (int i=0; i<=20; i++) {
  d=(1.5+(4−1.5)/20∗i);
      v=2∗d/5.56; //distance of Cs and its image charge

  // w sampling(horizontal), for different I distances from the surface,
      // negative sign−I is above Cs, positive sign−I is below Cs
  for (int j=0; j<=30; j++) {
    w=(d−(0.5+(5−0.5)/30∗j))/5.56;
        m=v−w; // z distance of I ion and Cs image charge
        n=v−2∗w; //distance between I and its image charge
    sss=0; ssCs1=0; sssCs=0; ssI1=0; sssI=0; ssCs2=0; ssI2=0;
    xxx=0; xxCs=0; xxxCs=0; xxI=0; xxxI=0;

        // sampling the surface over atoms with coordinates k,h in hexagonal grid
        for (int k=1; k<=N; k++) {
                for (int h=0; h<=k; h++) {
                rhk=h∗h+k∗k−h∗k;

                // atoms on the sides of the wedge, shared with neighborhood wedge.
                // two fold symmetry, two different wedges resulting in the different
                // neighbor for two Cs atmoms in the center (Cs1, Cs2)
                if ((h==0) || (k==h)) {

                        // calculation of type of the atom in h,k position
                        if ((k % 2) != 0) {
                                // I atom in the center
                                xxCs=xxCs+((−1)/sqrt(rhk+w∗w)+1/sqrt(rhk+m∗m))/2;
                                //Cs2 atom in the center
                                ssCs2=ssCs2+(1/sqrt(rhk)−1/sqrt(rhk+v∗v))/2;
                                if ((h % 2) == 0)
                                        //Cs1 atom in the center, contribution from I atoms
                                        ssI1=ssI1+((−1)/sqrt(rhk+w∗w)+1/sqrt(rhk+m∗m))/2;
```

```
                    else
                        //Cs1 atom in the center, contribution from Cs atoms
                        ssCs1=ssCs1+(1/sqrt(rhk)−1/sqrt(rhk+v∗v))/2;
                }
                else {
                    //Cs1 atom in the center
                    ssCs1=ssCs1+(1/sqrt(rhk)−1/sqrt(rhk+v∗v))/2;
                    if ((h % 2) == 0){
                        // I atom in the center
                        xxI=xxI+(1/sqrt(rhk)−1/sqrt(rhk+n∗n))/2;
                        //Cs2 atom in the center
                        ssCs2=ssCs2+(1/sqrt(rhk)−1/sqrt(rhk+v∗v))/2;
                    }
                    else {
                        // I atom in the center
                        xxCs=xxCs+((−1)/sqrt(rhk+w∗w)+1/sqrt(rhk+m∗m))/2;
                        //Cs2 atom in the center
                        ssI2=ssI2+((−1)/sqrt(rhk+w∗w)+1/sqrt(rhk+m∗m))/2;
                    }
                }
            }

            // the rest of atoms located in the wedge
            else {

            // calculation of type of the atom in h,k position
        if ((k % 2) != 0) {
                    // I atom in the center
                    xxCs=xxCs+((−1)/sqrt(rhk+w∗w)+1/sqrt(rhk+m∗m));
                    //Cs2 atom in the center
                    ssCs2=ssCs2+(1/sqrt(rhk)−1/sqrt(rhk+v∗v));
                    if ((h % 2) == 0)
                        //Cs1 atom in the center, contribution from I atoms
                        ssI1=ssI1+((−1)/sqrt(rhk+w∗w)+1/sqrt(rhk+m∗m));
```

```
                        else
                                //Cs1 atom in the center, contribution from Cs atoms
                                ssCs1=ssCs1+(1/sqrt(rhk)-1/sqrt(rhk+v*v));
                }
                else {
                        //Cs1 atom in the center
                        ssCs1=ssCs1+(1/sqrt(rhk)-1/sqrt(rhk+v*v));
                        if ((h % 2) == 0) {
                                // I atom in the center
                                xxI=xxI+(1/sqrt(rhk)-1/sqrt(rhk+n*n));
                                //Cs2 atom in the center
                                ssCs2=ssCs2+(1/sqrt(rhk)-1/sqrt(rhk+v*v));
                        }
                        else {
                                // I atom in the center
                                xxCs=xxCs+((-1)/sqrt(rhk+w*w)+1/sqrt(rhk+m*m));
                                //Cs2 atom in the center
                                ssI2=ssI2+((-1)/sqrt(rhk+w*w)+1/sqrt(rhk+m*m));
                        }
                }
        }
        }
    }
    // multiply by 6 wedges (6 fold symetry)
    // total contribution from all Cs atoms when calculating sum for Cs
sssCs=4*ssCs1+2*ssCs2;
// total contribution from all I atoms when calculating sum for Cs
sssI=4*ssI1+2*ssI2;
sss=sssCs+sssI;

    // total contribution from all Cs atoms when calculating sum for I
xxxCs=6*xxCs;
    // total contribution from all I atoms when calculating sum for I
xxxI=6*xxI;
```

```
      xxx=xxxCs+xxxI;

    // output of calculated sum
          file1 << setiosflags(ios::left) << setw(6) << N
            << setw(15) << setiosflags(ios::fixed) << setprecision(10) << sss
                << setw(15) << sssCs << setw(15) << sssI << setw(15) << xxx
                << setw(15) << xxxCs << setw(15) << xxxI << setw(10) << setprecision(6)
                    << v << setw(10) << w << endl;


        }
  }
  file1.close();
  cout << "done" <<endl ;
  cout << "Press enter";
  getch();
  return 0;
}
```

B.3 Source code for electrostatic energy calculation of third structure (Fig. 4.11d)

```
#include <iostream>
#include <fstream>
#include <iomanip>
#include <math.h>
#include <conio.h>
#include <string>

using namespace std;

int main () {
int N;
```

```
double v,w,m,n,rhkCs,rhkIx,rhkIy,rhkIz,rhkIv,rhkIw,rhkIu,d, xk, xh, yh,yk,zh,zk,vh,vk,wh,wk,
        uh,uk;
double sss, ssCs, sssCs, ssIx,ssIy,ssIz,ssIu,ssIv,ssIw, sssI, xxx, xxCs, xxxCs, xxI, xxxI, ssCs2, ssI2;
char s[50];
string op;

cout << "Enter number of neighbors (N): ";
cin >> N; // nubmer of neighborhood atoms in one row

cout << "Enter file name including path: ";
cin >> s;

ofstream file1; // open file
file1.open (s);

// write headers of the file
file1 << setw(6) << setiosflags(ios::left) << "N" << setw(15) << "sssTotal"
<< setw(15) << "sssCs" << setw(15) << "sssI" << setw(15) << "xxxTotal"
<< setw(15) << "xxxCs" << setw(15) << "xxxI" << setw(10) << "v"
            << setw(10) << "w" << setw(10) << "o" << endl;

// For third structure, sampling positions of the Cs atoms in the unit cell.
// There is no symmetry for the surface structure, therefore position for each atom in 6
// different wedges (6 different directions) must be calculated separetly.

for (int o=0; o<=3; o++) { //sampling in position in unit cell
        xk=6.0/9-o/9.0; //offset of the k index for 1st wedge
        xh=3.0/18+o/18.0; //offset of the h index for 1st wedge
        yk=xh; // 2nd wedge
        yh=1-yk;
        zk=yk; // 3rd wedge
        zh=xk;
        vk=xk; // 4th wedge
        vh=yh;
```

```
            wk=yk; // 5th wedge
            wh=xh;
            uk=xh; // 6th wedge
            uh=1−xk;

for (int i=0; i<=20; i++) { //v sampling (horizontal), for different Cs distances from the surface
d=(1.5+(4−1.5)/20∗i);
          v=2∗d/4.25;
          // w sampling(horizonatal), for different I distances from the surface,
          // negative sign−I is above Cs, positive sign−I is below Cs
for (int j=0; j<=30; j++) {
w=(d−(0.5+(5−0.5)/30∗j))/4.25;
            m=v−w;
            n=v−2∗w;
sss=0; ssCs=0; sssCs=0;ssIx=0,ssIy=0,ssIz=0,ssIu=0,ssIv=0,ssIw=0, sssI=0; ssCs2=0;
            ssI2=0; xxx=0; xxCs=0; xxxCs=0; xxI=0; xxxI=0;
// sampling the surface over atoms with coordinates k,h in hexagonal grid
            for (int k=1; k<=N; k++) {
                  for (int h=0; h<=(k−1); h++) {
                  rhkCs=h∗h+k∗k−h∗k;
                  //distance squared for I atoms in wedge 1
                  rhkIx=(h+xh)∗(h+xh)+(k−xk)∗(k−xk)−(h+xh)∗(k−xk);
                  //distance squared for I atoms in wedge 2
                  rhkIy=(h+yh)∗(h+yh)+(k+yk)∗(k+yk)−(h+yh)∗(k+yk);
                  //distance squared for I atoms in wedge 3
                  rhkIz=(h+zh)∗(h+zh)+(k−zk)∗(k−zk)−(h+zh)∗(k−zk);
                  //distance squared for I atoms in wedge 4
                  rhkIv=(h+vh)∗(h+vh)+(k+vk)∗(k+vk)−(h+vh)∗(k+vk);
                  //distance squared for I atoms in wedge 5
                  rhkIw=(h+wh)∗(h+wh)+(k−wk)∗(k−wk)−(h+wh)∗(k−wk);
//distance squared for I atoms in wedge 6
                  rhkIu=(h+uh)∗(h+uh)+(k+uk)∗(k+uk)−(h+uh)∗(k+uk);

                // Cs in the centre, calculating electrostatic energy for Cs
```

```
        //Cs atom in the centre, Cs atoms contributing to the sum (and it's image charge)
                ssCs=ssCs+(1/sqrt(rhkCs)−1/sqrt(rhkCs+v∗v));
//Cs atom in the centre, contribution from I in wedge 1
                ssIx=ssIx+((−1)/sqrt(rhkIx+w∗w)+1/sqrt(rhkIx+m∗m));
                //Cs atom in the centre, contribution from I in wedge 2
                ssIy=ssIy+((−1)/sqrt(rhkIy+w∗w)+1/sqrt(rhkIy+m∗m));
                //Cs atom in the centre, contribution from I in wedge 3
                ssIz=ssIz+((−1)/sqrt(rhkIz+w∗w)+1/sqrt(rhkIz+m∗m));
//Cs atom in the centre, contribution from I in wedge 4
                ssIv=ssIv+((−1)/sqrt(rhkIv+w∗w)+1/sqrt(rhkIv+m∗m));
                //Cs atom in the centre, contribution from I in wedge 5
                ssIw=ssIw+((−1)/sqrt(rhkIw+w∗w)+1/sqrt(rhkIw+m∗m));
                //Cs atom in the centre, contribution from I in wedge 6
                ssIu=ssIu+((−1)/sqrt(rhkIu+w∗w)+1/sqrt(rhkIu+m∗m));

                // I in the centre
//I atom in the centre, I atoms contributing, contribution from Cs atoms same as ssIx..ssIu
                xxI=xxI+(1/sqrt(rhkCs)−1/sqrt(rhkCs+n∗n));
                }
        }


// multiply
          // total contribution from all Cs atoms when calculating sum for Cs
sssCs=6∗ssCs;
         // total contribution from all I atoms when calculating sum for Cs
sssI=ssIx+ssIy+ssIz+ssIv+ssIw+ssIu;
sss=sssCs+sssI;

xxxI=6∗xxI; // total contribution from all I atoms when calculating sum for I
xxxCs=sssI; // total contribution from all Cs atoms when calculating sum for I
xxx=xxxCs+xxxI;
```

```
// output of calculated sum
          file1 << setiosflags(ios::left) << setw(6) << N
<< setw(15) << setiosflags(ios::fixed) << setprecision(10) << sss
                << setw(15) << sssCs << setw(15) << sssI << setw(15) << xxx
                << setw(15) << xxxCs << setw(15) << xxxI << setw(10) << setprecision(6)
                    << v << setw(10) << w << setw(10) << o << endl;


         }
}
}
file1.close();
cout << "done" <<endl ;
cout << "Press enter";
getch();
return 0;
}
```

Appendix C

Source code for Monte Carlo simulation

C.1 TDS_MC_thesis.cpp

```
// TDS_MC.cpp : Defines the entry point for the console application.
//
#include "stdafx.h"
#include "mtrand/mtrand.h"
#include <iostream>
#include <fstream>
#include <iomanip>
#include <math.h>
#include <conio.h>
#include <string>
#include "atom.h"
#include "grid.h"
#include <sstream>
#include "gsl−1.12\const\gsl_const_mks.h"
#include "gsl−1.12\const\gsl_const_num.h"
```

```
using namespace std;

int _tmain(int argc, _TCHAR* argv[])
{
	double T,dT,k; //temperature, rate
	int L;
	double f_E3,cov_i,totall;
	double d,beta,Rpt,alpha_1,alpha_2,alpha_3,mu0_1,mu0_2,mu0_3,nn,f_E1,f_E2,
		f_E4,alpha_4,mu0_4;
	int m,n,o,p,q,r;

	// 100 different seeds for random number generator
	for (r=1;r<=100;r++)
	{
		// output file string
		stringstream s;
		string ss;
		const char *buf;
		// parameters initialization
		L=200; // grid dimensions
		T=280; //initial temperature
		dT=1; //temperature step
		f_E1=410;
		f_E2=365;
		f_E3=360;
		f_E4=308;
		alpha_1=4.5e-30;
		alpha_2=6e-30;
		alpha_3=7e-30;
		alpha_4=4e-30;
		mu0_1=2.6e-29;
		mu0_2=2.5e-29;
```

```
mu0_3=2.5e-29;
mu0_4=2e-29;
cov_i=0.41; //initial coverage
d=0.5e-10;
beta=3e-10;
Rpt=2.78e-10;

k=5; //temperature ramp rate

//declaration of the x-tall surface
grid cryst(beta,d,Rpt,mu0_3,alpha_3,f_E3,L,cov_i,f_E1,f_E2,10,mu0_1,
        mu0_2,alpha_1,alpha_2,f_E4,mu0_4,alpha_4);

s << "e:/MC/run.txt" ; //output file
ss=s.str();
buf=ss.c_str();
// IO of the file header
ofstream file1;
file1.open (buf);

file1 << "E1=" << f_E1 << "; " << "E2=" << f_E2 << "; "
        << "E3=" << f_E3 << "; " << "E4=" << f_E4 << "; "
        << "alpha1=" << alpha_1 << "; " << "alpha2=" << alpha_2
        << "; " << "alpha3=" << alpha_3 << "; " << "alpha4="
        << alpha_4 << "; " << "mu01=" << mu0_1 << "; " << "mu02="
        << mu0_2 << "; " << "mu03=" << mu0_3 << "; " <<"mu04="
        << mu0_4 << "; " << "d=" << d << ";" << "beta=" << beta
        << ";" << "r=" << 10 << ";" << "L=" << L << "; " << "cov="
        << cov_i << endl << endl;


file1 << setw(10) << setiosflags(ios::left) << "T" << setw(15)
        << "intensity" << setw(10)<< "coverage" << setw(15) << "Energy"
        << setw(15) << "WF" <<endl;
```

```
cryst.init(); //initialization of the crystal surface

// MC alorithm
while ((cryst.remained>0)&&(T<2000.0))
{
        //intensity for theis temperature step set up to 0
        cryst.intensity=0;

        // calculation of the surface density used in energy calculation
        cryst.nn=cryst.coverage/(sin(PI/3)*cryst.g_Rpt*cryst.g_Rpt);

        //desorb
        cryst.desorb(dT,k,T);

        //debugging option, keep track of atoms desorbed from one
        //island type
        totall=cryst.tot/double(cryst.remained);

        //output the numbers to the file
        file1 << setiosflags(ios::left) << setiosflags(ios::fixed) << setw(10)
                << setprecision(2)<< T << setw(15) <<setprecision(5)
                <<cryst.intensity << setw(10) << setprecision(4) << cryst.coverage
                << setprecision(10) << setw(15) << cryst.E_tot << setw(15)
                << cryst.WF_value << setw(15) << totall << endl;
        std::cout << setiosflags(ios::left) << setiosflags(ios::fixed)
                << setw(10) << setprecision(2)<< T << setw(8) <<setprecision(5)
                <<cryst.intensity << setw(10) << setprecision(4) << cryst.coverage
                << setprecision(10) << setw(15) << cryst.E_tot << setw(15)
                << cryst.WF_value << setw(15) << totall <<endl;

        //surface relaxation
        if (cryst.remained>10)
        {
```

```
                        cryst.relax(100);
                    }
                    // calculate new T
                    T=T+dT;
                    //calculate new coverage
                    cryst.calc_cov(cryst.intensity);

                }
                //IO
                file1.close();
            std::cout << "done " << ss << "\n";

        return 0;
}
}
```

C.2 grid_thesis.cpp

```
#include "StdAfx.h"
#include "atom.h"
#include "grid.h"
#include <math.h>
#include "gsl−1.12\const\gsl_const_mks.h"
#include "gsl−1.12\const\gsl_const_num.h"
#include <iostream>

// grid initialization
grid::grid(double beta, double d, double Rpt, double mu0, double alpha,double Ucova,int L,
                    double cov_i,double f_E1,double f_E2,int seed,double mu0_1,double mu0_2,
                    double alpha_1,double alpha_2,double f_E4,double mu0_4,double alpha_4)
{
        // feed parameters into the object
        g_beta=beta;
```

```
        g_d=d;
        g_Rpt=Rpt;
        g_mu0_1=mu0_1;
        g_mu0_2=mu0_2;
        g_mu0_3=mu0;
        g_mu0_4=mu0_4;
        g_alpha_1=alpha_1;
        g_alpha_2=alpha_2;
        g_alpha_4=alpha_4;
        g_alpha_3=alpha;
        fix_E3=Ucova;
        LL=L;
        coverage=cov_i;
        remained=0;
        fix_E1=f_E1;
        fix_E2=f_E2;
        fix_E4=f_E4;
         // intialize random number generator
        ran_num.seed(seed);

        int i,j;
        //set up of each adsortion site
        for (i=0;i<=LL-1;i++)
        {
                for (j=0;j<=LL-1;j++)
                {
                        arra[i][j].status=0;
                        arra[i][j].des_E=0;
                        arra[i][j].des_prob=0;
                }
        }
}

grid::~grid(void)
```

```
{
}

void grid::desorb(double dT,double k, double T)
{
        int z=0,i,j; //keeps track of number of adsorbed atoms

        E_tot=0; // null the average desorption energy
        // each adsorbed atom is assigned desorption probablity
        get_des_prob_islands(T);
        //calculate WF
        WF();
        for (i=0;i<=LL-1;i++)
        {
                for (j=0;j<=LL-1;j++)
                {
                        // generate random number
                        // compare the desorption energy to random number
                        // change the status of the atom
                        if (arra[i][j].status==1)
                        {
                                if (ran_num()<arra[i][j].des_prob*dT/k)
                                {
                                        intensity=intensity+1;
                                        E_tot=E_tot+arra[i][j].des_E;
                                        z=z+1;
                                        arra[i][j].status=0;
                                }
                        }
                }
        }
        E_tot=E_tot/z; // average desorption energy of one atom
}
```

```
void grid::get_des_prob_islands(double T)
{
        int i,j;
        ihcp=0;
        r3r3=0;
        other=0;
        s2x2=0;
        tot=0;
        for (i=0;i<=LL-1;i++)
        {
                for (j=0;j<=LL-1;j++)
                {
                        if (arra[i][j].status==1)
                        {
                                // the desorption energy for each atom is calculated
                                arra[i][j].des_E=get_des_E(i,j);
                                // the desorption probability is calculated
                                arra[i][j].des_prob=1e13*exp(-1*(arra[i][j].des_E)
                                        /(GSL_CONST_NUM_AVOGADRO*
                                        (GSL_CONST_MKS_BOLTZMANN/1000)*T));
                        }
                }
        }
}
double grid::get_des_E(int i,int j)
{
        int i_first,i_second,i_third; //number of neighbors
        double F,E,total;

        i_first=first(i,j); //# of atoms in first adsorption shell
        i_second=second(i,j); //# of atoms in second adsorption shell
        i_third=third(i,j);//# of atoms in third adsorption shell

        //total number of atoms in the hexagonal cell
```

```
total=double(i_first)+double(i_second)/2+double(i_third)/3;

if (total>3) //if island type ihcp
{
        tot=tot+1; //debugging option

        E=-(1.0/8.0*g_mu0_1*g_mu0_1/
                (PI*GSL_CONST_MKS_VACUUM_PERMITTIVITY*
                (1.0/(1.633115623*PI*sqrt(3.0)*
                pow(nn,3.0/2.0)*(1.0+1.0/pow(1.0+8.000999888
                *g_beta*g_beta*nn,3.0/2.0))-1.0/
                (4.0*pow(g_beta,3.0)-g_beta*g_d*g_d))
                +g_alpha_1))+1.0/8.0*nn*g_mu0_1*g_mu0_1*
                (2.449673434*PI*sqrt(3.0)*sqrt(nn)*
                (1.0+1.0/pow(1.0+8.000999888*g_beta*
                g_beta*nn,3.0/2.0))-19.59983687*PI*
                sqrt(3.0)*pow(nn,3.0/2.0)*g_beta*
                g_beta/pow(1.0+8.000999888*g_beta*
                g_beta*nn,5.0/2.0))/
                (PI*GSL_CONST_MKS_VACUUM_PERMITTIVITY*
                pow(1.0/(1.633115623*PI*sqrt(3.0)*pow(nn,3.0/2.0)
                *(1.0+1.0/pow(1.0+8.000999888*g_beta*g_beta*
                nn,3.0/2.0))-1.0/(4.0*pow(g_beta,3)-g_beta*g_d*g_d))
                +g_alpha_1,2)*pow(1.633115623*PI*sqrt(3.0)*
                pow(nn,3.0/2.0)*(1.0+1.0/pow(1.0+8.000999888*
                g_beta*g_beta*nn,3.0/2.0))-1.0/(4.0*
                pow(g_beta,3)-g_beta*g_d*g_d),2)))*
                GSL_CONST_NUM_AVOGADRO/1000;

        //desorption energy fot this island
        E=E+fix_E1;
        ihcp=ihcp+1;
        return E;
}
```

```
else if (total>2) //island r3xr3
{

        E=−(1.0/8.0∗g_mu0_2∗g_mu0_2/
                (PI∗GSL_CONST_MKS_VACUUM_PERMITTIVITY∗
                (1.0/(1.633115623∗PI∗sqrt(3.0)∗
                pow(nn,3.0/2.0)∗(1.0+1.0/
                pow(1.0+8.000999888∗g_beta∗g_beta∗
                nn,3.0/2.0))−1.0/(4.0∗pow(g_beta,3.0)
                −g_beta∗g_d∗g_d))+g_alpha_2))+1.0/8.0
                ∗nn∗g_mu0_2∗g_mu0_2∗(2.449673434∗PI∗
                sqrt(3.0)∗sqrt(nn)∗(1.0+1.0/pow(1.0+8.000999888
                ∗g_beta∗g_beta∗nn,3.0/2.0))−19.59983687∗
                PI∗sqrt(3.0)∗pow(nn,3.0/2.0)∗g_beta
                ∗g_beta/pow(1.0+8.000999888∗g_beta∗
                g_beta∗nn,5.0/2.0))/
                (PI∗GSL_CONST_MKS_VACUUM_PERMITTIVITY∗
                pow(1.0/(1.633115623∗PI∗sqrt(3.0)∗
                pow(nn,3.0/2.0)∗(1.0+1.0/pow(1.0+8.000999888
                ∗g_beta∗g_beta∗nn,3.0/2.0))−1.0/(4.0∗
                pow(g_beta,3)−g_beta∗g_d∗g_d))+g_alpha_2,2)∗
                pow(1.633115623∗PI∗sqrt(3.0)∗pow(nn,3.0/2.0)
                ∗(1.0+1.0/pow(1.0+8.000999888∗g_beta∗g_beta∗
                nn,3.0/2.0))−1.0/(4.0∗pow(g_beta,3)−g_beta∗
                g_d∗g_d),2)))∗GSL_CONST_NUM_AVOGADRO/1000;


        //desorption energy fot this island
        E=E+fix_E2;
        r3r3=r3r3+1;
        return E;
}
else if (total>=0.8) //island 2x2
{
```

```
        E=−(1.0/8.0∗g_mu0_3∗g_mu0_3/
                (PI∗GSL_CONST_MKS_VACUUM_PERMITTIVITY∗
                (1.0/(1.633115623∗PI∗sqrt(3.0)∗pow(nn,3.0/2.0)
                ∗(1.0+1.0/pow(1.0+8.000999888∗g_beta∗g_beta∗
                nn,3.0/2.0))−1.0/(4.0∗pow(g_beta,3.0)−g_beta∗
                g_d∗g_d))+g_alpha_3))+1.0/8.0∗nn∗g_mu0_3∗
                g_mu0_3∗(2.449673434∗PI∗sqrt(3.0)∗sqrt(nn)∗
                (1.0+1.0/pow(1.0+8.000999888∗g_beta∗g_beta∗
                nn,3.0/2.0))−19.59983687∗PI∗sqrt(3.0)∗
                pow(nn,3.0/2.0)∗g_beta∗g_beta/pow(1.0+8.000999888
                ∗g_beta∗g_beta∗nn,5.0/2.0))/
                (PI∗GSL_CONST_MKS_VACUUM_PERMITTIVITY∗
                pow(1.0/(1.633115623∗PI∗sqrt(3.0)∗pow(nn,3.0/2.0)
                ∗(1.0+1.0/pow(1.0+8.000999888∗g_beta∗g_beta∗
                nn,3.0/2.0))−1.0/(4.0∗pow(g_beta,3)−g_beta∗
                g_d∗g_d))+g_alpha_3,2)∗pow(1.633115623∗PI∗
                sqrt(3.0)∗pow(nn,3.0/2.0)∗(1.0+1.0/
                pow(1.0+8.000999888∗g_beta∗g_beta∗
                nn,3.0/2.0))−1.0/(4.0∗pow(g_beta,3)−g_beta∗g_d∗
                g_d),2)))∗GSL_CONST_NUM_AVOGADRO/1000;

        //desorption energy fot this island
        E=E+fix_E3;
        s2x2=s2x2+1;
        return E;
}
else //anomalous
{

        //desorption energy fot anomalous Cs
        E=fix_E4;
        other=other+1;
        return E;
}
```

```
}
int grid::first(int k,int l) // get number of first shell neighbors
{
        int sum=0;

        sum=arra[mod((k+1),LL)][l].status +
                arra[mod((k−1),LL)][l].status +
                arra[k][mod((l+1),LL)].status +
                arra[k][mod((l−1),LL)].status +
                arra[mod((k+1),LL)][mod((l−1),LL)].status +
                arra[mod((k−1),LL)][mod((l+1),LL)].status;
        return sum;
}
int grid::second(int k,int l) // get number of second shell neighbors
{
        int sum=0;

        sum=arra[mod((k−2),LL)][mod((l+1),LL)].status +
                arra[mod((k−1),LL)][mod((l+2),LL)].status +
                arra[mod((k+1),LL)][mod((l+1),LL)].status +
                arra[mod((k+2),LL)][mod((l−1),LL)].status +
                arra[mod((k+1),LL)][mod((l−2),LL)].status +
                arra[mod((k−1),LL)][mod((l−1),LL)].status;
        return sum;
}
int grid::third(int k,int l) // get number of third neighbors
{
        int sum=0;

        sum=arra[mod((k+2),LL)][l].status +
                arra[mod((k−2),LL)][l].status +
                arra[k][mod((l+2),LL)].status +
                arra[k][mod((l−2),LL)].status +
                arra[mod((k+2),LL)][mod((l−2),LL)].status +
```

```
                arra[mod((k−2),LL)][mod((l+2),LL)].status;
        return sum;
}
void grid::calc_cov(int intensity) //calculates the grid coverage
{
        remained=remained−intensity;
        coverage=double(remained)/(LL∗LL);
}
void grid::relax(double per) // grid relaxation
{
        int a,b,c,d,z,i;
        double q,E1,E0,tot1,tot2;
        int i_first,i_second,i_third; //number of neighbors

        q=per;
        i=0;

        // switch per do
        {
                // unoccupied/occupied pair switch
                //find occupied/unoccupied pair
                do
                {
                        a=int(ran_num()∗LL−0.5);
                        b=int(ran_num()∗LL−0.5);
                        c=int(ran_num()∗LL−0.5);
                        d=int(ran_num()∗LL−0.5);
                }
                while ((arra[a][b].status==1&&arra[c][d].status==1)||
                        (arra[a][b].status==0&&arra[c][d].status==0));

                i_first=first(a,b);
                i_second=second(a,b);
                i_third=third(a,b);
```

```
                tot1=double(i_first)+double(i_second)/2+double(i_third)/3;

                i_first=first(c,d);
                i_second=second(c,d);
                i_third=third(c,d);
                tot2=double(i_first)+double(i_second)/2+double(i_third)/3;



                // if empty site is lower energy
                if ((arra[a][b].status==1&&tot1>tot2)||
                        (arra[c][d].status==1&&tot2>tot1))
                {
                        // do the switch
                        z=arra[a][b].status;
                        arra[a][b].status=arra[c][d].status;
                        arra[c][d].status=z;
                        i=0;
                }
                else
                {
                        i=i+1;
                }
          }
        while (i<q);

}
void grid::init(void) // grid initialization
{
        int i,a,b;
        //fill out the grid with atoms
        for (i=1;i<=coverage*LL*LL;i++)
        {
                a=int(ran_num()*LL-0.5);
```

```
                b=int(ran_num()*LL-0.5);
                if (arra[a][b].status==0)
                {
                        arra[a][b].status=1;
                        remained=remained+1;
                }
                else
                {
                        i=i-1;
                }
        }

        relax(500);

}

void grid::show_array(void) //debugging procedure
{
        int i,j;
        std::cout<<"\n\n\n";
        for(i=0;i<LL;i++)
{
                std::cout<<"\n";
                for(j=0;j<LL;j++)
                {
                        std::cout<<" "<<arra[j][i].status;
                }
        }
}

void grid::test(void) //debugging procedure
{
        std::cout<<"test/n";
}
```

```
int grid::mod(int x, int y) //modulo definition
{
        if (x>=0)
        {
                return x − y ∗ (x / y);
        }
        else
        {
                return y+x;
        }
}
void grid::WF(void) //WF calculation
{
        double WFihcp,WFr3r3,WFother,n,WFs2x2;

         n=double(ihcp)/(LL∗LL∗sin(PI/3)∗g_Rpt∗g_Rpt);
         WFihcp=−0.55e−29∗n/GSL_CONST_MKS_VACUUM_PERMITTIVITY;

        n=double(r3r3)/(LL∗LL∗sin(PI/3)∗g_Rpt∗g_Rpt);

        WFr3r3=−0.9e−29∗n/GSL_CONST_MKS_VACUUM_PERMITTIVITY;

        n=double(s2x2)/(LL∗LL∗sin(PI/3)∗g_Rpt∗g_Rpt);

        WFs2x2=−1.70e−29∗n/GSL_CONST_MKS_VACUUM_PERMITTIVITY;

        n=double(other)/(LL∗LL∗sin(PI/3)∗g_Rpt∗g_Rpt);
        WFother=−1.2e−29∗n/GSL_CONST_MKS_VACUUM_PERMITTIVITY;
        WF_value=WFihcp+WFr3r3+WFs2x2+WFother;
}
```

References

[1] G. A. Somorjai, *Introduction to Surface Chemistry and Catalysis*, Wiley-Interscience, 1 ed., 1994.

[2] M. Maack, H. Friis-Jensen, S. Sckerl, J. H. Larsen, and I. Chorkendorff, *Top. Catal.*, 2003, **22**(3), 151–160.

[3] ed. A. Nilsson, L. Pettersson, and J. Norskov, *Chemical Bonding at Surfaces and Interfaces*, Elsevier, 2008.

[4] J. J. Mortensen, B. Hammer, and J. K. Nørskov, *Phys. Rev. Lett.*, 1998, **80**(19), 4333–4336.

[5] E. L. Garfunkel and G. A. Somorjai, *Surf. Sci.*, 1982, **115**, 441–454.

[6] M. W. Roberts and C. S. McKee, *Chemistry of the Metal-Gas Interface*, Oxford University Press, New York, 1978.

[7] R. Diehl and R. McGrath, *Surf. Sci. Rep.*, 1996, **23**(2-5), 43–171.

[8] I. Langmuir, *J. Am. Chem. Soc.*, 1932, **54**(7), 2798–2832.

[9] R. W. Gurney, *Phys. Rev.*, 1935, **47**(6), 479–482.

[10] J. Topping, *P. R. Soc. London: A*, 1927, **114**(766), 67–72.

[11] R. D. Diehl and R. McGrath, *J. Phys.: Condens. Matter*, 1997, **9**(5), 951–968.

[12] C. Stampfl and M. Scheffler, *Surf. Rev. Lett.*, 1995, **2**(03), 317–343.

[13] R. W. Verhoef and M. Asscher, *Surf. Sci.*, 1997, **391**(1-3), 11 – 18.

[14] G. E. Rhead, *Surf. Sci.*, 1988, **203**, L663–L671.

[15] G. E. Rhead, *Appl. Surf. Sci.*, 1991, **47**, 35–42.

[16] E. V. Albano, *J. Chem. Phys.*, 1986, **85**(2), 1044–1051.

[17] R. O. Unac, *J. Phys.: Condens. Matter*, 1997, **9**, 9469–9482.

[18] J.X.Wang, I. K. Robinson, J. E. DeVilbiss, and R. Adzic, *J. Phys. Chem. B*, 2000, **104**, 7951–7959.

[19] J. X. Wang, I. K. Robinson, and R. R. Adzic, *Surf. Sci.*, 1998, **412-413**, 374 – 383.

[20] R. R. Adzic and J. X. Wang, *J. Phys. Chem. B*, 1998, **102**(33), 6305–6308.

[21] M. Labayen and D. A. Harrington, *J. Electroanal. Chem.*, 2004, **567**, 185–192.

[22] J. Wang, G. Watson, and B. Ocko, *J. Phys. Chem.*, 1996, **100**(16), 6672–6677.

[23] M. Labayen and D. A. Harrington, *J. Electroanal. Chem.*, 2005, **583**(1), 77 – 83.

[24] M. Labayen, D. A. Harrington, M. Saidy, and K. A. Mitchell, *Surf. Sci.*, 2001, **490**, 256–264.

[25] S. A. Furman, M. Labayen, R. G. Dean, and D. A. Harrington, *J. Vac. Sci. Technol., A*, 2001, **19**(3), 1032–1033.

[26] K. Griffiths and D. Bonnett, *Surf. Sci.*, 1986, **177**(1), 169–190.

[27] S. A. Furman and D. A. Harrington, *J. Vac. Sci. Technol., A*, 1996, **14**(1), 256–257.

[28] S. Stolbov and T. S. Rahman, *Phys. Rev. Lett.*, 2006, **96**(18), 186801.

[29] J. Lehmann, P. Roos, and E. Bertel, *Phys. Rev. B*, 1996, **54**(4), R2347–R2350.

[30] J. B. Hannon, M. Giesen, C. Klünker, G. Schulze Icking-Konert, D. Stapel, H. Ibach, and J. E. Müller, *Phys. Rev. Lett.*, 1997, **78**(6), 1094–1097.

[31] P. Wenter and N. Memmel, *Surf. Sci.*, 2002, **513**(2), L419–L424.

[32] C. Klünker, C. Steimer, J. B. Hannon, M. Giesen, and H. Ibach, *Surf. Sci.*, 1999, **420**(1), 25–32.

[33] S. A. Furman *Surface Chemistry of Iodine on Platinum(111)* PhD thesis, University of Victoria, 1998.

[34] Y. Yamada, A. Sinsarp, M. Sasaki, and S. Yamamoto, *Jpn. J. Appl. Phys.*, 2002, **41**, 5003–5007.

[35] J. Cousty, *Surf. Sci.*, 1989, **223(3)**, 479–92.

[36] T. E. Felter and A. T. Hubbard, *J. Electroanal. Chem.*, 1979, **100**, 473 – 491.

[37] B. C. Schardt, S.-L. Yau, and F. Rinaldi, *Science*, 1989, **243**(4894), 1050–1053.

[38] S. C. Chang, S. L. Yau, B. C. Schardt, and M. J. Weaver, *J. Phys. Chem*, 1991, **95**(12), 4787–4794.

[39] M. Saidy, K. A. R. Mitchell, S. A. Furman, M. Labayen, and D. A. Harrington, *Surf. Rev. Lett.*, 1999, **6**(5), 871–881.

[40] J. Cousty and R. Riwan, *Surf. Sci.*, 1988, **204(1-2)**, 45–56.

[41] A. Sinsarp, Y. Yamada, M. Sasaki, and S. Yamamoto, *Jpn. J. Appl. Phys.*, 2003, **42**, 4882–4886.

[42] J. M. Davidsen, F. C. Henn, G. K. Rowe, and C. T. Campbell, *J. Phys. Chem*, 1991, **95**, 6632–6642.

[43] S. J. Pratt, D. K. Escott, and D. A. King, *Phys. Rev. B*, 2003, **68**(23), 235406.

[44] R. I. Masel, *Principles of Adsorption and Reaction on Solid Surfaces*, John Wiley and Sons, Inc., 1st ed., 1996.

[45] M. Labayen, S. A. Furman, and D. A. Harrington, *Surf. Sci.*, 2003, **525**, 149–158.

[46] C.-S. Zhang, B. J. Flinn, I. V. Mitchell, and P. R. Norton, *Surf. Sci.*, 1991, **245**(3), 373 – 379.

[47] M. Tushaus, P. Gardner, and A. M. Bradshaw, *Langmuir*, 1993, **9**, 3491–3496.

[48] K. H. Ernst and C. T. Campbell, *Surf. Sci.*, 1991, **256(1-2)**, L736–L738.

[49] S. Moré, W. Berndt, A. M. Bradshaw, and R. Stumpf, *Phys. Rev. B*, 1998, **57**(15), 9246–9254.

[50] M. Scheffler and C. Stampfl, *Handbook of Surface Science*, Vol. 2, Elsevier, Amsterdam, 2000.

[51] G. N. Derry and P. N. Ross, *J. Chem. Phys.*, 1985, **82**(6), 2772–2778.

[52] M. Hohenegger, E. Bechtold, and R. Schennach, *Surf. Sci.*, 1998, **412-413**, 184–191.

[53] W. Ranke, *Surf. Sci.*, 1989, **209**(1-2), 57–76.

[54] D. H. Parker, M. E. Bartram, and B. E. Koel, *Surf. Sci.*, 1989, **217**(3), 489–510.

[55] J. L. Gland and E. B. Kollin, *J. Chem. Phys.*, 1983, **78**(2), 963–974.

[56] A. Szabo, M. Kiskinova, and J. T. Yates, *J. Chem. Phys.*, 1989, **90**(8), 4604–4612.

[57] J. F. Weaver, J.-J. Chen, and A. L. Gerrard, *Surf. Sci.*, 2005, **592**(1-3), 83–103.

[58] S. P. Devarajan, J. A. Hinojosa, and J. F. Weaver, *Surf. Sci.*, 2008, **602**(19), 3116 – 3124.

[59] B. G. Bravo, S. L. Michelhaugh, M. P. Soriaga, I. Villegas, D. W. Suggs, and J. L. Stickney, *J. Phys. Chem.*, 1991, **95**(13), 5245–5249.

[60] X. Gao, G. J. Edens, F.-C. Liu, M. J. Weaver, and A. Hamelin, *J. Phys. Chem.*, 1994, **98**(33), 8086–8095.

[61] J. L. Stickney, S. D. Rosasco, G. N. Salaita, and A. T. Hubbard, *Langmuir*, 1985, **1**(1), 66–71.

[62] J. Drnec and D. A. Harrington, *Surf. Sci.*, 2009, **603**(13), 2005 – 2014.

[63] R.Riwan, C.Papageorgopoulos, and J.Cousty, *Surf. Sci.*, 1991, **251/252**, 1086–1090.

[64] E. C. Honea, M. L. Homer, and R. L. Whetten, *Phys. Rev. B*, 1993, **47**(12), 7480–7493.

[65] A. T. Hubbard, *Chem. Rev.*, 1988, **88**(4), 633–656.

[66] P. S. Bagus, C. Woll, and A. Wieckowski, *Surf. Sci.*, 2009, **603**(2), 273 – 283.

[67] R. D. Shannon, *Acta Crystallographica A*, 1976, **32**(5), 751–767.

[68] T. B. Rymer and P. G. Hambling, *Acta Crystallographica*, 1951, **4**(6), 565.

[69] *CRC Handbook of Chemistry and Physics [Online]*, CRC Press: Boca Raton, Florida, 89 ed., 2009.

[70] J. V. Barth, R. J. Behm, and G. Ertl, *Surf. Sci.*, 1995, **341**(1-2), 62 – 91.

[71] A.Cassuto, S.Schmidt, and M. Mane, *Surf. Sci.*, 1993, **284**, 273–280.

[72] M.Ayyoob and M.S.Hedge, *Surf. Sci.*, 1983, **133**, 516–532.

[73] G. Pirug, H.P.Bonzel, and G. Broden, *Surf. Sci.*, 1982, **122**, 1–20.

[74] J.E.Crowel, E. Garfunkel, and G.A.Samorjai, *Surf. Sci.*, 1982, **121**, 303–320.

[75] L. Whitman and W. Ho, *J. Chem. Phys*, 1989, **90**, 6018–6025.

[76] T. Kondo, T. Sasaki, and S. Yamamoto, *J. Chem. Phys.*, 2002, **116**, 7673–7684.

[77] J. Drnec and D. A. Harrington, *Submitted to Surf. Sci.*, 2010.

[78] S. K. Jo and J. White, *Surf. Sci.*, 1992, **261**(1-3), 111 – 117.

[79] H. Steininger, S. Lehwald, and H. Ibach, *Surf. Sci.*, 1982, **123**(1), 1 – 17.

[80] C. Campbell, G. Ertl, H. Kuipers, and J. Segner, *Surf. Sci.*, 1981, **107**(1), 220 – 236.

[81] N. R. Avery, *Chem. Phys. Lett.*, 1983, **96**(3), 371 – 373.

[82] P. D. Nolan, B. R. Lutz, P. L. Tanaka, J. E. Davis, and C. B. Mullins, *J. Chem. Phys.*, 1999, **111**(8), 3696–3704.

[83] A. Politano, V. Formoso, and G. Chiarello, *Appl. Surf. Sci.*, 2008, **254**(21), 6854 – 6859.

[84] P. Finetti, M. Scantlebury, R. McGrath, F. Borgatti, M. Sambi, L. Zaratin, and G. Granozzi, *Surf. Sci.*, 2000, **461**, 240–254.

[85] Q. B. Lu, R. Souda, D. J. O'Connor, and B. V. King, *Phys. Rev. Lett.*, 1996, **77**(15), 3236–3239.

[86] T. Ikari, S. Arikado, K. Kameishi, H. Kawahara, K. Yamada, A. Watanabe, M. Naitoh, and S. Nishigaki, *Appl. Surf. Sci.*, 2006, **252**(15), 5424 – 5427.

[87] D. Pacilè, M. Papagno, G. Chiarello, L. Papagno, and E. Colavita, *Surf. Sci.*, 2004, **558**(1-3), 89 – 98.

[88] A. Cupolillo, G. Chiarello, S. Scalese, L. S. Caputi, L. Papagno, and E. Colavita, *Surf. Sci.*, 1998, **415**(1-2), 62 – 69.

[89] S. Murray, D. Brooks, F. Leibsle, R. Diehl, and R. McGrath, *Surf. Sci.*, 1994, **314**(3), 307 – 314.

[90] A. Cassuto, S. Schmidt, and M. Mane, *Surf. Sci.*, 1993, **284**(3), 273–280.

[91] X. S. D Heskett, D Tang and K. D. Tsuei, *J. Phys.: Condens. Matter*, 1993, **5**(27), 4601–4610.

[92] D. Heskett, D. Tang, X. Shi, and K. D. Tsuei, *Chem. Phys. Lett.*, 1992, **199**(1-2), 138–143.

[93] H. Over, H. Bludau, M. Skottke-Klein, W. Moritz, and G. Ertl, *Phys. Rev. B*, 1992, **46**(7), 4360–4363.

[94] H. Ishida, *Phys. Rev. B*, 1988, **38**(12), 8006–8021.

[95] H. Ishida, *Phys. Rev. B*, 1990, **42**(17), 10899–10911.

[96] R. W. Verhoef, W. Zhao, and M. Asscher, *J. Chem. Phys.*, 1997, **106**(22), 9353–9361.

[97] Z. SIDORSKI, *Appl. Phys. A: Mater*, 1984, **33**(4), 213–225.

[98] J. Neugebauer and M. Scheffler, *Phys. Rev. Lett.*, 1993, **71**(4), 577–580.

[99] S. Lee, M. Weiss, and G. Ertl, *Surf. Sci.*, 1981, **108**(2), 357 – 367.

[100] T. Vaara, J. Vaari, and J. Lahtinen, *Surf. Sci.*, 1998, **395**(1), 88 – 97.

[101] C. Resch, V. Zhukov, A. Lugstein, H. Berger, A. Winkler, and K. Rendulic, *Chem. Phys.*, 1993, **177**(2), 421 – 431.

[102] R. A. de Paola, J. Hrbek, and F. M. Hoffmann, *J. Chem. Phys.*, 1985, **82**(5), 2484–2498.

[103] J. Hrbek, M.-L. Shek, T. K. Sham, and G.-Q. Xu, *J. Chem. Phys.*, 1989, **91**(9), 5786–5792.

[104] L. Schmidt and R. Gomer, *J. Chem. Phys.*, 1965, **42**(10), 3573–3598.

[105] G. Rangelov and L. Surnev, *Surf. Sci.*, 1987, **185**(3), 457 – 468.

[106] R. Gerlach and T. Rhodin, *Surf. Sci.*, 1970, **19**(2), 403 – 426.

[107] J. Zivojinov and M. Srekovic, *Tehnika*, 1979, **31**(9), T6–T9.

[108] B. L. Maschhoff and J. P. Cowin, *J. Chem. Phys.*, 1994, **101**(9), 8138–8151.

[109] S. Moré, A. P. Seitsonen, W. Berndt, and A. M. Bradshaw, *Phys. Rev. B*, 2001, **63**(7), 075406.

[110] Z. Liu and P. Hu, *J. Am. Chem. Soc.*, 2001, **123**(50), 12596–12604.

[111] W. Lai, W. Huang, and D. Xie, *Phys. Chem. Chem. Phys*, 2008, **10**(12), 1669–1674.

[112] W. Lai and D. Xie, *J. Phys. Chem. B*, 2006, **110**(47), 23904–23910.

[113] H. Xiao and D. Xie, *Surf. Sci.*, 2004, **553**(1-3), 13–22.

[114] M. Matsumoto and T. Nishimura, *ACM Trans. Model. Comput. Simul.*, 1998, **8**(1), 3–30.

[115] A. Loburets, A. Naumovets, and Y. Vedula, *Surf. Sci.*, 1982, **120**(2), 347 – 366.